BETA DECAY STUDIES IN NEUTRON RICH Tc, Ru, Rh AND Pd ISOTOPES AND THE WEAK R-PROCESS

By

Fernando Montes

A DISSERTATION

Submitted to
Michigan State University
in partial fulfillment of the requirements
for the degree of

DOCTOR OF PHILOSOPHY

Department of Physics and Astronomy

2005

ABSTRACT

BETA DECAY STUDIES IN NEUTRON RICH Tc, Ru, Rh AND Pd ISOTOPES AND THE WEAK R-PROCESS

By

Fernando Montes

The r-process is responsible for the creation of more than half of the existing elements heavier than iron in the universe. Because most of the isotopes involved in its proposed path have not been reached experimentally, most of the nuclear physics required to successfully model the r-process has been derived using theoretical models. Among the most important nuclear properties necessary to model the r-process are β-decay half-lives $T_{1/2}$ and β-delayed neutron emission probabilities P_n. The mass region around the shell closure $N = 82$ has been of considerable theoretical and experimental interest since nuclear physics in that region is responsible for the creation of elements in the onset and $A \approx 130$ peak of the solar r-process abundance pattern.

β-decay studies were performed at the National Superconducting Cyclotron Laboratory. A new technique at the NSCL to measure the kinetic energy of the implanting fragments was used to distinguish charge states of the fragments in the particle identification. β-delayed neutron branchings for neutron-rich $^{116-120}$Rh, $^{120-122}$Pd and ^{124}Ag have been measured and they are direct inputs in r-process calculations. Half-lives for neutron-rich $^{114-115}$Tc, $^{114-118}$Ru, $^{116-121}$Rh and $^{119-124}$Pd have also been measured.

The results agree reasonably well with theoretical QRPA calculations within model uncertainties and the only exception is the neutron branching of ^{120}Rh. The measured P_n values are direct inputs in r-process network calculations. The isotopic solar r-process abundance ratio ^{120}Sn/^{119}Sn increases by 40% when using the experimental values instead of the prediction by the ETFSI-Q mass model. Although it is not possible to draw definite conclusions about the shell structure in this mass region

based on the measured $T_{1/2}$ and P_n values alone, it was found that the absolute values of the quadrupole deformation ϵ_2 have to be maintained or slightly reduced from the predicted FRDM and ETFSI-Q models values to have agreement with measured $^{116-119}$Rh $T_{1/2}$ and P_n values. Furthermore, a systematic increase in Q_β values best reproduces the experimental values of the ^{121,123}Pd isotopes. A relative weakening of the neutron shell closure at $N = 82$ is consistent with an increase in the Q_β values for the exotic Pd isotopes but because the predicted β-strength functions may have systematic problems, such increase might be compensating for other nuclear structure deficiencies.

The region Sr-Ag is not only of particular interest due the challenges in obtaining the observed solar r-process abundance pattern when modeling the r-process but also because there are some discrepancies between elemental abundances from r-process rich metal-poor and solar system r-process abundances. Even though there are ambiguities in the contribution of the s-process that is used to calculate the solar r-process abundance pattern, elements $42 \leq Z \leq 47$ seem to be less abundant than the solar abundance. These observations suggest that an additional mechanism besides the *strong* r-process is required to create the missing or residual abundances in the region $Z \leq 47$. Since the astrophysical scenario and conditions necessary for such a process were not known, a network calculation with classical neutron exposures from s-process to r-process type was used to find the astrophysical conditions (n_n, T, τ) in which a neutron capture process would produce the necessary residual abundance pattern. Neutron density and temperature were spanned from 10^7 (s-process) to 10^{22} cm^{-3} (r-process) and from 0.09 to 1.5 GK, respectively. Neutron densities and temperatures that resemble a r-process-like scenario were found to better fit the residual abundance pattern. An overabundance of Pd was calculated and it may be due to incorrect nuclear structure properties when modeling the neutron capture process.

to Monica, my inspiration and my light

ACKNOWLEDGMENTS

I would like to thank my advisor Hendrik Schatz who always was enthusiastic and willing to help me through my time at the NSCL. He was extremely supportive and made me realize how the most daunting tasks can actually be pretty easy. I will always remember how everything can be done in 30 minutes.

I would like to thank Paul Mantica for answering all my questions and explaining even the most trivial things.

I would like to thank all the people in the Schatz group; Peter Santi for his help during the setup and running of the experiment and because he was always there when I had a problem; Paul Hosmer for all the discussions and for making my stay at the lab really enjoyable; Thom Elliot for being my personal Google, helping me with network calculations and proof-reading of the manuscript; Alfredo Estrade and Michelle Ouellette for the mate and ice cream meetings.

I would like to thank Colin Morton, Sean Liddick and Bryan Tomlin for all their help during the experiment and for valuable *physics* discussions.

I would like to thank my collaborators at the University of Mainz, Bernd Pfeiffer and K.-L. Kratz for reminding me multiple times of previous work pertinent to mine and their help with theoretical calculations.

I would like to thank my collaborators at the University of Maryland and Notre Dame, Bill Walters and Andreas Woehr for having the time to discuss my results.

I would like to thank the members of my guidance committee, Vladimir Zelevinsky, Carl Schmidt, Thomas Glasmacher, Ed Brown and Tim Beers for answering my occasional questions.

I would like to thank the staff of the NSCL for their help and advice; the computer department, especially Barbara Pollack, for help with my multiple software and disk-space requests; the A1900 group for being extremely helpful in the preparation of and during the experiment.

I would like to thank those who supported and believed in me. To fellow graduate students, Jorge Benitez, Mark Wallace, Eric Pellegrini, Divya Singh and Mustafa al-HajDarwhish. To Shruti Tewari and Jennifer Nichols for their friendship.

Finally, I would like to thank my wife and family. I always had their understanding and constant encouragement through my years in graduate school. Thank you Monica for always being there.

Contents

List of Figures

List of Tables

Chapter 1

Astrophysics

1.1 Introduction

We are interested in the creation of elements. Elements have been created since the Big Bang occurred some 13 Gyr ago. Almost all the H and He along with some of the Li currently existing in the universe was created a few minutes after the Big Bang. As shown in Fig. 1.1, the elemental composition after those few minutes consisted of 76% H and 24% He by mass and only negligible amounts of heavier isotopes [1]. Since then, the H abundance is being depleted and it is being converted into He and heavier elements. Nucleosynthesis in stars is the dominant process responsible for the creation of elements from He up to Fe, except for Be and B which are mainly created in collisions between interstellar gas nuclei and cosmic rays. The amount of material heavier than He (which from now on are going to be called metals, following astronomers nomenclature) created during the evolution of the universe after the big bang correspond to $\sim 1 - 3\%$ by mass fraction [2].

Stars create metals in a variety of different ways. During most of a star's life, the principal fusion reaction is the conversion of H into He (p-p chain, CNO cycle [3]). These exothermic fusion reactions inside the star release energy that prevent its collapse due to gravitational energy. If the star is sufficiently massive, once all the

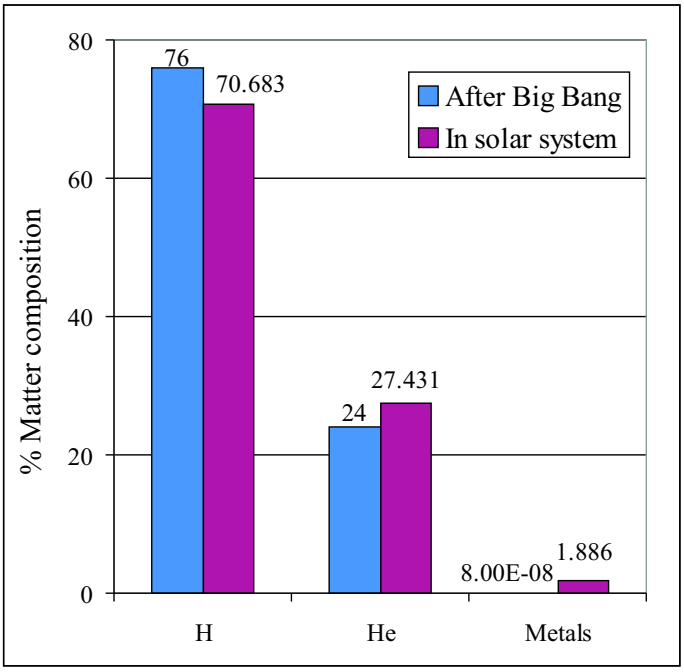

Figure 1.1: Elemental abundance composition right after the Big Bang and current solar elemental abundance composition. Images in this thesis/dissertation are presented in color.

H in the star's core has been transformed into He, the He material starts to burn into C in what is called the triple-α reaction. This process of transforming nuclei into heavier elements continues until Fe and Ni are reached and it is usually referred as stellar burning. No further fusion reactions occur after Fe because the production of any heavier elements by fusion are endothermic. Besides consuming energy, fusion into heavier elements requires a high kinetic energy due to the rise of the coulomb barrier with increasing proton number.

There are other processes contributing to the creation of elements as shown in Fig. 1.2. To produce elements heavier than Fe, two dominant mechanisms take place [4]. These mechanisms involve capture of neutrons which is not affected by an increasing coulomb barrier due to the absence of coulomb barrier to overcome. They are called the s- (slow) and r- (rapid) processes.

Even though the r-process and s-process create the majority of elements heavier than Fe, there are other nucleosynthesis processes contributing. The p-process cre-

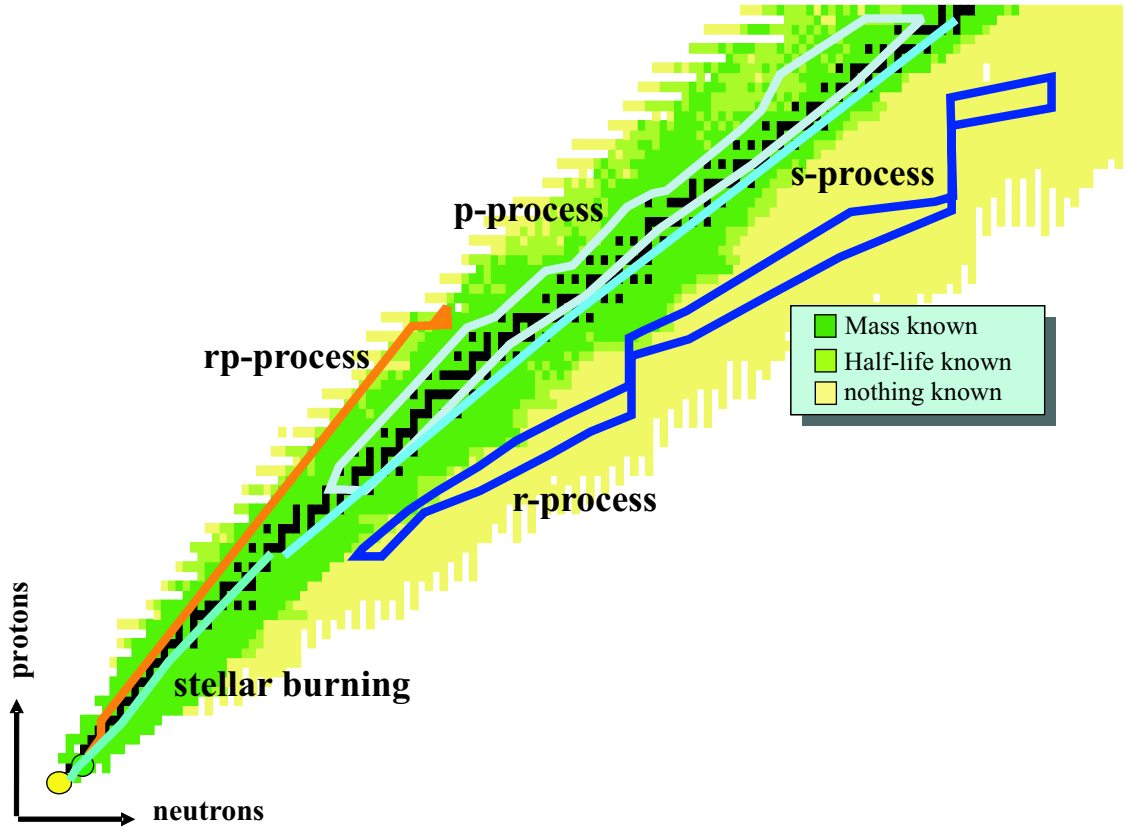

Figure 1.2: Proposed path of different nucleosynthesis processes in the nuclei chart. Black squares represent isotopes in the valley of stability, dark-green squares are isotopes with known mass, light-green squares are isotopes with unknown mass but with known half-life, and squares with yellow color are isotopes predicted to exist within theoretical proton and drip lines but with no known experimental information.

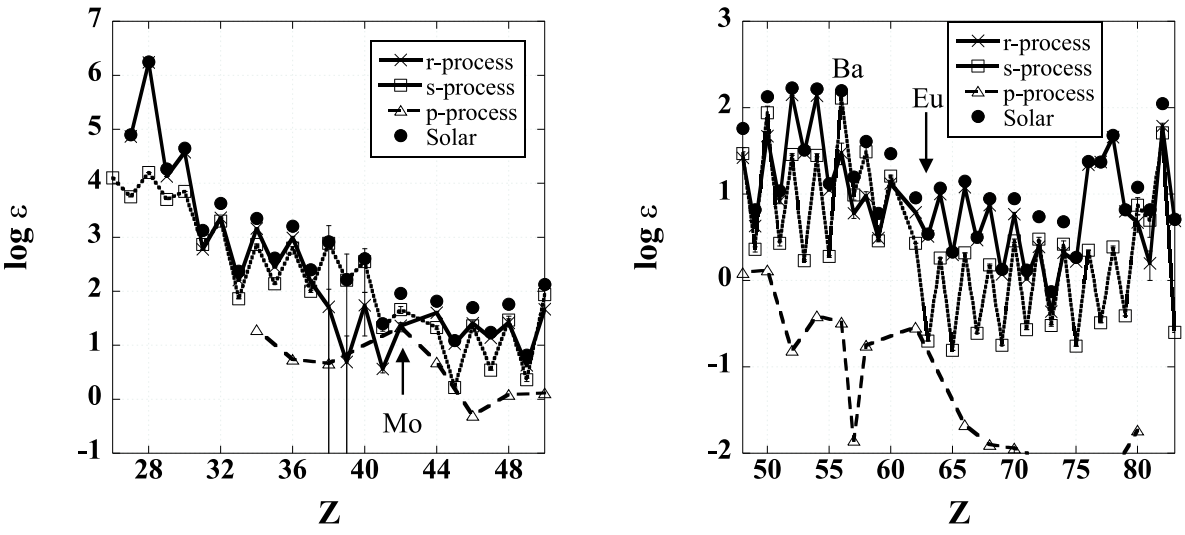

Figure 1.3: Solar abundance curves [8] (black dots) and different contributions. Dotted line is the s-process contribution from the sum of the weak [9] and main [10] component, dashed line is the p-process contribution from p-only isotopes in [8] and solid line is the r-process contribution obtained by subtracting p- and s- contributions from solar.

ates nuclei by photodisintegration of heavy seed nuclei by a series of (γ,n), (γ,p) or (γ,α) reactions. The new unstable material then decays back to stability and a new abundance pattern is obtained. A possible site of the p-process is the supernova shock passing through O-Ne layers of the progenitor star. The rp-process, on the other hand, synthesizes matter through a sequence of proton captures and β-decays along the proton-drip line. Possible astrophysical scenarios are nova explosions on accreting white dwarfs [5], X-ray bursts on accreting neutron stars in close binary systems [6] and the early neutrino driven wind in core collapse supernovae [7]. The p- and rp- processes proceed through the proton-rich side of the chart of the nuclides and therefore specific signatures of such processes can be obtained from rare p-rich nuclei.

The contributions of the major processes to the solar system abundance pattern

are shown in Fig. 1.3. The s- and r- processes are the dominant source of elements heavier than Fe and the p-process only has a significant contribution in specific cases such as Mo. It is observed that Ba is predominantly an s-process element (≈80% in solar system material) while Eu is predominantly an r-process element (≈95% in solar system material). These two elements are traditionally used as signatures of the respective process.

1.2 s-process

Heavy elements can be synthesized by exposing light nuclei to a flux of neutrons. When a nucleus (Z,A) captures a neutron, the new formed nucleus (Z,A+1) may be stable or unstable. If the nucleus (Z,A+1) is stable, it has to wait until it captures another neutron for the process to proceed. If it is unstable, it can β-decay to (Z+1,A+1) or capture a second neutron to (Z,A+2). Whichever happens faster determines what step follows. Close to stability, β-decay half-lives are typically of the order of hours or days. For very neutron rich isotopes the β-decay half-lives can go down to milliseconds. If the neutron captures are slow compared to the β-decays, the resulting path proceeds close to the valley of stability. This type of process is called the *s*-process. Nuclei with small neutron capture cross sections can be expected to have a larger abundance relative to those with high cross sections because the latter will be destroyed faster through neutron captures. Peaks in the s-process elemental solar abundance shown in Fig. 1.5(a) are due to neutron closed shells. At closed shells, the cross section to capture a neutron is reduced because the next neutron would have to occupy another energy level less bound. The Sr-Y-Zr, Ba-La-Ce-Pr-Nd and Pb peaks are due to the N=50, 82 and 126 shell closures, respectively.

In the classical s-process picture, any abundance as a function of mass number can only change by neutron captures. β-decays do not change mass number and therefore

do not appear in the equation,

$$\frac{dN_A}{d\tau} = -\sigma_A N_A + \sigma_{A-1} N_{A-1}, \tag{1.1}$$

where σ_A is an average neutron-capture cross section, the neutron exposure is defined as $\tau = \int n_n v_T dt$ and v_T is the thermal velocity of the neutrons. In steady-state, $dN_A/d\tau \rightarrow 0$ and $\sigma_A N_A =$ constant. Clayton and collaborators [11] showed that a single neutron density exposure has to be replaced by exponential distributions of exposures to correctly reproduce the solar system abundance of s-only nuclei.

The classical picture breaks down for nuclei that have comparable probabilities of undergoing β-decay or neutron captures such as ^{134}Cs, ^{148}Pm, ^{151}Sm, ^{154}Eu, ^{170}Yb and ^{185}W [12]. They are called branching points, and because isotopic abundances resulting from those branchings are temperature and neutron density dependent, the abundances of nuclei along the different branches serve as signatures of the conditions at the site of the s-process. To fully include the effect of those branching nuclei and the possibility of time dependent neutron fluxes, it is necessary to use a full network of nuclei coupled with a realistic stellar model instead of the classical picture.

It has been recognized that to correctly reproduce the solar system s-process distribution at least two different components are required [13]. The weak component of the s-process, which likely occurs in the core of massive stars ($\geq$ 15 $M_\odot$) at the He burning and to some extent, C burning stages, is responsible for the creation of elements with A$\leq$90. From stellar models the expected temperature and neutron density are in the range $T = 0.18 - 0.3$ GK and $n_n = 0.8 - 1.9 \times 10^8 cm^{-3}$, respectively [13]. The temperature in this scenario is high enough for the reaction ^{22}Ne(α,n)^{25}Mg to liberate the necessary neutrons.

The so-called strong or main component of the s-process occurs in He burning shells in asymptotic giant branch (AGB) stars. The main component is responsible for creating elements with A$\geq$ 90 [10, 14]. When the intershell between the He and

H shells in AGB stars becomes convective, protons are captured by ^{12}C forming ^{13}C via the reaction sequence ^{12}C+p$\rightarrow$ ^{13}N$\rightarrow$ $\beta+$ $\rightarrow$ ^{13}C. The dominant reaction liberating neutrons is then ^{13}C(α,n)^{16}O. In addition, after H burning in a shell has built up enough He, a He shell flash occurs expanding the star and shutting off the H burning. In the convective intershell, the reaction ^{22}Ne(α,n)^{25}Mg is also activated and a second neutron flux may occur. This neutron flux affects the final abundances of isotopes that are branching points, even though due to its low neutron production it does not contribute much to the overall element production. After the shell settles and compresses, H starts burning again and the process repeats. Such a sequence of mixing and burning in different pulses explains the overall success of the exponential distribution of neutron exposures in the classical picture. From stellar models, the ^{13}C(α,n)^{16}O reaction contributes a neutron flux of around $n_n = 7 \times 10^7$ cm^{-3} for a duration of 20000 years at T =0.09 GK. The ^{22}Ne(α,n)^{25}Mg reaction, on the other hand, contributes with a more intense neutron burst n_n =10^{10} cm^{-3} for a shorter period of time (a few years) in a hotter environment T =0.27 GK.

Traditionally the s-process pattern had been modeled using the classical approach but as the nuclear physics of more s-process branchings has been measured, more sophisticated methods have been developed. Arlandini *et al.* [10] obtained an s-process abundance pattern for the main s-process component based upon nucleosynthesis in low mass AGB stars (2 M$_\odot$ and metallicity $Z = \frac{1}{2}Z_\odot$). This stellar model is not completely parameter-free and the final abundance in their stellar model still depends on the choice of parameters such as the amount of ^{13}C. In addition, uncertainties in the neutron-capture cross sections create uncertainties in the predicted s-process abundances (δY_s). The weak s-process has been modeled by Raiteri and collaborators [9] by core burning of massive stars and the subsequent supernovae explosions included in a sequence of stellar models representing the expected range of stellar masses.

Figure 1.4 shows the total s-process contribution to the solar system abundance pattern with the contributions from the main component using the Arlandini *et al.*

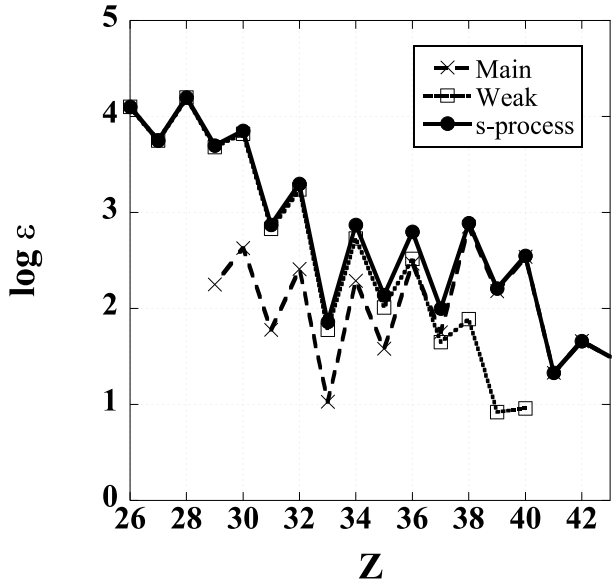

Figure 1.4: Solar s-process abundance (solid line) obtained from the sum of the weak [9](dashed line) and main [10] component(dotted line).

approach and the weak component using the Raiteri *et al.* approach.

More recently, Travaglio and collaborators [14] obtained a much improved prediction of the main component in the s-process by taking into account the contributions from a range of low to intermediate stellar masses and different metallicities. They also studied the galactic chemical evolution and predicted the s-process abundance pattern at the time of the solar system formation.

Figure 1.5(a) shows the solar s-process abundance pattern derived using the two different s-process models ([10] and [14]). The weak component is the same in both models [9]. The relative differences of both models is shown in Fig. 1.5(b). Discrepancies between the two models are observed for elements below $Z \leq 50$. While, for elements with $Z \leq 37$, the Travaglio *et al.* model creates more material, for elements in the range $38 \leq Z \leq 49$ it creates less material than the Arlandini *et al.* model.

Isotopic deficiencies in this mass region are specially problematic in the Travaglio

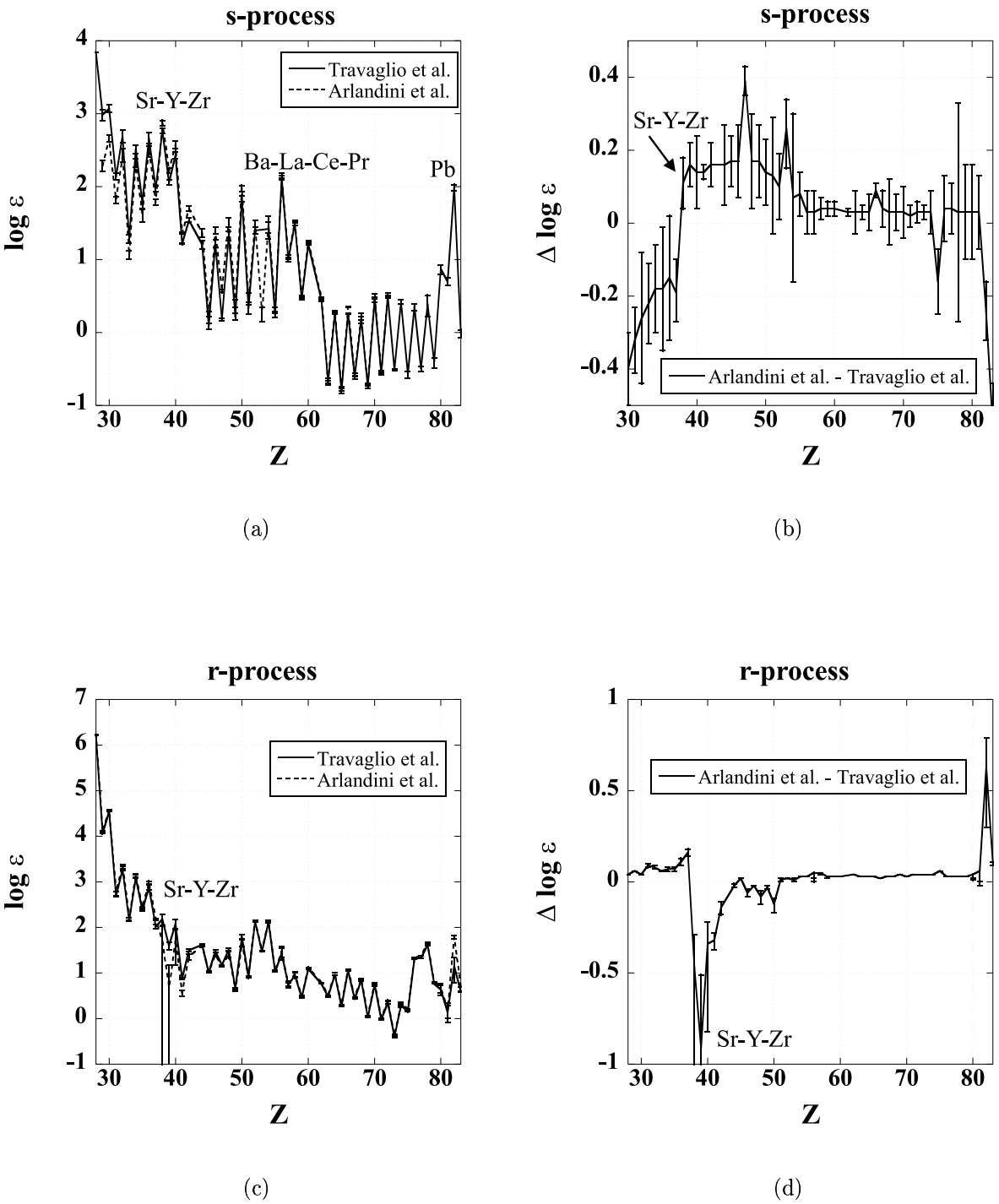

Figure 1.5: Abundance curves derived from two different s-process models. a) Solid and dashed lines are main s-process abundance curves from [10] and [14], respectively. b) Difference in the s-process abundance curves from [10] and [14]. c) Solid line is the r-process abundance curve obtained by subtracting p- and s- (from [10]) contributions from solar [8]. Dashed line results from using [14] instead. d) Difference in the r-process abundance curves that result using [10] and [14].

model because solar abundances of s-process only isotopes should come entirely from contributions from the main component of the s-process. Table 1.1 shows the contributions of the Arlandini, Travaglio and Raiteri models to some s-process only isotopic abundances. Either a third s-process component has to be included to account for such deficiencies or there is a problem in the Travaglio model. For elements with $Z \geq 50$ both models agree within the error bars and no major discrepancies are found.

1.3 r-process

The rapid neutron-capture process (r-process) is responsible for the creation of more than half the elements heavier than iron in the universe [4]. For the r-process to happen, a scenario is necessary with sufficiently high neutron density such that neutron captures occur faster than β-decays.

In the classical r-process picture, this scenario involves seed nuclei in the Fe region being bombarded with a constant neutron flux (n_n) for a fixed amount of time (τ) so that heavier nuclei are formed. Kratz *et al.* [15] showed that a single neutron exposure is not enough and that at least three components are needed to successfully reproduce the solar r-process pattern. In classical r-process calculations usually the waiting point approximation is employed. In this approximation, it is assumed that for each element Z there is a (n,γ)$\rightleftharpoons$(γ,n) equilibrium between isotopes. This equilibrium entirely determines the abundances of the different isotopes of the same element. The equilibrium abundances depend on temperature and neutron density. When equating the chemical potential of neighbor isotopes, one obtains

$$\frac{Y(Z,A+1)}{Y(Z,A)} = n_n \frac{G(Z,A+1)}{G(Z,A)} \left[\frac{(A+1)2\pi\hbar^2}{Am_u kT}\right]^{3/2} exp(S_n/kT), \qquad (1.2)$$

where $Y(Z,A)$ is the abundance defined in A, $G(Z,A)$ is the partition function, n_n is the neutron density and S_n is the neutron separation energy.

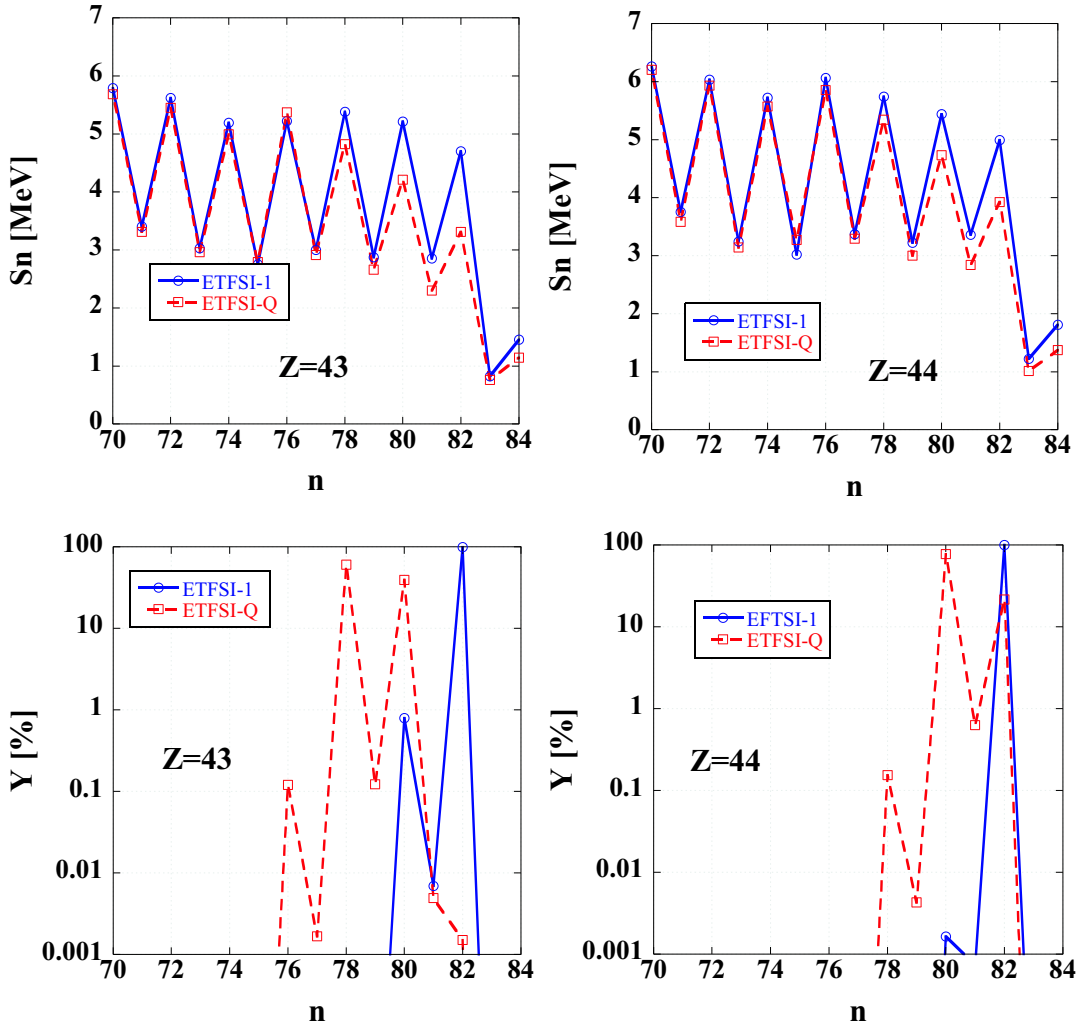

Figure 1.6: a) and b) Theoretical neutron separation energy as a function of neutron number for Tc and Ru, respectively. The solid and dashed lines show predictions based on the ETFSI-1 [16] and ETFSI-Q [17] mass models, respectively. c) and d) Normalized abundance Y as a function of neutron number for Tc and Ru, respectively. Solid and dashed line are obtained using Eq. 1.2 with $kT = 130$ keV and the predicted S_n from the ETFSI-1 and ETFSI-Q mass models, respectively

Figure 1.6 shows the theoretical neutron separation energies and the resulting normalized abundances Y as a function of neutron number for Tc and Ru isotopes when $kT = 130$ keV, which is typical for a r-process [15]. It is observed that almost all the elemental abundance is accumulated into just one or two isotopes, which are called waiting points since the half-lives of those isotopes determine how fast the material moves via β-decay to the next element. The theoretical neutron separation energies S_n used in Fig. 1.6 are predicted using the ETFSI-1 [16] and ETFSI-Q [17] mass models. These mass models are further explained in Section 4.1 but among other differences, the ETFSI-Q model predicts a smaller neutron separation energy for the most neutron-rich isotopes than the EFTSI-1 model. This difference in S_n results in different isotopes being waiting points. For Tc, the most abundant isotope changes from ^{125}Tc using the EFTSI-1 model to ^{121}Tc and ^{123}Tc using the ETFSI-Q model. A similar change occurs for Ru. This reduction in the neutron separation energy therefore has an effect on the final abundance pattern because the material that has been waiting to β-decay when the neutron flux is exhausted (refered as freeze-out) would β-decay to different stable isotopes depending on which mass model is used. The r-process path is defined as the collection of isotopes with the largest abundances for every element. Because during the r-process, the neutron density and the temperature are expected to change as a function of time, the waiting points also change. Waiting points have an S_n that correspond to a value from 0 to $\sim$5 MeV. This change in neutron density and temperature produces a "widening" of the most abundant isotope per element, and it is modeled using different components (n_n,T,τ) in a classical r-process calculation.

Solid and dashed lines in Fig. 1.7 are the predicted abundance patterns using a classical r-process calculation with a combination of different components (n_n,T,τ) best fitted to reproduce the solar system r-process abundance pattern (how to obtain this abundance is explained in Section 1.3.1) while using two different mass models. Solar r-process abundances are shown as dots in the figure. The same stellar condi-

Table 1.1: Contributions in percent from different models to s-process only solar system abundances.

s-only isotope	Main component		Weak component
	Arlandini *et al.* [10]	Travaglio *et al.* [14]	Raiteri *et al.* [9]
^{86}Sr	47%	52%	24%
^{93}Nb	85%	67%	
^{96}Mo	106%	78%	
^{100}Ru	95%	73%	
^{104}Pd	106%	78%	
^{110}Cd	97%	71%	

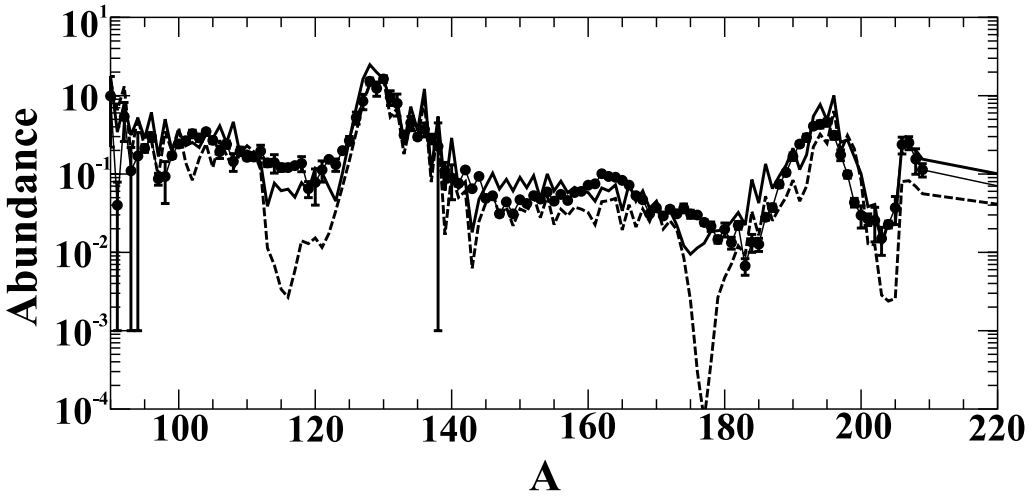

Figure 1.7: Solar r-process abundances (dots) and abundances predicted using the classical r-process model. The solid line shows the predictions based on the ETFSI-Q mass model assuming quenching of the neutron shell gaps far from stability. The dashed line shows the predictions based on the ETFSI-1 mass model without such shell quenching. Figure taken from [15].

tions were used while using the ETFSI-1 and the ETFSI-Q mass models. As it can be seen in the graph, while there is a successful reproduction of the positions and relative heights of the abundance peaks, there are also some deficiencies or abundance troughs at $A \approx 115$ and $A \approx 175$. These features have been interpreted as signatures of nuclear structure for extremely neutron-rich nuclei [15]. In this framework, the observed troughs have their origin in an overestimation of the N=82 and the N=126 shell gap strengths far from stability. This gap size of the shell closures is embedded in the predicted neutron separation energies and thus it is reflected into the predicted abundances. The solid line in Fig. 1.7 is the result of the calculation using the ETFSI-Q mass model and it shows an improvement to the overall fit compared to the ETFSI-1 masses. The ETFSI-Q mass model includes a phenomenological weakening of the neutron shells. In particular, the abundance trough around $A \approx 115$ and $A \approx 175$ are eliminated to a large extent when using the ETFSI-Q mass model. It has been suggested [15] that this result may indicate such weakening of the neutron shell closures for nuclei far away from stability. Nuclear structure properties of nuclei in this region indicating such weakening are mentioned in Section 2.2.

As noticed before, the β-decays from one isotopic chain to the next allow the r-process to create heavier elements and determine the speed at which the heavy nuclei are formed. Of particular importance within the r-process are the so-called bottle-necks, or isotopes with particularly long half-lives. These bottle-neck isotopes are typically located at shell closures where the sudden drop in the neutron separation energy makes photodisintegration more favorable. Because the neutron-rich isotope cannot capture anymore neutrons before it photodisintegrates, it has to wait to β-decay to capture another neutron. If the neutron shell closure is strong, the same process repeats and the ensuing isotopes are driven closer to stability. As the path gets closer to stability, the half-lives get longer and those isotopes become the longest waiting points in the r-process. Between waiting points at closed shells, the timescales of β-decays along the r-process path are one or two orders of magnitude shorter.

The ratio of neutron-to-seed nuclei has to be around 100 to 150 in order to produce elements up to Pt, Th or U. When the neutron flux is exhausted, nuclei in the r-process path decay back to stability through a series of β-decays, sometimes accompanied by β-delayed neutron emission.

1.3.1 Stellar Observations

As it has been mentioned before, elements above Fe are created mainly in the r-, s- and, to a lesser degree, in the p-process. The r-process is one of the least understood processes because it involves extremely neutron-rich isotopes which are difficult to study experimentally and because it requires the most extreme astrophysical conditions. Because of that, any calculation has to rely on theoretical models that are based on our knowledge of nuclear structure properties of known nuclei. How nuclear structure properties change from nuclei close to stability to extremely neutron-rich nuclei is not well understood. Furthermore, the astrophysical scenarios in which a r-process may occur are still a matter of debate. Since the s-process is relatively well understood compared to the r-process, its calculated abundance pattern is used to obtain the solar system r-process abundance pattern by subtracting it from the total solar abundance $Y_r = Y_\odot - Y_s - Y_p$.

Fig. 1.5(c) shows the solar r-process abundance pattern after subtraction of the s- and p- components from the solar system abundance. Because of the mentioned discrepancy in the calculated s-process abundance pattern, two different r-process abundance distributions are obtained. The relative differences of the solar r-process abundance derived using both models is shown in Fig. 1.5(d). The main difference in the solar r-process contributions are in the predictions of Sr, Y and Zr elements. Using the s-process contribution from Arlandini *et al.* [10], the solar r-process contribution has smaller amounts of Sr, Y and Zr material than using the s-process calculations from Travaglio *et al.* [14].

Recently r-process-enhanced metal-poor stars have been discovered that allow

one to directly observe the r-process elemental abundance pattern. Because metal-poor stars ([Fe/H] <1) are believed to be old stars formed from material not yet mixed and processed as much as in our solar system (therefore the low metallicity), their abundance patterns reflect the matter composition of just a few nucleosynthesis events. The interstellar material from which the star was formed is reflected in the unburned star's surface material. High resolution spectroscopy observations from stars allow us to know the composition of the surface. In addition, the main component of the s-process occurs in low or intermediate stars of 1-8 solar masses. These stars have long evolutionary time scales of the order of billion of years. Because it is believed than the r-process is related to stars heavier than 8 solar masses which live only a million years, the products of the s-process take longer to be created and ejected into the interstellar medium. For these reasons, there are metal-poor stars that formed out of material exposed mainly to an r-process event. Detailed abundance patterns of r-process enhanced metal-poor stars are therefore extremely useful to identify signatures of the r-process.

Recent comprehensive studies of the metal-poor stars CS 22892-052 [19] ([Fe/H]=-3.1), HD 155444 [20], BD $+17^o3248$ [21] and CS 31082-001 [22] are shown in Fig. 1.8 and Fig. 1.9. The scaled solar system r-process abundances are also shown for comparison. While CS 22892-052 and 31082-001 belong to the subclass of highly r-process enhanced stars (r-II) for which [Eu/Fe]>+1.0 and [Ba/Eu]<0, HD 155444 and BD $+17^o3248$ belong to the subclass of moderately r-process enhanced stars (r-I) for which $0.3 \leq$[Eu/Fe]$\leq +1.0$ and [Ba/Eu]<0. Metal poor r-process enhanced stars r-I and r-II exhibit abundance ratios of r-process elements such as Eu, Os and Pt much larger than observed in the sun in spite of their relative low Fe abundance. The fact that r-process elements are enriched, allow astronomers to observe their absorption lines because otherwise those lines would be too weak to detect for most elements.

For Ba (Z=56) and heavier elements, the scaled solar r-process abundances agree very well with the abundances in metal poor stars as shown in Fig. 1.8 and Fig. 1.9.

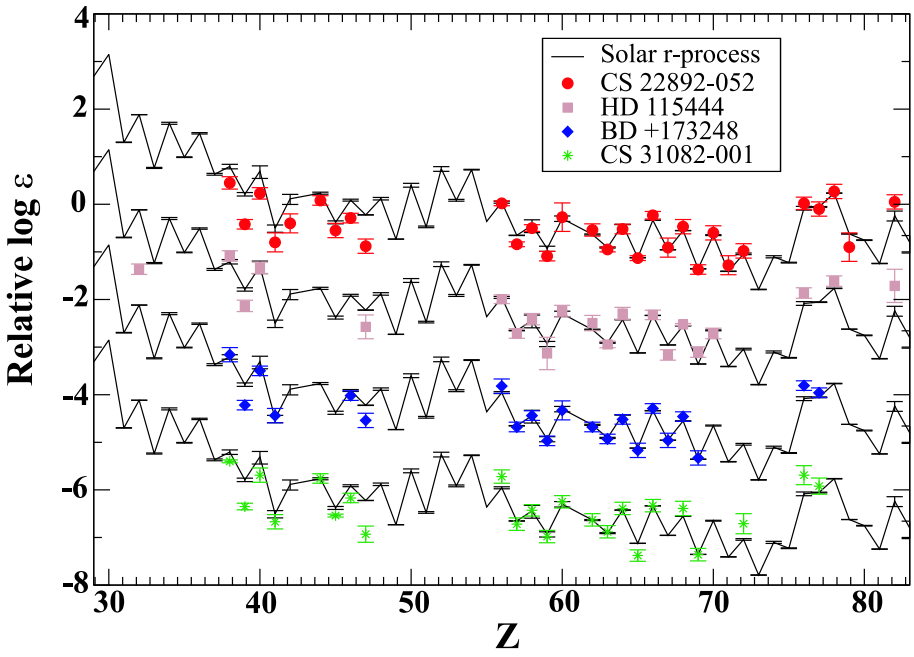

Figure 1.8: Elemental abundance pattern of r-process rich stars CS 22892-052, HD 155444, BD $+17^o$3248 and CS 31082-001 compared with solar r-process abundance derived using the s-process contribution from Travaglio et al. [14]. Abundances have been shifted for all stars for display purposes. Adapted from [18].

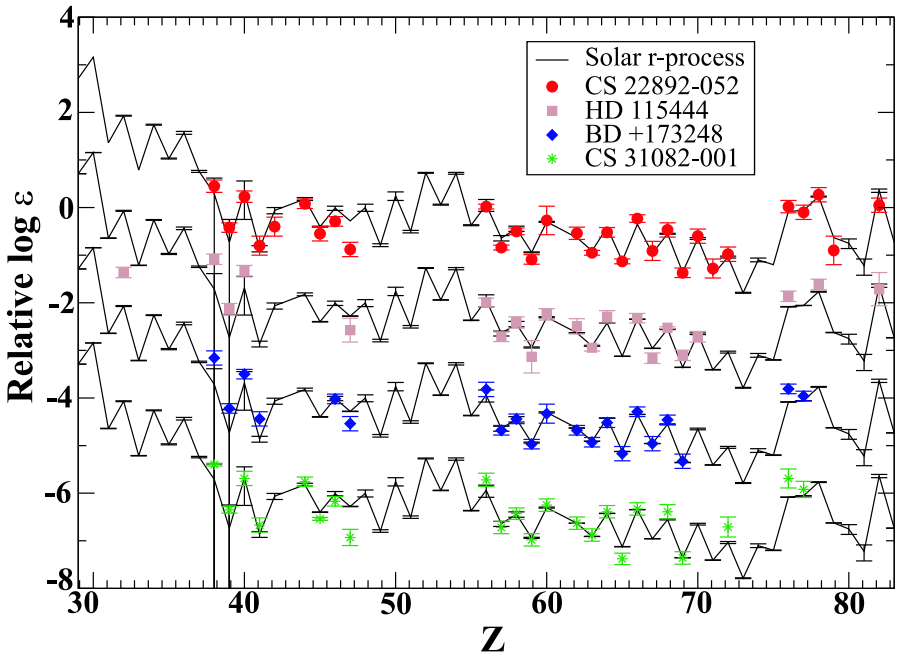

Figure 1.9: Elemental abundance pattern of r-process rich stars CS 22892-052, HD 155444, BD $+17^o$3248 and CS 31082-001 compared with solar r-process abundance derived using the s-process contribution from Arlandini et al. [10]. Abundances have been shifted for all stars for display purposes. Adapted from [18].

Even though the absolute values differ, the relative abundances are pretty similar. For lighter elements in the Z=40-50 range, abundances from the metal-poor stars do not agree as well as for the heavier elements compared with the solar abundances. Chapter 5 discusses these discrepancies and possible astrophysical scenarios in which a different nucleosynthesis process may produce them.

1.3.2 Proposed sites of the r-process

Possible sites where the r-process may happen require a high density of free neutrons. This condition is satisfied in supernovae and neutron star mergers, which are the most accepted candidates for possible sites. Within the supernova site, two possible scenarios have been discussed in literature, the neutrino-driven wind model and prompt explosions.

The neutrino-driven wind model in supernovae has been studied widely in the literature [23–26]. When a supernova occurs, the stellar core collapses into a neutron star. The gravitational binding energy that the neutron star liberates is $\sim 10^{53}$ erg, most of which is released by the emission of $\nu_e, \bar{\nu}_e, \nu_\mu, \bar{\nu}_\mu$ and $\bar{\nu}_\tau$ neutrinos. Near the newly forming proto-neutron star, matter is completely dissociated into neutrons and protons. When some of the energy released from the neutron star in the form of neutrinos passes through this material, some of the neutrinos are captured by the neutrons and protons by the reactions,

$$\nu_e + n \rightarrow p + e^- \tag{1.3}$$

$$\bar{\nu}_e + p \rightarrow n + e^+. \tag{1.4}$$

These reactions transfer energy to the material which leads to heating and produces a mass outflow. Besides depositing energy, the neutrino captures change the neutron-richness of the material. Because the antineutrinos come from deeper regions in the neutron star, they are more numerous than the neutrinos, and have a

higher average energy and higher luminosity, equation 1.4 dominates and the material becomes more neutron-rich [27]. The outflow of material is usually referred as the neutrino-driven wind [28]. As the wind expands, its temperature and density change producing new reactions that change its composition. When the temperature drops to $\sim$0.5 MeV, protons and neutrons assemble into α-particles; eventually, when the temperature drops further, an α-process starts in which neutrons and α-particles are captured into heavier nuclei [29]. When the temperature reaches $kT \sim$0.25 MeV, the coulomb barrier prevents charge-particle reactions. At this point, nuclei up to $A \sim 90$ have been produced. The remaining neutrons start to be captured by the newly formed heavy nuclei during the subsequent r-process.

One way to parametrize such r-process is using the entropy of the system, the ratio of neutrons to protons, and the expansion timescale. If the entropy is low, a very neutron-rich environment is needed for the r-process to happen. Conversely, if the entropy is high enough, even a small excess of neutrons over protons allows the process to happen. Current models however do not achieve sufficiently high entropy for the expected neutron richness for an r-process to reach the heaviest nuclei.

Another suggested scenario in the same site are prompt supernova explosion models. During the core collapse, high densities allow the creation of neutrons by electron capture thus decreasing the electron pressure. Infalling material interacts with those neutrons close to the resulting proto-neutron star resulting in a r-process. Even though the collapse of O-Ne-Mg cores of stars in the 8-10 $M_\odot$ seemed promising candidates [30], recent calculations do not reach the low entropies and high neutron density necessary to produce an r-process [31].

A second suggested r-process site is a neutron star merging with another neutron star or a black hole [32–37]. The basic idea is that after the neutron stars have come into contact, a rapidly spinning object with mass of around 3 $M_\odot$ forms surrounded by a thick disk of a few times 0.1 $M_\odot$ and a low density region. Besides the cooling due to an expansion caused by angular momentum, the temperature changes due

to nucleosynthesis releasing nuclear binding energy and heating up the material. An r-process proceeds inside this neutron-rich material. Due to the material being so neutron-rich, the required entropy does not have to be as high as in the supernova site scenario. Due to angular momentum conservation, some of the material avoids collapse and matter from the neutron star is ejected. Neutron star mergers occur at a rate $\sim 10^3$ lower than supernovae and therefore there are fewer events to create heavy elements. Argast *et al.* [38] showed that the amount of r-process material generated in neutron star mergers would lead to a scatter in the [Eu/Fe] ratio that is too large compared to the one observed.

As pointed out in [39], comparing Eu and Ge abundances in halo stars of different iron abundances suggests different production sites for Eu and Ge. The ratio [Eu/Fe] seems to decrease over time and it shows a large scatter for very old stars that reduces over time. On the other hand, the [Ge/Fe] ratio shows little scatter suggesting it does not change much over time. The large chemical inhomogeneity at early times in the galaxy when some of these stars were formed explains the large scatter. As more material went through r-process events, chemical abundances were homogenized resulting in less abundance scatter. Because Ge has not changed its relative abundance over time, maybe it has been produced in a large number of r-process events, while Eu has only been produced in some of those events and that is why more time is required to smooth out the inhomogeneities. A possibility is that perhaps the r-process occurs in more than one scenario resulting in different abundance yields and rates of production.

Recently, prospects of obtaining an r-process from gamma ray burst disk winds has been discussed in the literature [40]. Gamma ray bursts occur in rare supernovae (collapsars) or in some neutron star mergers. In both cases, an accretion disk forms around a black hole. The key to obtain the necessary neutron-rich material are neutrinos emitted from the disk. To make the outflow material have the right neutron excess, electron capture and electron antineutrino capture must dominate. Depend-

ing on the accretion rate, the viscosity and the angular momentum of the material a r-process may proceed if the entropy is low.

It is difficult to pinpoint an exact location of the r-process due to our insufficient understanding of how supernovae explode and the properties of neutron stars. Among the problems with the supernovae scenario is the incomplete understanding in the role of neutrinos, the hydrodynamics of the material in 3D simulations, the equation of state and the explosion mechanism. Therefore, how the process happens in either scenario is still an unresolved question.

Chapter 2

Nuclear Physics

2.1 Relevant nuclear physics properties

As mentioned in the previous chapter, the r-process path is determined by neutron separation energies (S_n) and partition functions. The *location* of the solar r-process abundance peaks are determined by the r-process path and therefore depend on the underlying nuclear structure.

β-decay half-lives ($T_{1/2}$) determine the speed of the process toward heavier elements for a given set of astrophysical conditions. In addition, waiting points with long $T_{1/2}$ serve as bottlenecks where material accumulates. The *height* of the peaks in the r-process elemental solar abundance distribution can therefore be explained by the long half-lives of some of the involved nuclei at the magic numbers N = 50, 82 and 126.

Once the neutron freeze-out occurs, very neutron-rich nuclei decay back to stability through a series of β-decays with branchings for β-delayed neutron emission (P_n) further affecting the final abundance pattern. In addition, the β-delayed neutron emission releases neutrons which increase the neutron abundance during freezeout.

Besides the neutron separation energies, partition functions, β-decay half-lives ($T_{1/2}$) and β-delayed neutron emission probabilities (P_n), individual neutron capture

cross sections may be important while the neutron flux is disappearing and there is a breakdown of the equilibrium conditions. Depending on the site where the r-process takes place, neutrino interactions may also play a role [41].

Fission occurs for very heavy nuclei produced in the r-process. Decays may occur through spontaneous fission or neutron capture induced fission when nuclei are produced at excitations energies above their fission barriers. Fission of heavy nuclei prevents the creation of nuclei heavier than A>256. Besides depleting the heaviest isotopes produced in the process, fission increases the abundance of the light isotopes that serve as seed nuclei and the amount of available neutrons.

2.2 A=112-123 mass region

The A=112-123 mass region is of considerable importance for r-process studies. In this region, r-process models do not produce sufficient amounts of nuclei to explain the solar system elemental abundances as shown in Fig. 1.7. As mentioned in Section 1.3, it has been suggested that this problem may be due to the incorrect strength of the shell closure used in theoretical mass models because the problem can be alleviated to some extent by assuming a reduction of the N=82 shell gap far from stability [42].

Since the region around N=82 is responsible for the formation of the $A \approx 130$ peak in the solar r-process abundance pattern, this mass region has been of considerable theoretical and experimental interest. Figure 2.1 shows the limit where experimental information had been obtained before this work in the region below the N=82 shell closure. Isotopes with at least an experimentally known half-life are shown to the left of the dashed line in Fig. 2.1. A β-decay half-life is a global quantity and it is one of the "easiest" nuclear structure properties to measure.

In section 2.1 the relevant nuclear properties necessary to correctly model the r-process were mentioned. Because the progenitors of only a few nuclei in the r-process path have been studied experimentally in the A=112-130 mass region, theoretical

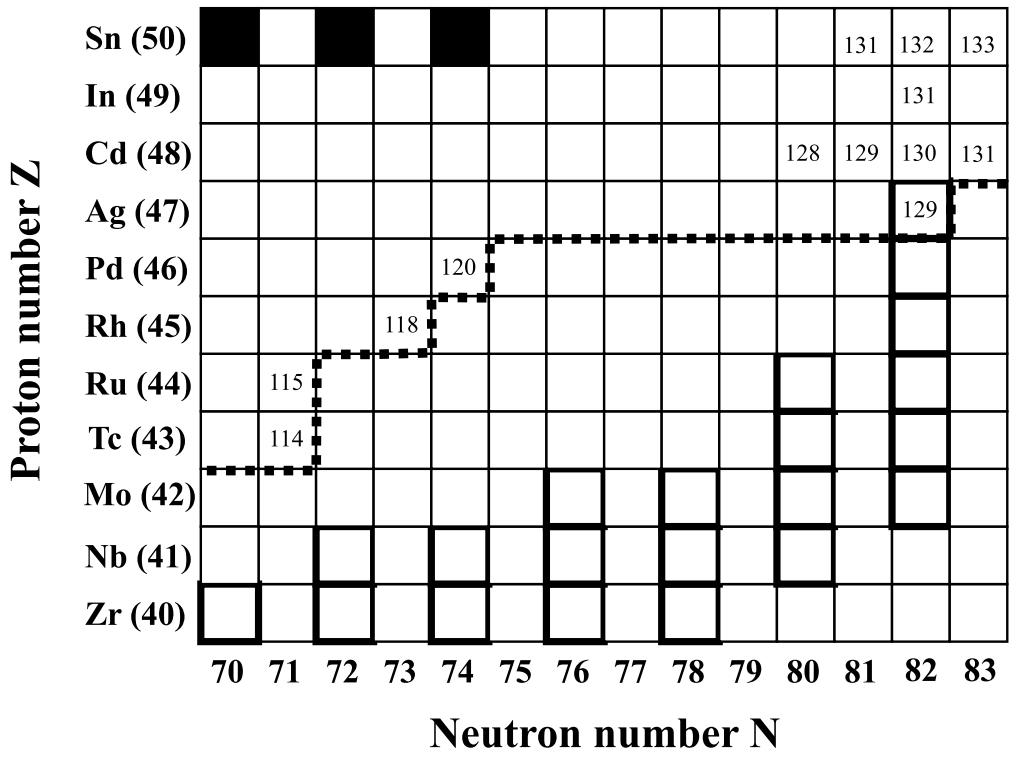

Figure 2.1: ^{110}Zr to ^{133}Sn mass region. Isotopes with previously known half-lives are shown to the left of the dashed line. Isotopes mentioned in the text are also shown. The r-process waiting points predicted with the ETFSI-Q mass model in the classical r-process model [43] are framed with black thick lines.

models are required. Theoretical models are based on nuclear properties of experimentally known nuclei. In this section relevant experimental properties in this mass region are discussed.

Particularly important are properties from the neutron-rich double-magic nucleus $^{132}_{82}Sn_{50}$, proton single-particle $^{133}_{82}Sb_{51}$, neutron single particle $^{133}_{83}Sn_{50}$, proton single-hole $^{131}_{82}In_{49}$ and neutron single-hole $^{131}_{81}Sn_{50}$. Their properties are needed to constrain single particle energies in shell model calculations and other microscopic nuclear structure calculations.

Experimental information for very neutron-rich Ag to Sb isotopes has been obtained mainly through β-decay spectroscopy mainly at OSIRIS and CERN-ISOLDE. Among the 1p or 1h isotopes, the structure of the closest isotopes to stability $^{131}_{81}Sn_{50}$ (ν-hole) and $^{133}_{82}Sb_{51}$ (π-particle) have been known for more than a decade. Energy

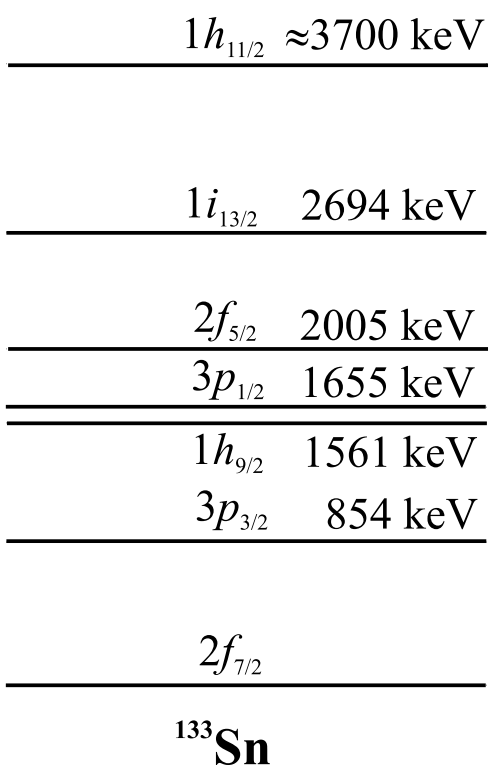

Figure 2.2: Experimental level scheme of ^{133}Sn and assigned single-particle states.

levels in ν-particle $^{133}_{83}Sn_{50}$ have been identified more recently [44] and they are shown in Fig. 2.2. Using a Nilsson model, Pfeiffer and collaborators [42] showed that by reducing the spin-orbit interaction from the standard value, the correct energy of the $\nu p_{3/2}$ and $\nu p_{1/2}$ levels in $^{133}_{83}Sn_{50}$ is obtained; otherwise, those energy levels are located more than 2 MeV higher than the measured values.

For π-hole $^{131}_{82}In_{49}$ only the half-life and the energy of the first two excited states are known and more experimental information is needed. Recently, spectroscopy became available for ^{130}In [45]. The high measured energy of the $[\pi g_{9/2}^{-1} \otimes \nu g_{7/2}^{-1}]$ 2QP 1^+ state is determined by the difference in the strength of the proton-neutron interaction between $\pi g_{9/2}^{-1}$ and $\nu g_{7/2}^{-1}$ relative to $\pi g_{9/2}^{-1}$ and $\nu h_{11/2}^{-1}$. The location of the orbitals $\nu g_{7/2}$ and $\nu g_{11/2}$ is also important when determining the location of the 2QP 1^+ state. The proton-neutron interaction was artificially changed in the shell-model code OXBASH [46] to calculate the correct energy placement, and if that interaction is maintained at the shell closure down to Zr, the half-lives of ^{128}Pd to ^{122}Zr become longer [45]. However, the reason for such change is not understood and more experimental information is required.

For $^{130}_{82}Cd_{48}$ only the ground state half-life and energy of the first excited state is known. At N=83, the measured half-life of ^{131}Cd (68$\pm$3 ms) is short compared to global theoretical predictions from QRPA calculations [47] (943 ms) that use the FRDM [48] mass model. In addition, the experimental P_n value (3.4$\pm$1%) is smaller than predicted (99%) when using the same theoretical calculation. Hannawald *et al.* [49] using the Q_β value predicted in the Audi *et al.* mass evaluation [50], which agrees with the ETFSI-Q mass model [17] but not the FRDM mass model, as inputs of the QRPA calculation and including first forbidden transitions correctly calculated the experimental $T_{1/2}$ and P_n value.

Level systematics of Cd isotopes up to N=82 have been obtained [42] and in particular $E(2^+)$ and $E(4^+)$ (energy of the first 2^+ and 4^+ states in even-even nuclei, respectively) level systematics have been measured up to ^{128}Cd. The behavior of

$E(2^+)$ is a good indication of nuclear structure and of collective properties when compared systematically between even-even isotopes of the same element. Away from shell closures, collective behavior prevails and the nucleus displays features that can be described as the rotation of a statically deformed shape. Due to collective interactions among many nucleons the energy of the first 2^+ state is lowered in comparison with the value at the shell closures where single particle excitations can usually explain the low energy level structure of the nucleus. Similarly, the ratio $E(4^+)/E(2^+)$ is a good indication of deformation. Away from shell closures, this ratio is almost constant and close to shell closures sharply decreases. The experimental ratio $E(4^+)/E(2^+)$ of neutron-rich Cd isotopes is almost unchanged (≈ 2.25) up to ^{126}Cd. There is a small decrease of that ratio in ^{128}Cd which contrasts with the more dramatic decrease in neighboring even-even Sn and Te isotopes. Such a reduction would be consistent with a weakening of the shell strength seen by the Cd isotopes [42].

Dillmann *et al.* [45] studied the r-process waiting point ^{130}Cd and pointed out that the measured Q_β value agrees with recent mass models that include a reduction of the shell strength at N=82, usually referred as shell quenching. The measured Q_β value is higher than the predictions from models with a strong N=82 shell closure such as the finite range droplet model (FRDM) [48], ETFSI-1 [16] and the Duflo-Zuker mass formula [51]. However, even though "shell quenching" models as the Hartree-Fock-Bogoliubov Skyrme force P HFB-SkP [52] and the ETFSI-Q [17] are in much better agreement, others as the most recent microscopic HF models [53, 54] predict a lower Q_β value than measured by up to 1 MeV.

The observations of the mentioned low-lying $\nu p_{3/2}$ and $\nu p_{1/2}$ single-particle levels in $^{133}_{83}Sn_{50}$, the experimental systematics of the ratio $E(4^+)/E(2^+)$ of neutron-rich Cd isotopes, the observation and explanation of the short $T_{1/2}$ and P_n value of ^{131}Cd and the large ^{130}Cd Q_β are evidence of shell quenching for Cd, In and Sn isotopes.

Figure 2.3 shows the difference $S_n(82) - S_n(84)$ as a function of proton number. Such difference can be interpreted as the strength of the shell closure because

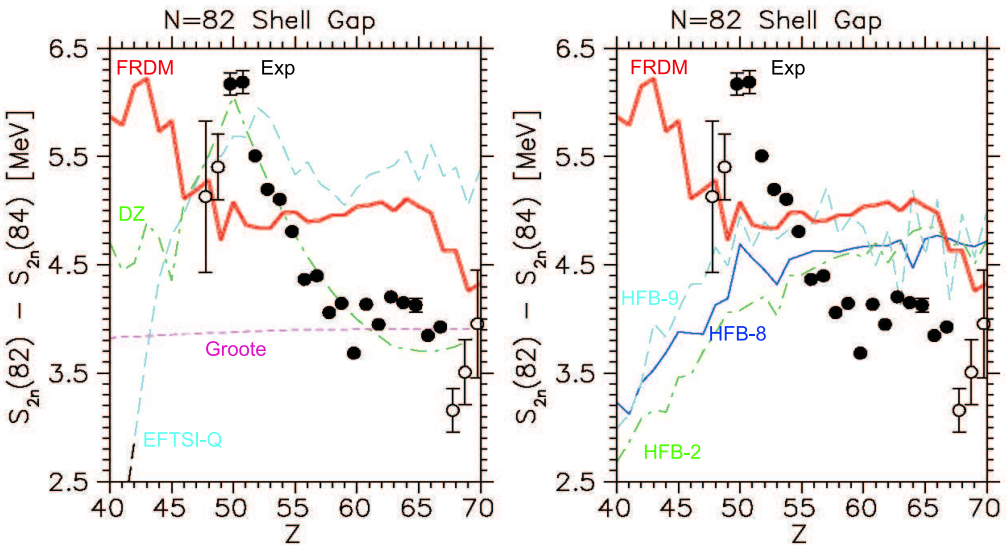

Figure 2.3: Difference of two-neutron separation energy as a function of proton number at the N=82 shell closure. Solid circles represent direct mass measurements. Open circles are results obtained by an indirect measurement such as a Q_β value. Solid and dashed lines are theoretical predictions from different models. Courtesy of K.-L. Kratz.

it represents the steepness of the *slope* of the neutron separation energy as a function of neutron number after N=82 as shown in Fig. 1.6 a) and b). Coming from the "proton-rich" side, the experimental values show a sharp peak with a maximum around Z=50. In principle, one should expect a close to symmetric decrease on the "neutron-rich" side and the two experimental values seem to be in agreement. If the notion of symmetry is maintained as the proton number is decreased, one could expect the experimental values to follow a path close to the ETFSI-Q predictions at least until the difference flattens out as it did on the "proton-rich" side. This may be further indication of a weakening of the shell closure at N=82.

So far, most of the experimental studies in the very-neutron rich Tc-Pd region have been done at the IGISOL facility in Jyväskylä, with spectroscopic and β-decay information having been obtained for nuclei up to ^{114}Tc [55], ^{115}Ru [56], ^{118}Rh [57] and ^{120}Pd [58]. More recently, Walters *et al.* [59] reported the measurement of the energy of $E(2^+)$ in ^{120}Pd resulting from the β-decay of ^{120}Rh at the NSCL at MSU.

In this region, the dominant β-decay transition takes place via the transformation of a $g_{7/2}$ neutron into a $g_{9/2}$ proton. In even-even nuclei, decay typically occurs through $0^+ \rightarrow [\pi g_{9/2} \otimes \nu g_{7/2}^{-1}]$ 2QP 1^+ β transitions. The GT β-strength is distributed over several states due to deformations.

Comparing the known low-energy structure of N$\leq$74 Pd isotopes and the isotonic Xe isotopes, Walters and collaborators concluded that Pd and Xe isotopes share the same N=82 shell structure. If shell quenching is defined as a reduction of the shell gap compared to the largest gap (Z=50 in the difference $S_n(82) - S_n(84)$ shown in Fig. 2.3), then Walters' conclusion suggests the existence of shell quenching for both Pd and Xe isotopes. On the other hand, if shell quenching is defined as the existence of an additional shell gap reduction far from stability on top of the shell gap reduction observed on the "proton-rich" side in Fig. 2.3, Walters' conclusion would indicate no shell quenching for the Pd isotopes.

All these observations make the need of nuclear experiments extending the boundary of known nuclei crucial for our understanding of nuclear structure in this mass region. In this work, we extend the limit of known β-decay half-lives and β-delayed neutron emission probabilities P_n further toward the r-process path by measuring β-decay half-lives $T_{1/2}$ of very neutron-rich $^{114-115}$Tc, $^{114-118}$Ru, $^{116-121}$Rh and $^{119-124}$Pd and P_n values (or upper limits) for $^{116-120}$Rh, $^{120-122}$Pd and $^{122-124}$Ag isotopes. Fig. 2.4 shows the region of interest. Chapter 3 discusses the experiment and results. Analysis and implications in the r-process are discussed in Chapter 4.

The measured P_n values are direct inputs of r-process models and even though $T_{1/2}$ and P_n values are global quantities they provide first experimental clues on masses, shapes, and β-decay strength functions far from stability. The half-life measurement contains information about low-lying β-decay strength while the P_n value is sensitive to the strength just above the neutron separation energy. These measurements also provide an important test for the theoretical predictions used for the majority of the nuclear physics calculations in r-process models.

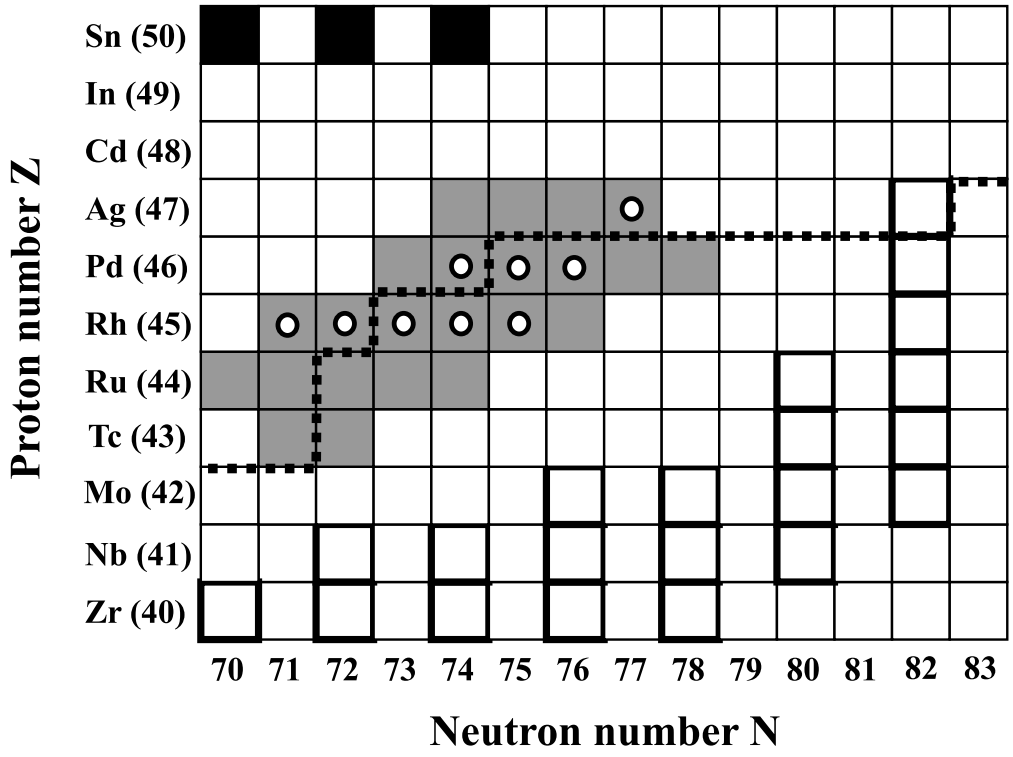

Figure 2.4: ^{110}Zr to ^{133}Sn mass region showing the region of interest. Isotopes with previously known half-lives are shown to the left of the dashed line. A half-life measurement for the isotopes colored in gray was obtained and for isotopes with open circles a new P_n value was measured. The r-process waiting points predicted with the ETFSI-Q mass model in the classical r-process model [43] are framed with black thick lines.

2.3 Sr-Pd region

The presence of discrepancies between the abundance pattern of the r-process solar abundances and the metal-poor stars in the $Z = 38 - 47$ region hints at an additional process contributing in this region. The need of nuclear data to correctly model the r-process in order to correctly disentangle the various contributions of neutron-capture processes makes experimental information essential.

In Chapter 5 the need of an additional neutron-capture process is discussed and the necessary astrophysical conditions are studied. Network calculations used in that chapter required the use of theoretical models. Of particular importance in the results is the possible doubly semi-magic number ^{110}Zr. A strongly quenched model may result in almost no deformation around $Z = 40$ and $N = 70$ [60]. Due to the interplay of collective and single-particle excitations, the region around the Zr isotopes has a concentration of rapidly evolving shapes and excitation modes within a small mass range. As the classical neutron shell closure at N=50 is filled, a sudden increase in deformation is observed near N=58. In this region, reducing pairing correlations by exciting particles into higher-lying orbitals still results in an increase in the binding energy through a gain in the proton-neutron interaction. When the radial overlap between the neutrons and the protons is maximal, this gain in binding energy is maximized.

Most of these studies up to N$\approx$ 66 took place at small ISOL facilities and by using GAMMASPHERE or EUROGAM. As the neutron number is increased this strong deformation must change to a spherical shape at N=82. Recent calculations on shape deformations [61,62] have shown complex energy landscapes with several minima and the presence of tetrahedral symmetry has been suggested. More experiments are to come and we will have a more through understanding of the nuclear structure in this mass region.

Chapter 3

β-decay studies in the Tc-Ag region near to the N=82 shell closure

3.1 Experimental setup

3.1.1 Isotope Production

Radioactive isotopes are produced at the National Superconducting Cyclotron Laboratory (NSCL) at Michigan State University using projectile fragmentation. In this technique, a primary ion beam is accelerated to relativistic energies before hitting a target. Some of the primary beam nuclei continue as degraded primary beam while some interact with the target creating new fragments. Because of their high velocities, the resulting fragments proceed with forward momenta to a fragment separator. At the focal plane of the fragment separator, nuclei are physically separated depending on their nuclear charge Z and ratio of atomic number over atomic charge (A/Q). This method, referred as $B\rho - \Delta E - B\rho$, makes use of a degrader located at the dispersive plane of the separator where beam particles lose different amounts of energy depending mainly on Z. Once the nuclei of interest has been isolated, the selected isotopes are sent to an experimental vault were nuclear properties can be further studied. A

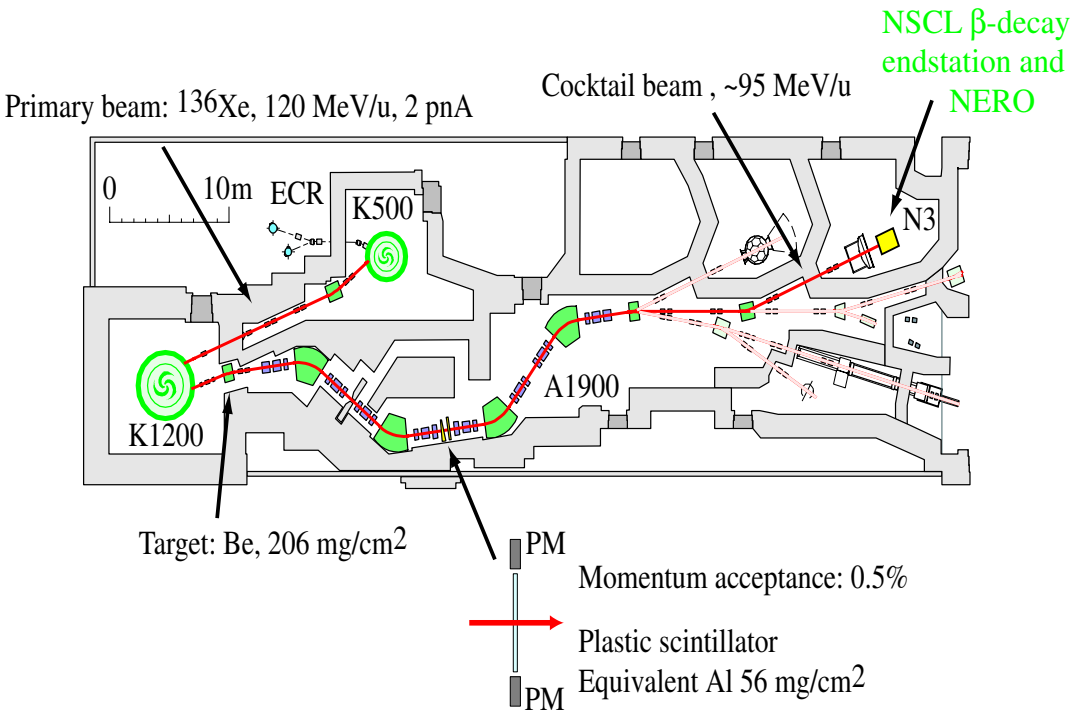

Figure 3.1: Schematic diagram of the NSCL.

schematic layout of NSCL is shown in Fig. 3.1.

In the current experiment (NSCL 02032), nuclei of interest consisted of neutron-rich Tc, Ru, Rh, Pd and Ag isotopes. A 1.4 pnA average intensity ^{136}Xe beam (primary beam) with an energy of 121.8 Mev/nucleon was produced using the coupled cyclotron facility at the NSCL. The primary beam impinged onto a 206 mg/cm^2 Be target where an assortment of nuclei were produced (secondary beam) by fragmentation reactions. The A1900 fragment separator [63] was used to separate and isolate the nuclei of interest.

Degraded primary beam is the most abundant isotope after the target. Because of charge exchange reactions between the projectile and the target, the ^{136}Xe beam could become fully stripped of electrons or pick up electrons from the target while going through the target. The charge exchange reaction between target and projectile is a stochastic process. Once an average depth inside the target has been reached, the charge state distribution of the ions does not depend on the initial charge state but the

initial projectile's energy, and target and projectile atomic numbers. In the current experiment, fully stripped $^{136}Xe^{54+}$ to lithium-like $^{136}Xe^{51+}$ degraded primary beam charge states were more abundant than all the nuclei of interest combined by at least two orders of magnitude. The intensity of other degraded primary beam charge states is less or comparable to secondary beam fragment intensities. To avoid transmitting degraded primary beam charge states to the implantation and decay endstation, the momentum acceptance was set to $\pm 0.5\%$ at the dispersive plane of the fragment separator. The magnetic rigidity $B\rho$ in the first part of the A1900 was set to 3.96 Tm. This value of magnetic rigidity corresponds to a setting between the degraded primary beam fragments $^{136}Xe^{51+}$ and $^{136}Xe^{50+}$.The second part of the A1900 had a magnetic rigidity of $B\rho = 3.8515$ during the production setting so that ^{120}Rh ions were centered.

3.1.2 Detector Setup

At the dispersive plane of the A1900, the beam hit an equivalent effective thickness of 56 mg/cm^2 Al material which was used as a degrader. The equivalent Al material corresponds to a PPAC detector, which was not used during the experiment, and a plastic scintillator which was used to obtain a position measurement in the horizontal plane of each isotope. Among ions of the same species there is a linear correlation (to 1^{st} order) between their momentum and their horizontal position at the dispersive plane. This position information was used to correct the spread in detected energy loss and time-of-flight (TOF) measurements of the same species further downstream that is induced by the $\pm 0.5\%$ momentum spread of the fragments. The same scintillator was also used to obtain one of the signals of a TOF measurement for each isotope. The second signal of the TOF measurement was obtained from a second plastic scintillator in the experimental vault. The approximate distance between the signals of the TOF measurement was 38 m.

In the experimental N3 vault, the radioactive beam was implanted into the β-

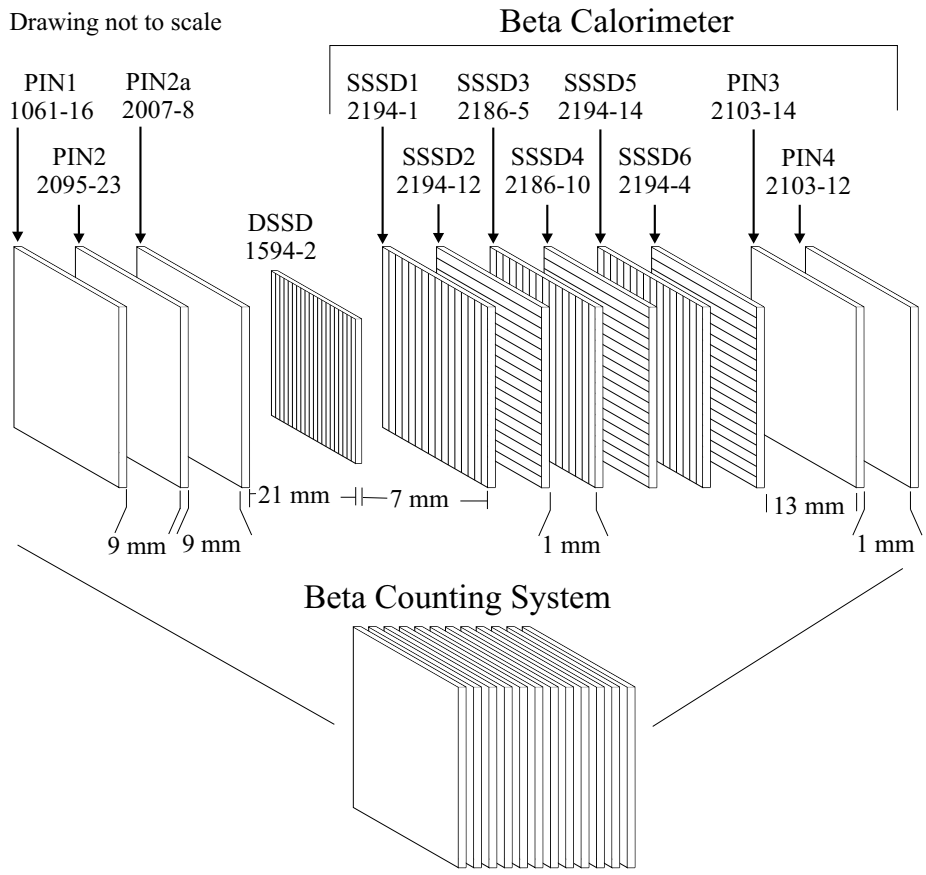

Figure 3.2: Schematic of the β-decay endstation. Silicon detector serial numbers are given below the name of the detector. Distances between detectors are also given. Courtesy of S. Liddick.

decay endstation where the subsequent β-decay was studied. The NSCL β-decay endstation [64] was surrounded by the Neutron Emission Ratio Observer (NERO) [65] to study the β-decay properties of the selected nuclei.

A schematic diagram of the β-decay endstation is shown in Figure 3.2. The β-decay endstation consists of a stack of three Si detectors (PIN1, PIN2 and PIN2a) followed by a double-sided Si strip detector (DSSD) and a stack of single-sided Si strip detectors (SSSD). The first three PIN detectors had thicknesses of 488, 992 and 966 μm respectively and their electronics was set up to detect beam energy losses up to 10 GeV. The PIN thicknesses were selected so that nuclei of interest would slow down in the PINs and be stopped inside the DSSD.

A cooling system surrounding the PINs and DSSD detectors was used trying

to improve their energy resolution. Inside the β-decay endstation the cooling system consisted of a copper pipe in contact with copper frames located near each detector at $\approx$5 mm. A mixture of ethylene glycol and water was used as coolant at a temperature of 0^o C. The energy resolution of each detector was measured at room temperature and during cooling. Leakage currents were reduced but no appreciable gain in the resolution was observed

The DSSD consists of 40 1-mm strips in the front (y-direction) and 40 1-mm strips in the back (x-direction) resulting in 1600 individual pixels in the xy-plane. Each strip was connected to a dual gain amplifier to detect the energies of the secondary beam fragments being implanted (0-3 GeV, low gain) and the energies that the β particles deposit (0-400 keV, high gain) when the implanted isotopes β-decay. To take advantage of the number of pixels the beam was defocused to illuminate as much area of the detector as possible. For each isotope reaching the DSSD, the specific pixel location of the implantation, a time stamp of when the event took place, and front and back energies were recorded.

The first SSSD detector had a thickness of 990 μm and it was used as an additional mechanism to detect β particles and to identify isotopes that do not stop inside the DSSD. The SSSD detectors used were segmented into sixteen strips and they were mounted so that the strip orientation alternated between the x and y directions.

The β-decay endstation was surrounded by the Neutron Emission Ratio Observer (NERO) [65] to detect β-delayed neutron emission as shown in Fig. 3.3.

NERO consists of 60 proportional counters containing ^{3}He or BF_3 placed in concentric rings embedded in a polyethylene matrix surrounding the implantation chamber. Once a decay event had been observed in the β-decay endstation, a hardware gate was opened for 200μs to allow NERO to detect neutrons. The gate time was chosen to allow time for the neutrons to become thermalized inside the NERO moderator matrix to maximize detection efficiency. Each proportional counter was individually read out and time and energy were recorded. Since the energy of the neutrons is not

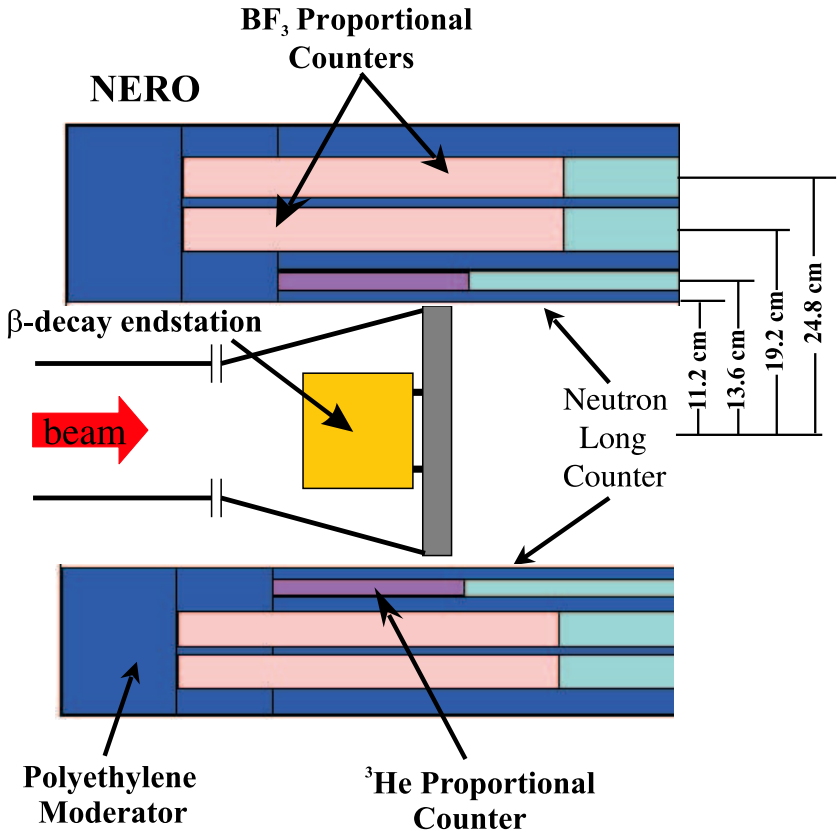

Figure 3.3: Schematic diagram of the β-decay endstation surrounded by the Neutron Emission Ratio Observer NERO. Distances between concentric rings are also given. Drawing not to scale.

directly measured because of the moderation, the measured energy is simply the Q value of the reaction inside the proportional material plus the typically small residual energies of the neutrons.

3.1.3 Electronics

A schematic diagram of the signal processing system is shown in Fig. 3.4. The event trigger was either a PIN1 signal (particle arriving with the beam) or a master gate DSSD signal (β-decay). The master gate live signal resulted from an AND between a master gate and a not-busy signal from the computer. The live signal triggered the computer acquisition to read the detectors and created gates for the VME ADCs and coincidence registers.

The 80 signals from the DSSD (40 back and 40 front strips) were grouped in blocks 1-16, 17-32 and 33-40 for both back and front strips. Because it is necessary to distinguish between implantation of particles, which roughly deposit $\approx$2 GeV, and emission of β-decays, which leave energies around $\approx$150 keV, those blocks of signals were sent into Multi Channel System (MCS) pre-amplifiers. These pre-amplifiers provide low- and high- gain outputs. The low-gain output signals were used to detect ion implantations and they were sent into VME ADCs. The high-gain signals were used to detect β-decays and they were sent into a Pico Systems shaper -discriminator. After shaping, the high-gain signals were then sent into VME ADCs. An OR signal of the timing signals of each Pico systems module went into a coincidence register bit. In software, this bit in the coincidence register was used to decide if there was information in the corresponding VME ADC that had to be read-out. In that way, the DSSD information was read in blocks of 16 low and high channels even if there was only one strip within that block registering an event, but only the VME ADCs that had experimental data were read-out. The DSSD master gate signal consisted of an OR signal between all the 6 ORs of all the Pico system modules. The individual timing signals of each module were also sent into a scaler module.

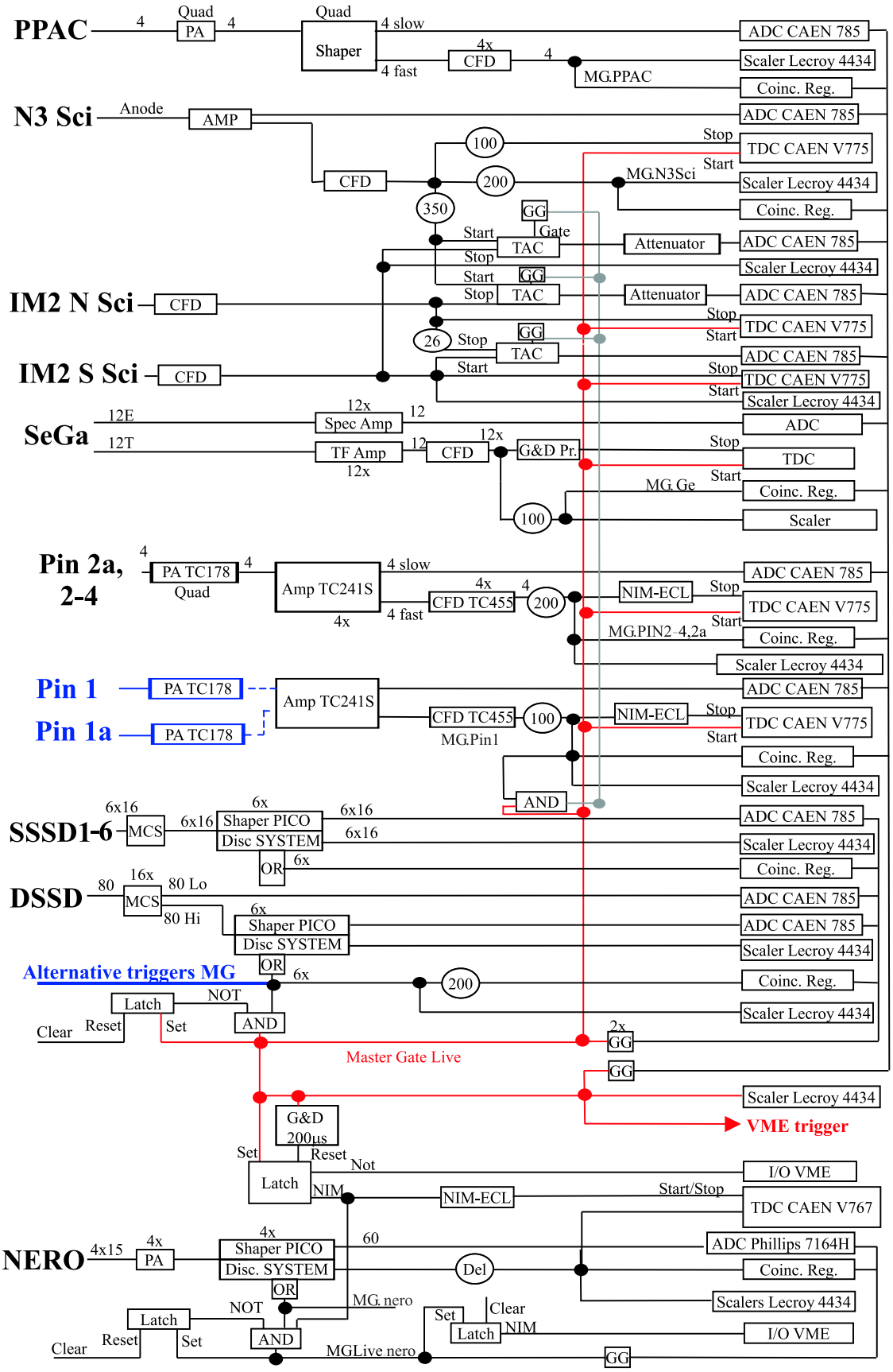

Figure 3.4: Electronics setup during experiment 02032. Numbers within circles correspond to delays in nanoseconds.

Signals of the PIN detectors were sent into pre-amplifiers and then to amplifiers that provided fast and slow signals. The slow or energy signals were then sent into a VME ADC while the fast or timing signal (PIN master gate) were sent into a coincidence register and a scaler module. The electronics of the 12 Ge detectors in SEGA were similar to the PIN's. While the particle identification was being confirmed with γ-rays from microsecond isomers, the trigger was switched to an OR of the timing signals out of the SEGA amplifiers.

Three scintillator signals were used to obtain the TOF of incoming particles. A scintillator in the experimental vault was used as the TOF start signal and two delayed signals from photomultipliers at both ends of the scintillator in the dispersive plane of A1900 ($IM2N$ and $IM2S$) were used as the TOF stop signals in two TAC modules. The TAC's gate was triggered by an AND between PIN1 master gate and the master gate live signal to only receive data when an incoming particle arrived to PIN1.

NERO has 60 proportional counter signals that were grouped into A, B, C and D quadrants. Each quadrant has 15 signals that went into a Pico System shaper -discriminator. Following shaping, signals were sent into a Phillips ADC. The fast signals from the discriminator were sent into coincidence registers, scalers and VME multi-hit TDC modules. In software, only ADC channels with signals in the coincidence register were read. The timing signals were OR'ed together to obtain a NERO master gate signal. The NERO master gate live was the result of an AND between the NERO master gate, a computer not-busy signal and a latch signal that was ON for 200 μs after the master gate live signal was created. The NERO live signal created gates for the NERO ADCs and coincidence registers. Times of all neutron events in all NERO channels that occur within 200 μs after a decay trigger were recorded. The ADCs used for the energies were single-hit and therefore in each channel, only the first of the energy signals of neutron events within the 200 μs window were recorded. NERO readout came last in software and a bit set by the end of the 200 μs latch gate was used to make sure the time for NERO to detect neutrons was over.

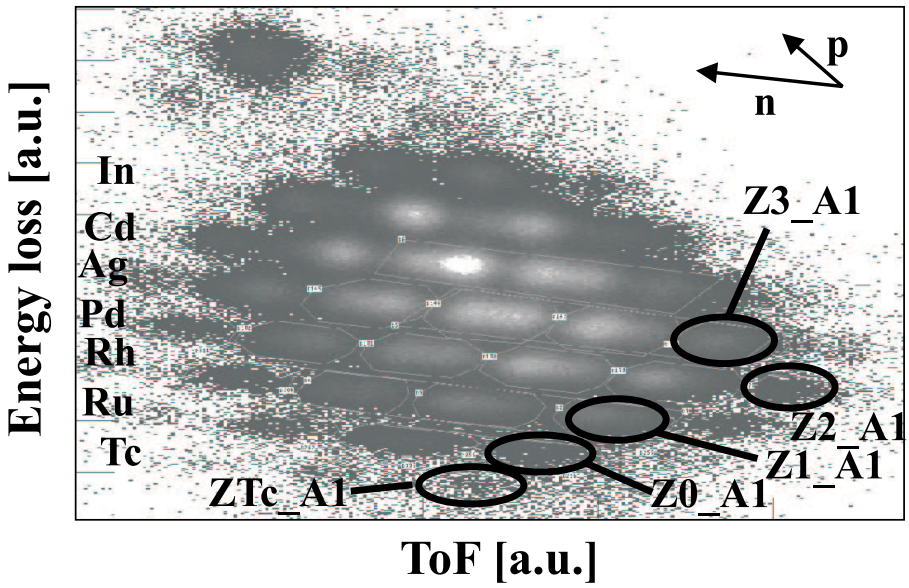

Figure 3.5: Particle identification using energy loss in the first PIN detector versus time-of-flight of all nuclei reaching PIN1. Examples of gates used in the identification are shown.

3.2 Particle Identification

Particle identification was first obtained at the extended focal plane of the A1900 through a combination of the information of the energy losses in a stack of Si detectors and a TOF measurement. A plastic scintillator at the extended focal place of the A1900 provided the start signal while a delayed signal from the scintillator at the dispersive plane was the stop of the TOF measurement. A Ge detector was used to obtain γ-rays of known microsecond isomers to verify the identification.

In the experimental vault, the particle identification was obtained using a similar procedure with the energy losses of the PIN and DSSD detectors and the start signal of the time-of-flight from the scintillator in the experimental vault. As a first step, each nucleus was identified by the momentum-corrected energy loss in PIN1 and the momentum-corrected TOF measurement as shown in Fig. 3.5. Due to the presence of secondary-beam charge states, additional information is needed because fully stripped isotopes with mass number A have a similar PIN1 energy and TOF as hydrogen-like isotopes with mass number A-3. To identify the charge states, the total kinetic energy

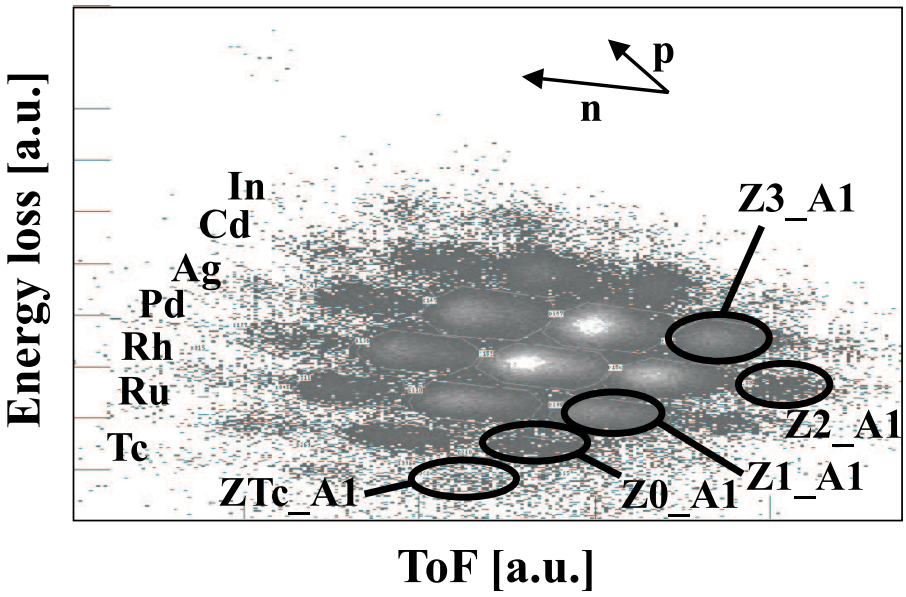

Figure 3.6: Energy loss in the first PIN detector versus time-of-flight of only implanted nuclei in the DSSD. Examples of gates used in the identification are shown.

of each isotope was obtained by summing up the calibrated energies of the first three PINs and the DSSD. The particle identification of nuclei reaching the DSSD is shown in Fig. 3.6. Within the selected fragments, the majority of the In, Cd isotopes and unfortunately the very exotic Rh, Pd and Ag isotopes were stopped before they reached the DSSD and no final identification was obtained.

The energy calibration of the first three PIN detectors and the DSSD was done using degraded primary beam at different energies (13140, 14505, 14717 and 14762 MeV). The program LISE [66] was used to theoretically calculate the energy loss of the Xe particles passing through the Si material in the PIN and DSSD detectors. The LISE program has the option of using ATIMA [67] or Ziegler *et al.* [68] methods to calculate the stopping and range of ions into matter. As mentioned before, in the current experiment In, Cd isotopes and very exotic Rh, Pd and Ag isotopes are stopped before they reach the DSSD. Because ATIMA mistakenly predicted that all of those isotopes would reach the DSSD while Ziegler *et al.* was more accurate in their predictions, it was decided to use the theoretical energy losses calculated by Ziegler *et al.* The reason of the disagreement however, is not well understood. Figure 3.7 shows

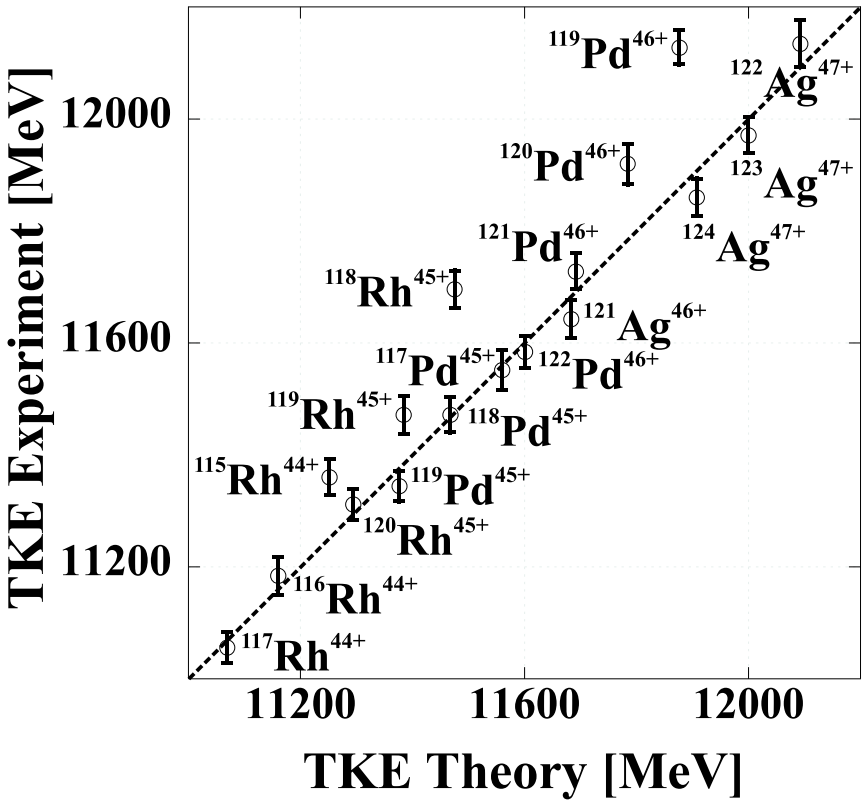

Figure 3.7: Calibrated versus theoretical total kinetic energy for isotopes of interest.

the resulting calibrated versus theoretical total kinetic energy for isotopes of interest.

The total kinetic energies (TKE) versus time-of-flights (TOF) for Tc, Ru, Rh, Pd and Ag isotopes are shown in Fig. 3.8. The hydrogen-like charge states with mass number A-3 can be distinguished from the fully stripped isotopes with mass number A due to the difference in TKE and to some extent TOF.

To better understand the contamination of charge states in the particle identification, it was decided to obtain a total kinetic energy histogram after the energy has been corrected by the TOF measurement. This is equivalent to a rotation in Fig. 3.8 so the "distance" between charge state and fully stripped state is maximized. Figures

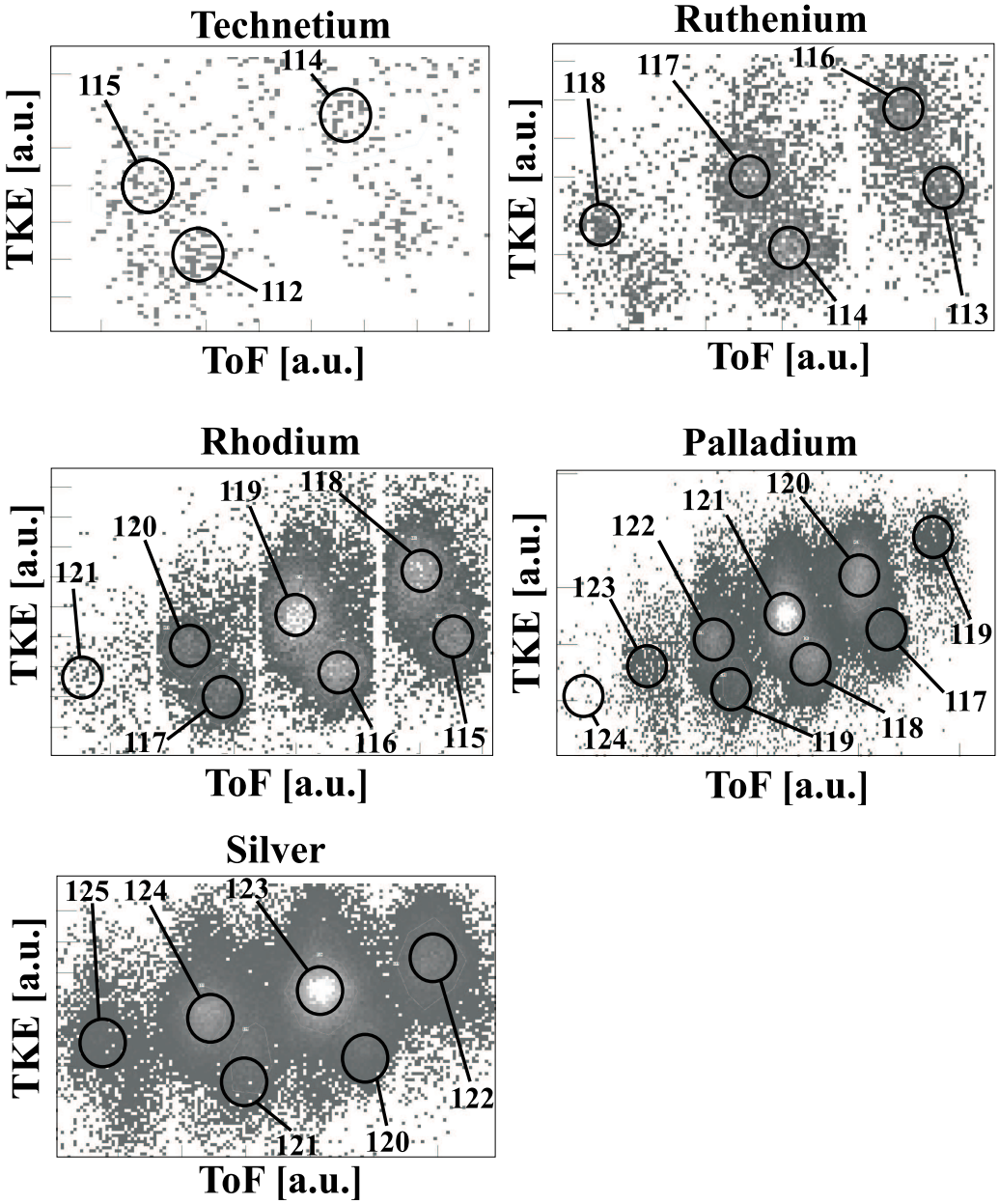

Figure 3.8: Total kinetic energy versus time-of-flight for isotopes of interest. The mass number and approximate location of each isotope is shown.

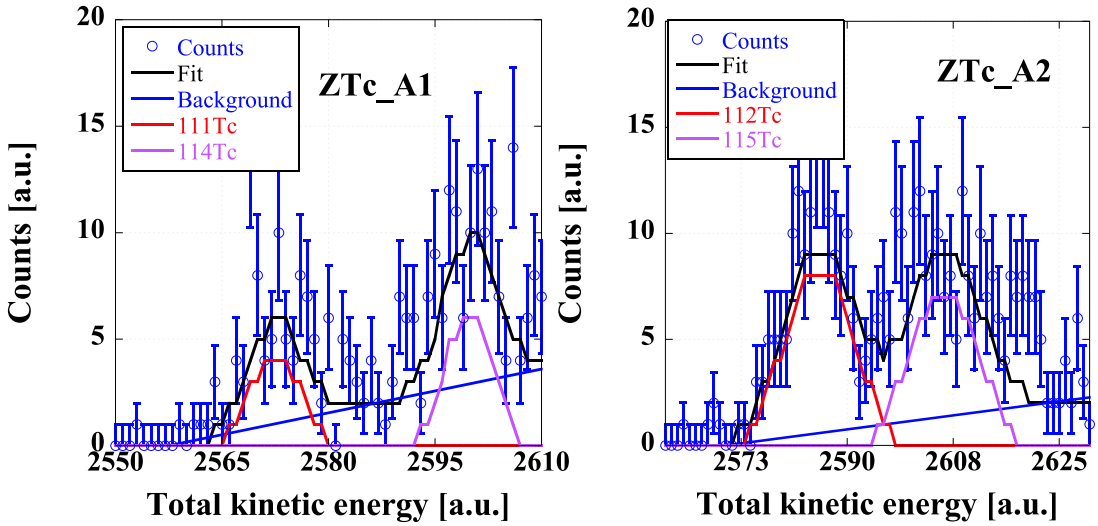

Figure 3.9: Histograms of the total kinetic energy for Tc isotopes. The name of the gate applied in Fig. 3.6 is shown and each graph includes only the fragments within that gate. Gaussian fits and a constant background are also shown.

3.9, 3.10, 3.11, 3.12 and 3.13 correspond to histograms of the rotated total kinetic energy for Tc, Ru, Rh, Pd and Ag fragments respectively. Each fragment must be within a gate defined in Fig. 3.6 to be included in the histogram.

Particle misidentification is gate-dependent and different gates in the TKE vs TOF graphs and TKE histograms were used to study the background contamination. In cases where the contamination was higher than average a contamination-induced error was included in the results. Particle misidentification due to the resolution and spread of the energy of the isotopes was calculated to be on average less than 3%.

The particle identification was confirmed at the beginning of the experiment by detecting γ-rays from the decay of known microsecond isomers in ^{130}Sn and ^{126,127}In at a temporary and separate implantation station upstream. In addition, γ-rays from the decay of a well known 164 ns isomer of ^{134}Te, which is the most abundant fragment being implanted, were also observed. For these measurements, the NSCL Segmented Germanium Array (SEGA) [69] with 11 Ge detectors was used to detect γ-rays in

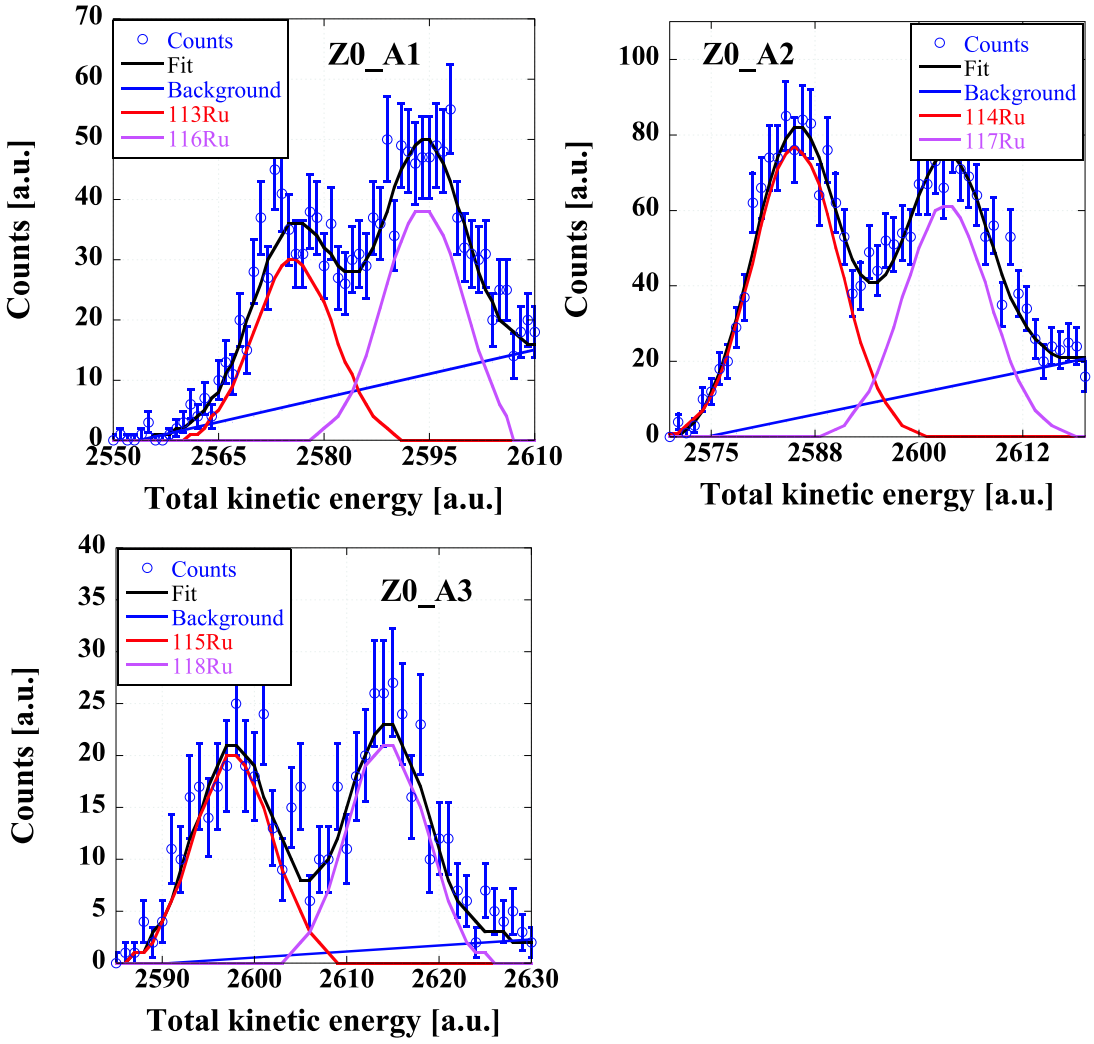

Figure 3.10: Histograms of the total kinetic energy for Ru isotopes. The name of the gate applied in Fig. 3.6 is shown and each graph includes only the fragments within that gate. Gaussian fits and a constant background are also shown.

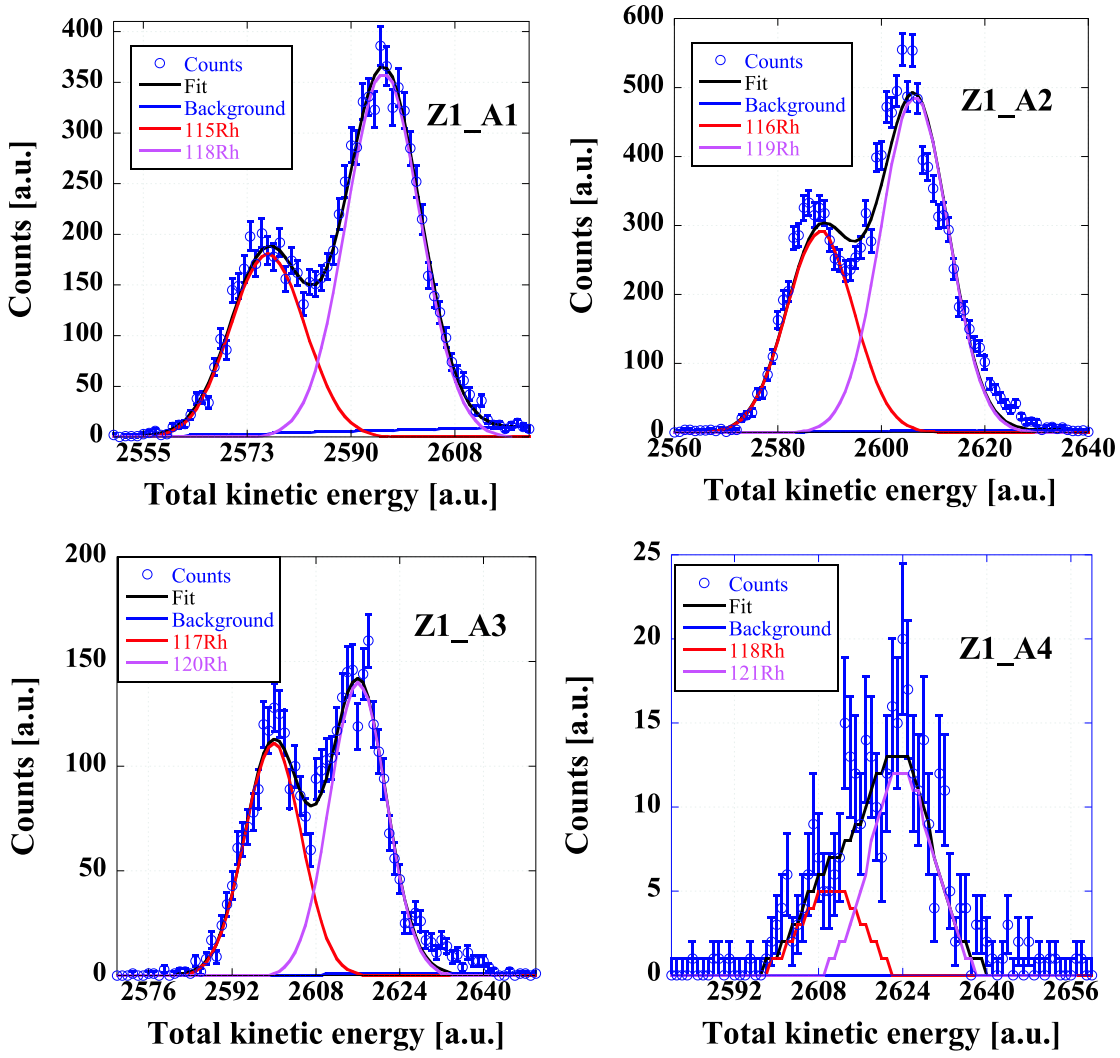

Figure 3.11: Histograms of the total kinetic energy for Rh isotopes. The name of the gate applied in Fig. 3.6 is shown and each graph includes only the fragments within that gate. Gaussian fits and a constant background are also shown.

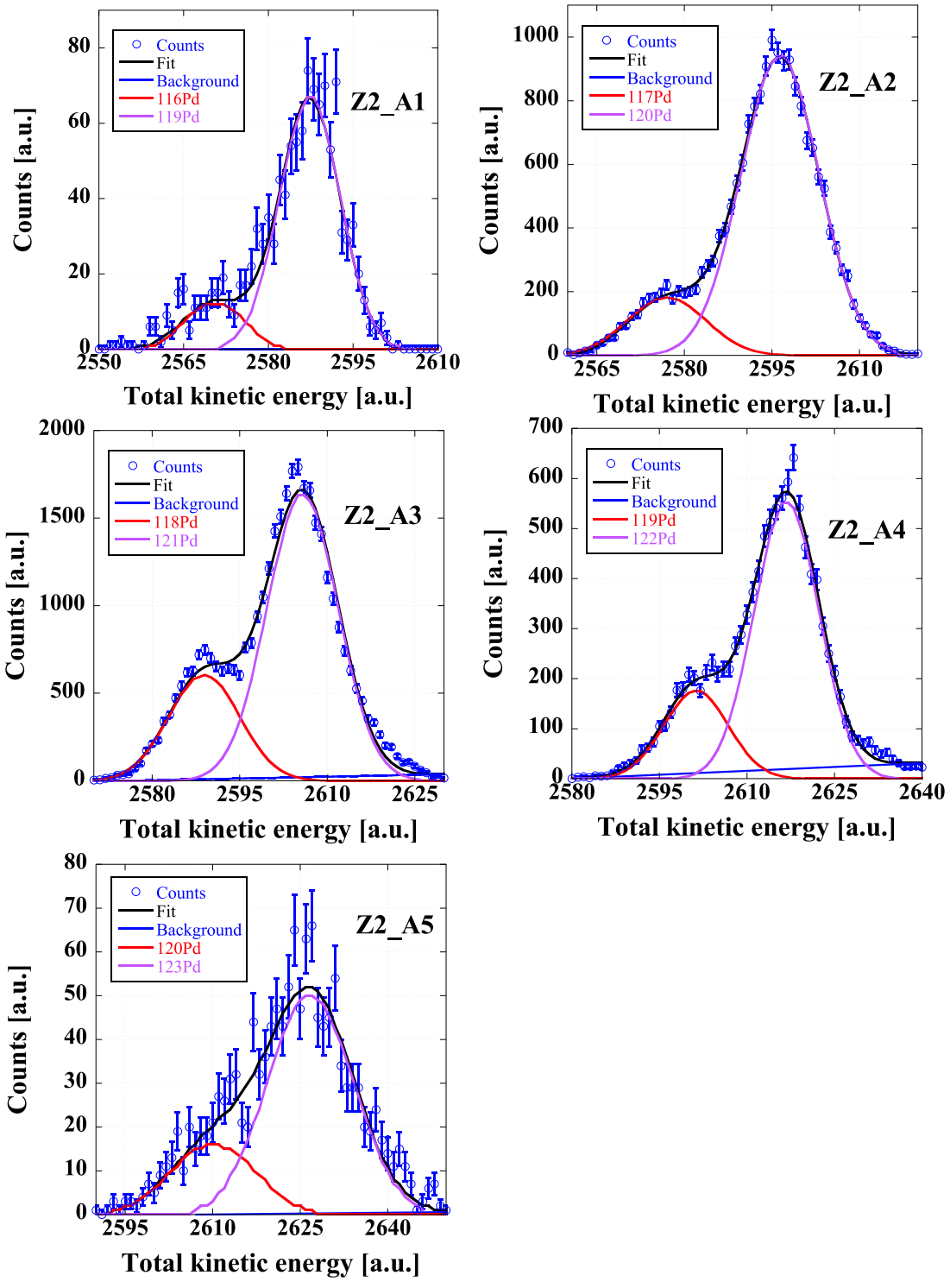

Figure 3.12: Histograms of the total kinetic energy for Pd isotopes. The name of the gate applied in Fig. 3.6 is shown and each graph includes only the fragments within that gate. Gaussian fits and a constant background are also shown.

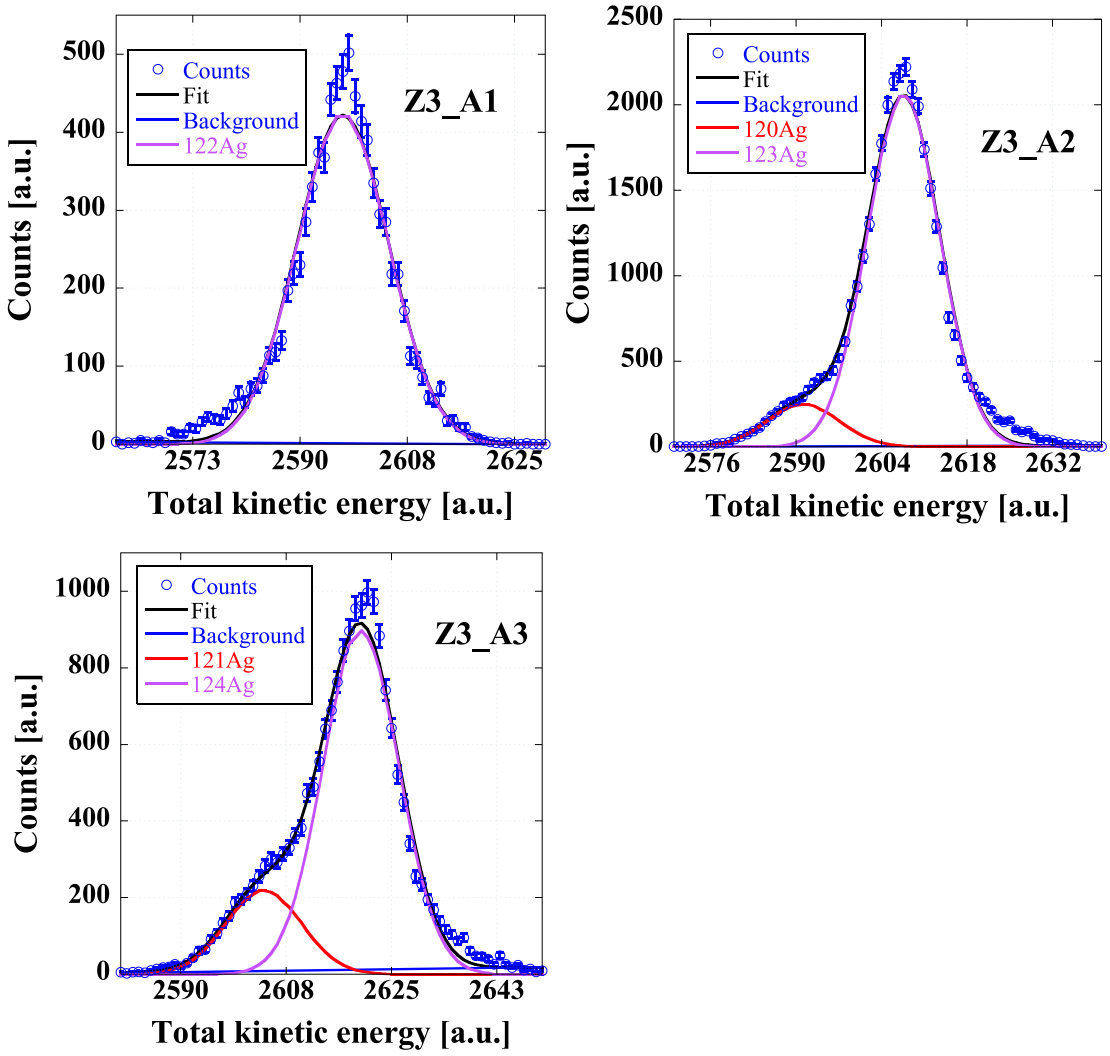

Figure 3.13: Histograms of the total kinetic energy for Ag isotopes. The name of the gate applied in Fig. 3.6 is shown and each graph includes only the fragments within that gate. Gaussian fits and a constant background are also shown.

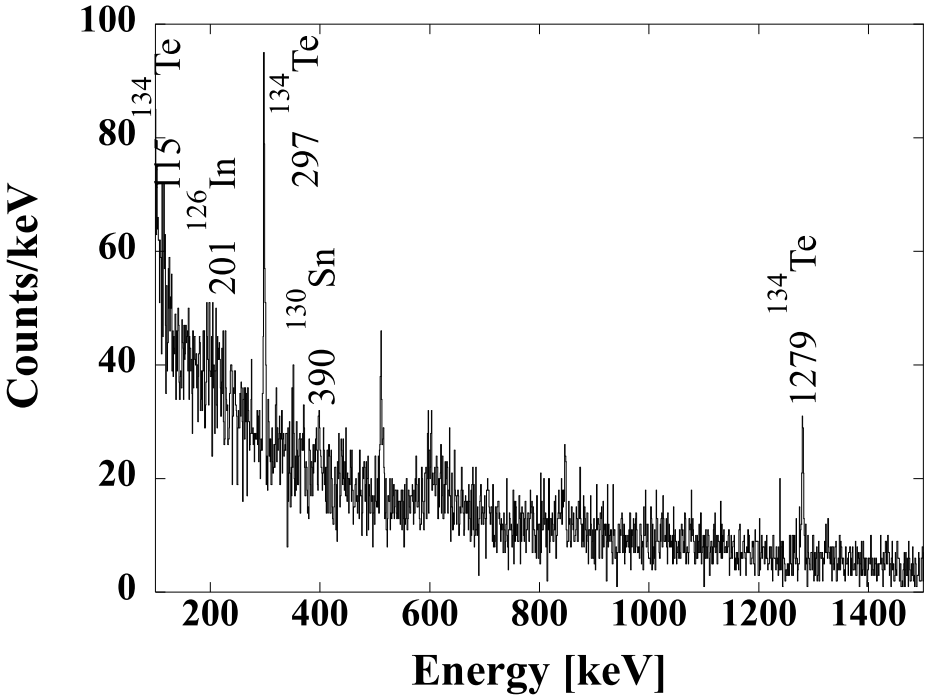

Figure 3.14: Isomeric γ-ray spectrum collected within 20 μs following the arrival of a particle. Known γ-lines used in the identification are shown.

coincidence with beam particles. Observed γ-rays collected during $\sim$9 hours are shown Fig. 3.14.

3.2.1 Implants and β Decay

Once the isotope had been identified, it was considered to be implanted into the DSSD if the event had a valid signal in PIN1, a signal in the low gain channel in at least one front strip in the DSSD, a signal in the low gain channel in at least one back strip in the DSSD and the absence of a valid signal in the first SSSD (the isotope went through the first three PIN detectors and it stopped in the DSSD). On the other hand, an event was defined as as a decay if the event did not have valid signals in PIN1, PIN2 and PIN2a and valid signals in the high gain channel in at least one front

strip in the DSSD and in the high gain channel in at least one back strip in the DSSD (it was not a particle coming with the beam and the β particle was detected in the DSSD). Because some light energy events may be light particles that deposit small energies in the first three PINs, software thresholds were set appropriately to identify and discard them.

Correlations between implants and decays were obtained in software on an event-by-event basis using time and pixel locations. To be correlated, a decay had to take place within a given correlation time of an implantation in the same pixel or the 8 pixels adjacent to it. Up to three decays within the correlation time window were considered in the analysis (parent, daughter and granddaughter decay). The correlation time window was chosen isotope-dependent so decays of a fourth generation were minimal. It was typically 10 s and for the very exotic Pd and Rh isotopes was reduced to 1-3 s. If there were two or more implants correlated to the decay, the decay was discarded. The total implantation rate in the DSSD was 0.4 Hz. Because the average implantation rate per 9-pixels was only 0.002 Hz, the number of multiple implantation events correlated to a decay event were negligible.

3.3 Fitting and Maximum likelihood methods

Differences between the time stamps of implants and correlated decays were used to obtain the β-decay half-lives of implanted nuclei. One method to obtain them is based on a histogram of such differences which is then fit with a Bateman [70] equation that takes into account the decay of the parent, daughter and granddaughter nuclei. The fitting procedure involves a least-squares minimization which finds a constant background level and the decay constant for the parent decay. Although this method has been widely used in the past and its highly effective in cases with a large number of statistics, the binning procedure that is used to obtain the histogram leads to some loss of decay information. Also, the fitting procedure requires enough statistics to satisfy

the requirements of Gaussian statistics of the individual histogram bins. Because some of the isotopes of interest had a small amount of statistics, it was decided to use a maximum-likelihood (MLH) calculation where all the available information is used. This method has been used in the past in experiments with low statistics [71, 72].

The maximum-likelihood method finds the parent decay half-life which maximizes a joint probability density called the likelihood function. The likelihood function is calculated considering the probabilities of all the possible scenarios that may result in the observed sequence of decays, including parent, daughter and granddaughter decays as well as background. The β-delayed neutron emission probabilities effectively change the event chain that a given nucleus may follow in its decay and they were included in the analysis. For each decay chain, a probability as a function of parent decay half-life can be calculated if the daughter and granddaughter half-lives, background rate and β-detection efficiency ϵ_β are known. They have to be calculated independently because taking into account a second free parameter (β background for example) leads to a large number of maxima in the likelihood function for the typical experimental data in this work. This high number of maxima was found using Monte Carlo simulations that created "decay data" with expected experimental values of parent, daughter and granddaughter $T_{1/2}$, ϵ_β and β background. Even though three decay generations were included, the only free parameter (after other "free" parameters were found using alternate methods) in our maximum likelihood analysis is the parent decay half-life.

3.3.1 β detection efficiency

In the cases of $^{116-120}$Rh, $^{121-122}$Pd and $^{121-124}$Ag, there was sufficient statistics to also fit histograms as shown in Fig. 3.15, Fig. 3.16 and Fig. 3.17, respectively. Those cases were used to find the β-decay efficiency (ϵ_β) of the NSCL β-decay endstation by comparing the total number of fitted parent decays N_1 with the total number of

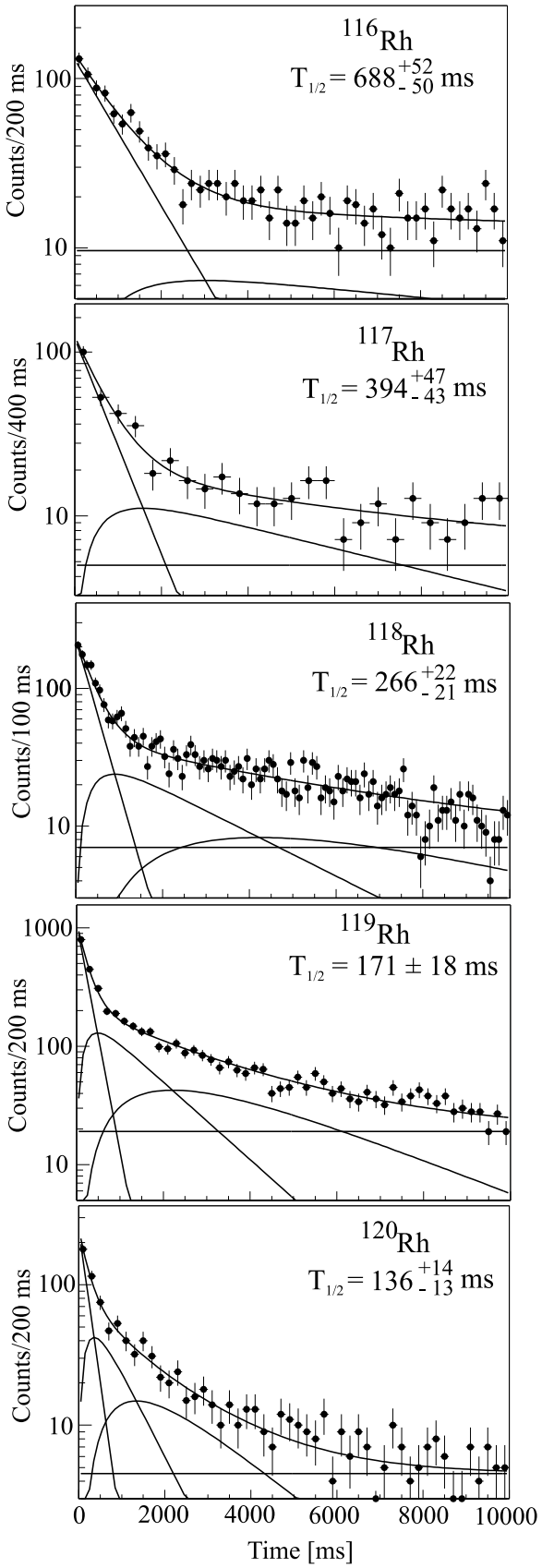

Figure 3.15: Decay curves of rhodium isotopes. Contributions from the parent, daughter, granddaughter and background are shown.

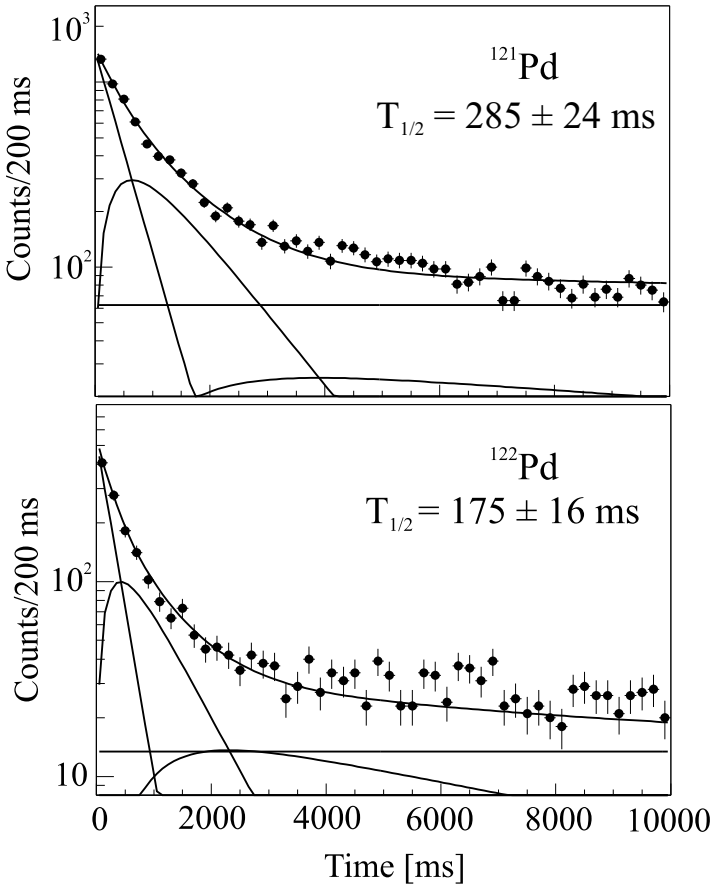

Figure 3.16: Decay curves of palladium isotopes. Contributions from the parent, daughter, granddaughter and background are shown.

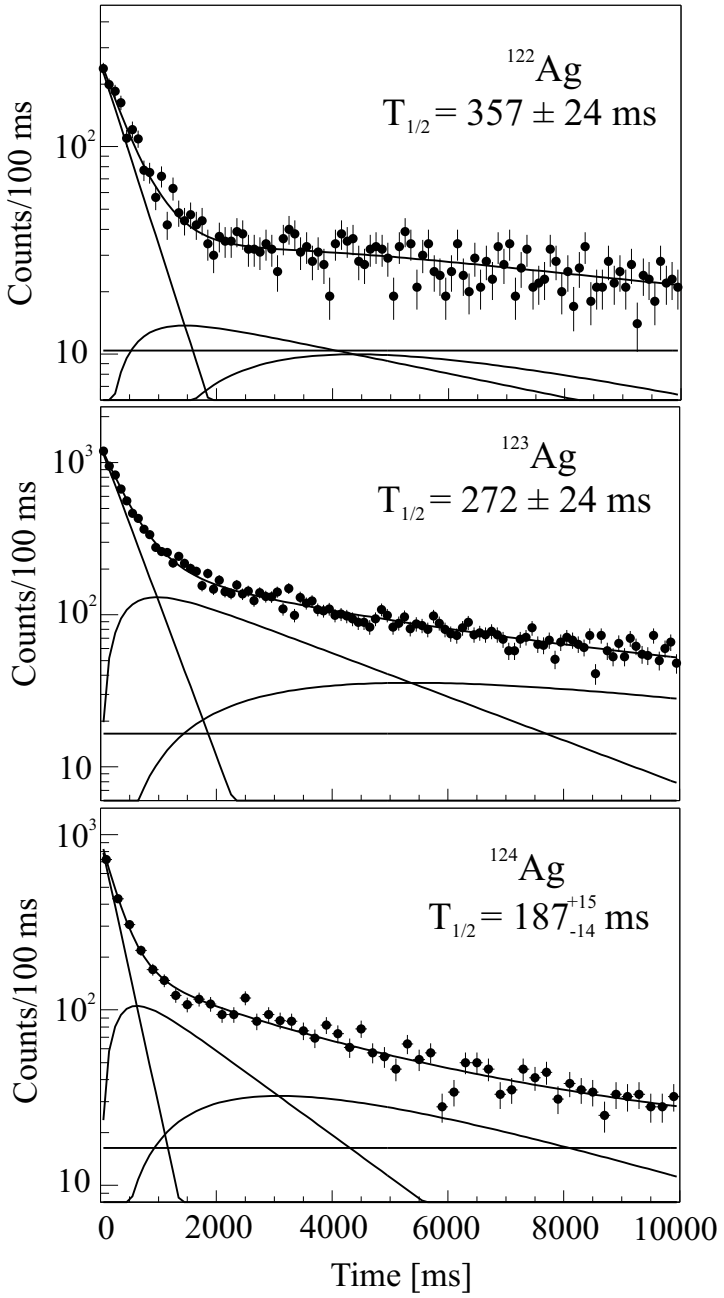

Figure 3.17: Decay curves of silver isotopes. Contributions from the parent, daughter, granddaughter and background are shown.

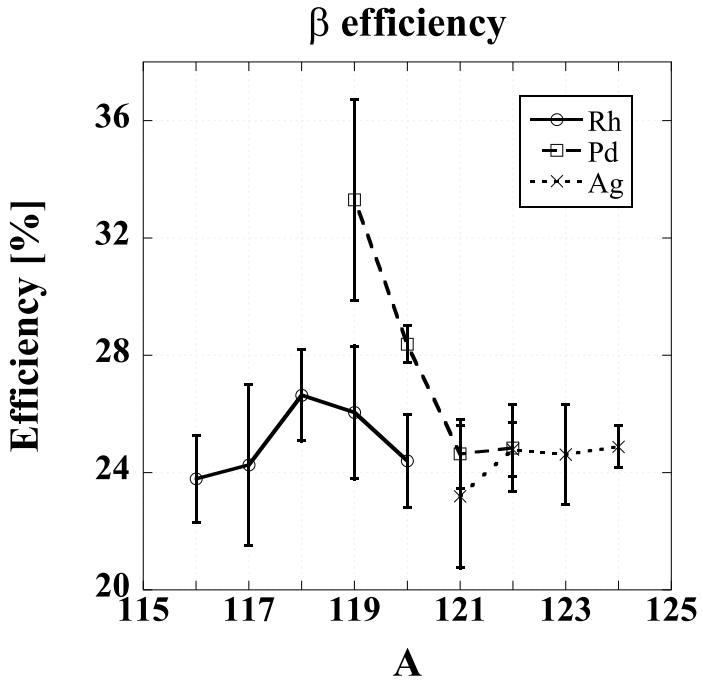

Figure 3.18: β efficiency of the β-decay endstation as a function of mass number for Rh, Pd and Ag isotopes.

implanted isotopes N into the DSSD using the equation,

$$\epsilon_\beta = \frac{N_1}{N} = \frac{A_0 T_{1/2}}{\Delta t N ln2}, \tag{3.1}$$

where A_0 is the number of counts in the first bin, $T_{1/2}$ is the fitted parent half-life and Δt is the bin size. The efficiencies range from 23% to 27% for different isotopes with no systematic trends as shown in Fig. 3.18. The average β-decay efficiency was taken to be $\epsilon = 25\% \pm 2\%$.

3.3.2 β Background

Due to the nature of the experimental setup, decays of long-lived late generations outside the correlation time may be correlated to a more recent uncorrelated implant

occurred within the same or adjacent pixels. They correspond to decays assigned to the wrong implant and those cases constitute β background. Other potential background sources are light fragments that pass through the Si detectors and mimic the energy loss of electrons and are not entirely rejected by software gates. Because of the low implantation rate, the background is constant over the correlation time after an implantation. The background rate was determined by counting decay events that occurred outside a 10 s correlation window after an implantation. If there was an implantation, the pixel where it happened along with the 24 adjacent pixels were "blocked" for 10 seconds. If a β-decay type event occurs, it is counted as background in the nine adjacent pixels if they are not "blocked". The background rate for an implantation pixel is then the number of counted background decays divided by the total "unblocked" time at this location. The time the pixels were blocked was varied from 10 to 100 s and no noticeable changes were observed.

Because fragments in the beam do not hit uniformly over the face of the DSSD, there are more fragments being implanted at the center of the DSSD than close to the edges. This results in a β background that is pixel-dependent as shown in Fig. 3.19.

Because the implantation profile in the DSSD may change for different isotopes, the decay background (which is calculated pixel by pixel) may change. For each isotope, a background was calculated by taking the average of the pixel-dependent background of all the pixels where an implantation of the specific isotope occurred. This way of calculating background is represented by black triangles in Fig. 3.20.

As mentioned before, the fitting procedure also finds a background level. The β background found in this way for cases with high statistics is represented in Fig. 3.20 with black squares. A third method of finding the β background (black diamonds in Fig. 3.20) uses the maximum likelihood method itself and it can be used as a consistency check when compared to the results of the other methods. The method outlined in Ref. [73] was followed, where the total number of implantation events N is the sum of those implantations that were followed by up to three observed decays N_{123}

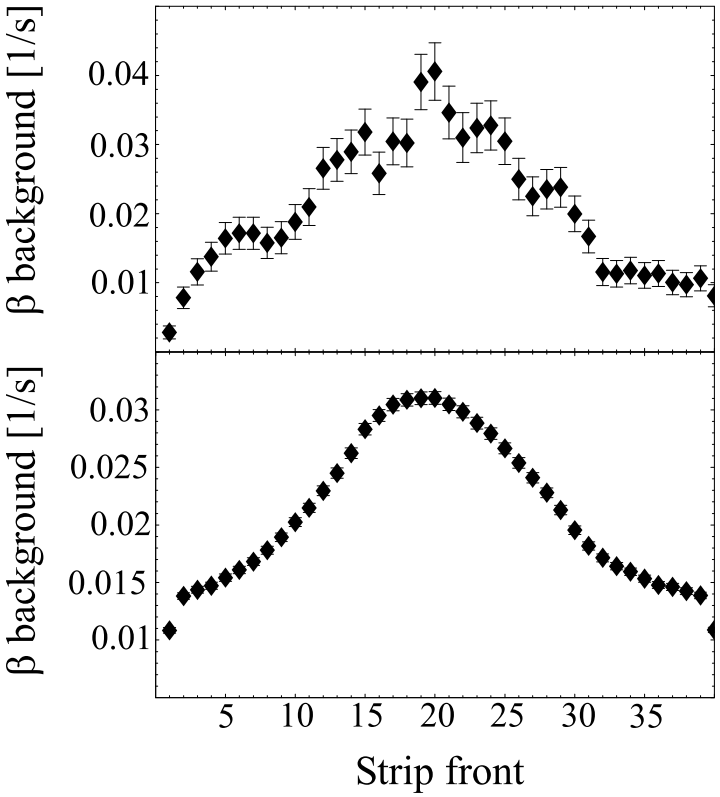

Figure 3.19: a.) β-background of the 40 pixels in the strip channel 15 of the back of the DSSD during *one* typical data run. b.) β-background of the 40 pixels in the strip channel 15 of the back of the DSSD averaged over all the data runs.

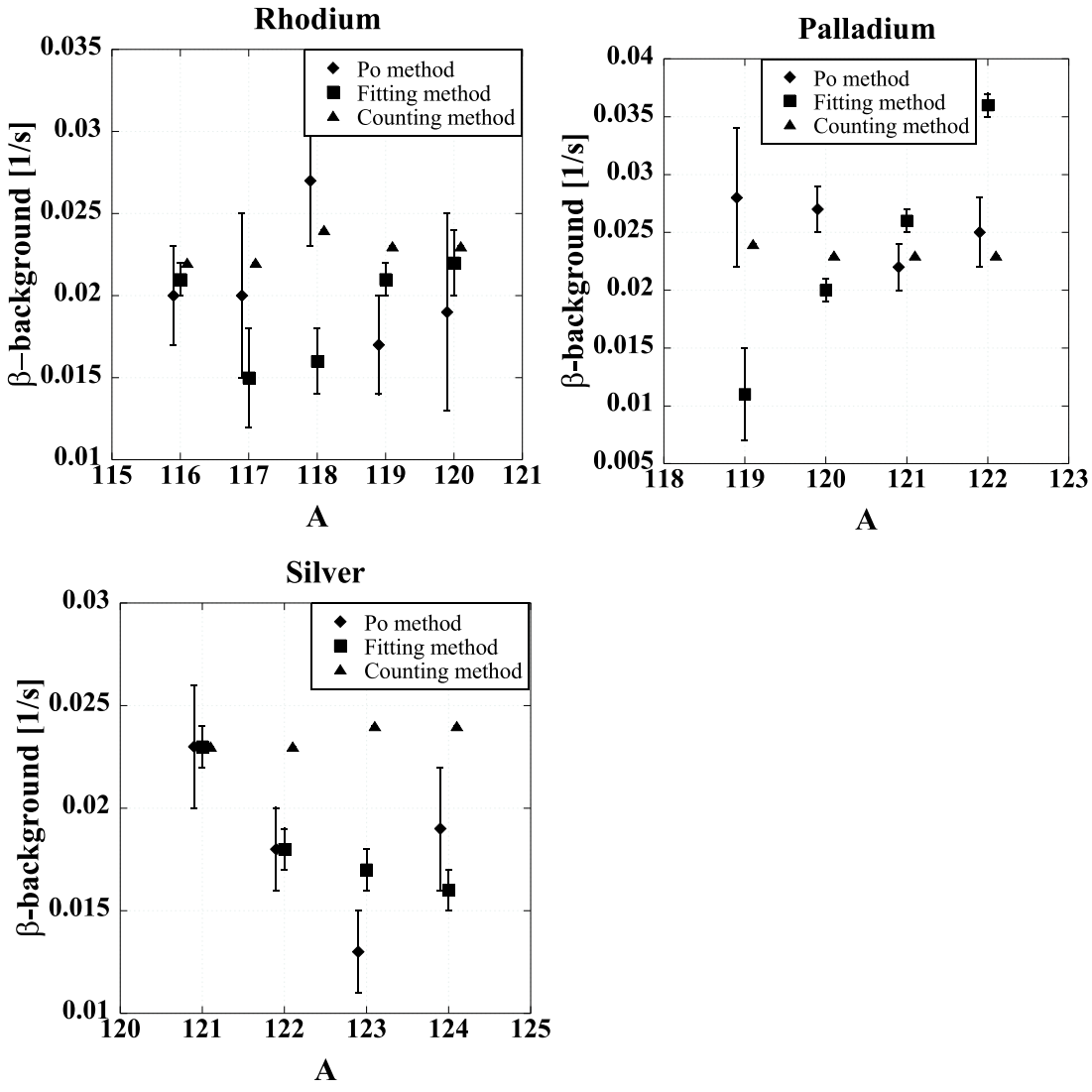

Figure 3.20: Average β background per second for a given isotope. Results from three different methods are shown. For an explanation of the methods read text.

plus the number of implantations that did not have any observed decay event within the correlation time N_0, $N = N_0 + N_{123}$. If P_0 is the probability of the observation of no decay event within the correlation time, N_0 and N_{123} can be expressed as,

$$\begin{aligned} N_0(b) &= NP_0(b) \\ N_{123} &= N(1 - P_0(b)) \qquad \text{and therefore,} \\ N_0(b) &= \frac{P_0(b)N_{123}}{1 - P_0(b)}. \end{aligned} \tag{3.2}$$

P_0 is a function of different parameters, one of them being the β background b. N_0 calculated using Eq. 3.2 thus depends on the background which is then chosen such that the experimental and calculated N_0 were equal, $N_0^{Exp} = N_0(b)$.

The fitting method and N_0 method of finding the β background were found to be consistent, but because they are indirect methods that have the uncertainties of other parameters (daughter and granddaughter $T_{1/2}$, β detection efficiencies) entangled in the result and they are based on less statistics as they require real implantation events, it was decided to use instead the background found by counting decay events occurred outside a 10 s correlation window after an implantation (counting method in Fig. 3.20). The total average background rate of decay-type events was 0.023 ± 0.002 Hz.

3.3.3 Neutron detection and background

An event with a valid energy signal in one or more of the NERO proportional counters was considered a neutron event. Using appropriate energy gates in software, neutrons can be distinguished from electronic "noise" or from low energy gamma rays which may also interact with the detector gas. Background neutrons may originate from cosmic rays or fragmentation reactions of the radioactive beam.

To determine the background of β-n coincidences, a procedure similar to the one used to obtain the β background in the DSSD was used. Instead of counting just

β-decays, the same procedure was followed for β-neutron coincidences. Pixel and run information of all events that include neutrons and β-decays that are considered uncorrelated and background-like were counted. Because of the low total β-decay rate in the DSSD (2.8 Hz), the probability of detecting a neutron correlated to more than one decay within the 200μs time gate is less than 10^{-4}%.

The background is position and time dependant. The neutron background varies randomly as a function of time and because of the low number of background neutron events, it was decided to average all background events as a function of time to obtain a background rate per pixel. A typical pixel-dependent β-n background is shown in Fig. 3.21. As it was shown in Fig. 3.19, the β-background is larger at the center than at the edges of the DSSD. The dip in Fig. 3.21 at the center of the DSSD is due to that increase in β-decay background because neutron background alone does not depend as much on pixel location. Because of the pixel dependency, the β-n background rate ($b_{\beta-n}$) was calculated averaging only the pixels that had a given isotope being implanted. Comparing the average rate for all isotopes with the β background rate, it was found that the probability for detecting a background neutron within 200μs after a β-decay was on average 0.78$\pm$0.11%. The expected number of β-n coincidences per implant was $t_c \times b_{\beta-n}$. The average $b_{\beta-n}$ is 0.18 ± 0.02 mHz and the total number of background neutrons per isotope are shown in Table 3.1.

The total cosmic ray-related neutron event rate is just $\approx$ 5 Hz. Because NERO detects neutrons only for 200μs after PIN1 triggers, the cosmic ray-related background was calculated to contribute only $\sim$15% of the total measured β-n background. Because no long-lived β-delayed neutron emitters are implanted, the largest contributor must have had a different origin. Most likely this additional $\beta - n$ comes from light beam particles that are indistinguishable from β-decays and are accompanied by neutrons.

As mentioned before, neutrons may result from heavy ions fragmenting inside the β-decay endstation before stopping in the DSSD. Those neutrons were not considered

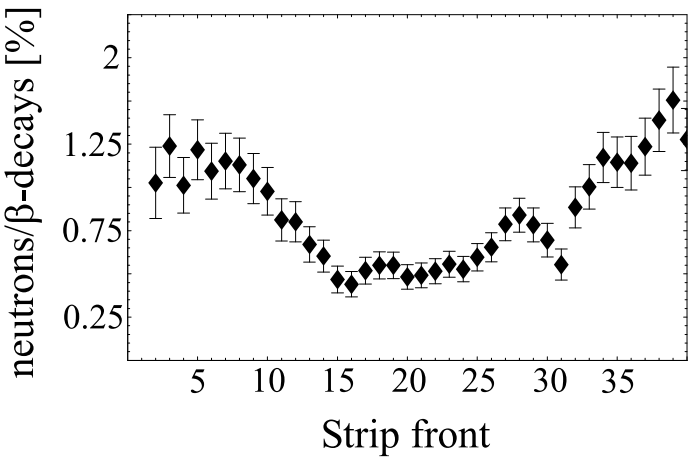

Figure 3.21: β-n background of the 40 pixels in the strip channel 15 of the back of the DSSD averaged over all the data runs.

in the β-n background because they were not triggered by decay events but by PIN1 signals and therefore those events were not included in the neutron analysis. Nevertheless, to determine the likelihood of neutrons produced by fragmentation of beam particles, we took the ratio of the number of PIN1 valid energy signals accompanied with a neutron detection versus only PIN1 valid energy signals. The number of neutrons detected associated with implantation events is approximately 16 times higher than what is expected from only random coincidences with cosmic-ray related neutrons. Less than 3% of the PIN1 triggers have an associated neutron and because of the low beam rate (~1-2 Hz), the contribution to the overall neutron rate is minimal.

3.4 P_n determination

P_n values were calculated using

$$P_n = \frac{N_n - B}{N_\beta \times \epsilon_N}, \tag{3.3}$$

where N_n is the total number of correlated β-n coincidences, B is the calculated number of β-n background coincidences, N_β is the number of parent decays and ϵ_N

is the NERO efficiency. Neutron statistics are shown in Table 3.1. All the isotopes where the P_n values could be measured have sufficient β-decay statistics to determine the number of parent decays N_β from decay curve fits. Because β-delayed neutron emission from daughter and granddaughter decays are expected to be zero they were not considered in the analysis.

As a consistency check, it can be observed in Table 3.1 that for cases with expected P_n=0, the number of measured neutron matches closely the number of expected background neutrons.

In all cases, the minimum number of β-n coincidences that would be necessary to have a one sigma confidence (using gaussian statistics) of having at least one coincidence above the expected number of β-n background coincidences was calculated. If the number of measured β-n coincidences was less than that minimum, the minimum of β-n coincidences was used to calculate the upper limit in the P_n value. In such a way, the resulting upper limit is the interval in which there is a one sigma confidence of not measuring at least one β-n coincidence above background.

The NERO neutron detection efficiency decreases slightly as a function of neutron energy from a value of 37% at 0.1 MeV to 32.4% at 1 MeV. For more energetic neutrons the drop off is more dramatic and for a neutron energy of 5 MeV the efficiency has fallen to 17% [65]. QRPA [47] calculations were performed to obtain the expected neutron energies corresponding to decays from the ground state of the parent nucleus to excited daughter states just above the neutron separation energy S_n in nuclei of interest. The expected neutrons had energies $\sim 0.1 - 1.0$ MeV which are in the range where the NERO efficiency is roughly constant. A NERO efficiency of $\epsilon = 34.7 \pm 2.3\%$ was used.

Table 3.1: Neutron statistics. N_β is the number of parent decays, N_n is the total number of correlated β-n coincidences, and B is the number of β-n background coincidences.

Isotope	Implants	N_β	N_n	B
^{121}Ag	1672	399	3	3.2
^{122}Ag	4859	1229	8	9.7
^{123}Ag	18836	4756	45	31.2
^{124}Ag	4848	1247	14	8.7
^{119}Pd	945	259	3	1.3
^{120}Pd	8802	2577	13	14.7
^{121}Pd	11646	2950	22	21.7
^{122}Pd	2626	669	8	5.3
^{123}Pd	293		1	0.5
^{124}Pd	30		0	0.1
^{116}Rh	2421	591	3	3.9
^{117}Rh	759	189	1	1.2
^{118}Rh	3173	868	14	5.9
^{119}Rh	4700	1256	35	7.9
^{120}Rh	982	245	2	1.6
^{121}Rh	118		1	0.2
^{114}Ru	661		1	1.2
^{115}Ru	129		0	0.2
^{116}Ru	419		0	0.8
^{117}Ru	572		2	1.0
^{118}Ru	144		2	2.7
^{114}Tc	55		1	0.1
^{115}Tc	81		0	0.1

3.5 Error analysis

Experimental daughter and granddaughter half-lives were taken from Ref. [74] except when measured in this work. When a literature value and a result from our experiment was available, a weighted average was used.

The uncertainties in our results include statistical and systematic errors. The half-lives' statistical error is directly obtained from the maximum likelihood analysis, where we have taken an approach explained in Ref. [75] to obtain a confidence interval for cases with low rates. Because the maximum probability density is in general asymmetric around the maximum, it was decided to use the highest probability density interval with the minimal length interval and the highest probability density corresponding to 68% of the area under the likelihood curve. For this interval, no value outside has a higher probability than any value inside.

To verify that the quoted interval corresponds to a one σ error, Monte Carlo simulations of two different physical situations were run and "decay data" was created. Fig. 3.22(a) and 3.22(b) are the results of a simulation of 10000 event sets with 50 decay chains each. Fig. 3.22(c) and 3.22(d) are the results of a simulation of 10000 event sets with 8 decay chains each. Typical expected experimental values of parent, daughter and granddaughter $T_{1/2}$, ϵ_β and β background were used.

Figures 3.22(a) and 3.22(c) show the number of times the input half-life was inside the MLH error bars in percent as a function of the confidence interval chosen for the MLH error bars. A confidence interval of 68% for the error bar correctly predicts the input half-life within the MLH error bar 68% of the time or more. Only in the case with very low statistics (8 decay chains), the confidence interval chosen for the MLH error bars overestimates the uncertainty. Figures 3.22(b) and 3.22(d) show histograms of the difference between the MLH half-life and the input MC half-life. One σ error correspond to a 68% confidence interval when selecting the MLH error bars. The asymmetry in the histograms is due to the asymmetry in the likelihood function as a

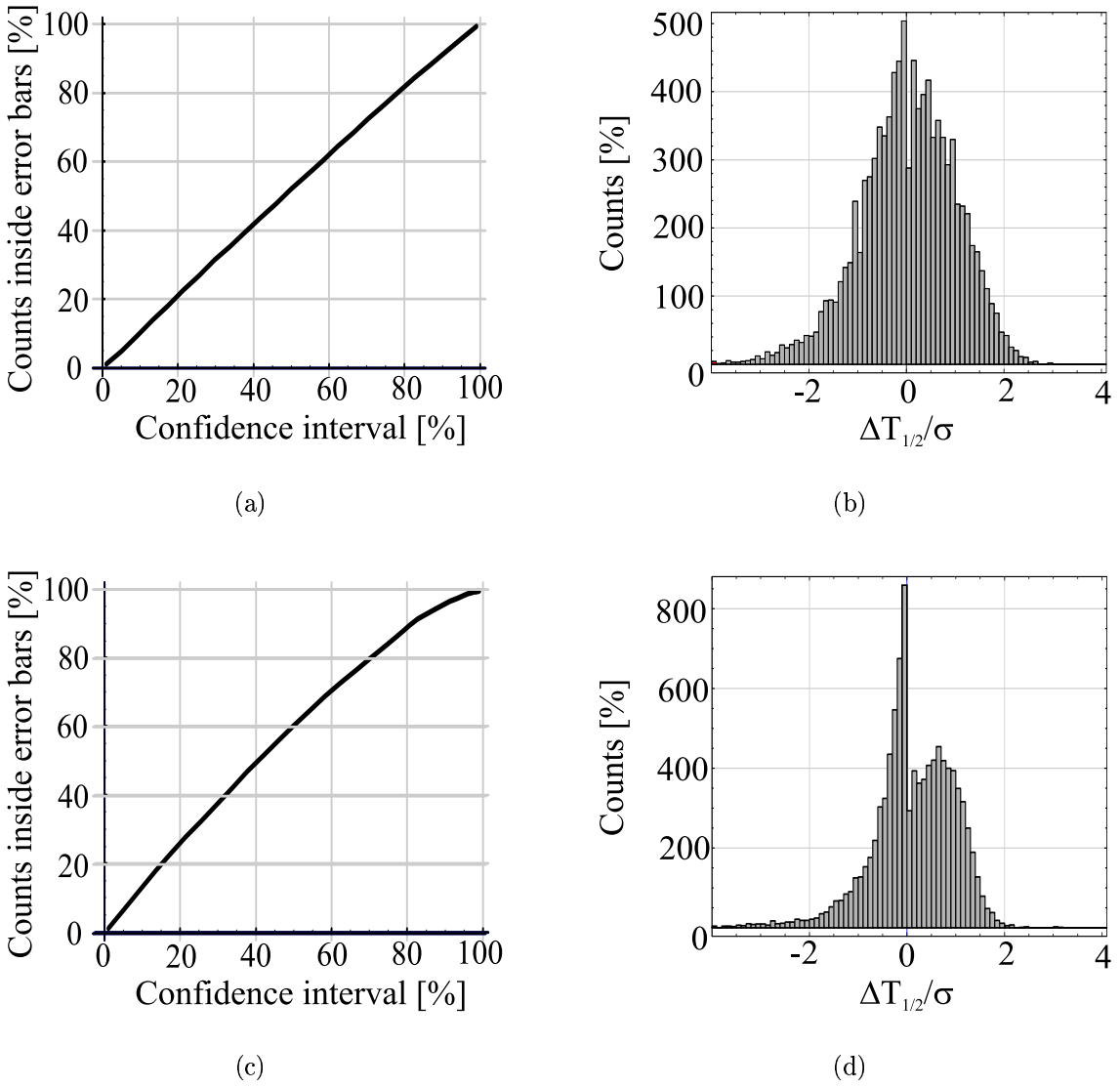

Figure 3.22: Error bars from Monte Carlo simulations of 10000 event sets. a.) number of times the input half-life was inside the MLH error bars in percent as a function of the confidence interval chosen for the MLH error bars when each event set had 50 decay chains. b.) Histogram of the differences between the MLH result and the input MC parent $T_{1/2}$ normalized to one σ when each event set had 50 decay chains. c.) Same as a.) but each event set had 8 decay chains. d.) Same as b.) but each event set had 8 decay chains.

function of parent $T_{1/2}$.

Uncertainties in the daughter and granddaughter half-lives, efficiency and background were included in the systematic error. The β-delayed neutron emission probabilities were taken from theoretical predictions [74] or, if measured, from this work. The largest contribution to the error among the P_n values come from the parent, but their effect is rather small and they do not have a major impact in the $T_{1/2}$ results. To obtain the total error, all the analysis parameters were varied within their uncertainties. An average error for each parameter resulting from its uncertainty was found, and then those errors were added in quadrature together with the average statistical error. The β detection efficiency of the parent decay is the largest systematic uncertainty and it contributes up to 70% of the total error. The uncertainty in the β background and daughter $T_{1/2}$ had similar contributions to the total error and they were usually smaller than 15%. The statistical error is usually larger than individual systematic errors and for cases with low statistics, it has the largest contribution to the total uncertainty.

Uncertainties in the total number of correlated β-n coincidences N_n, total number of β-n background coincidences B, number of parent decays N_β and NERO efficiency ϵ_N affect the total uncertainty of the measured P_n values. The statistical error of N_n was assumed to follow gaussian statistics and it contributes to $\approx$50-70% of the total error. The uncertainty in B contributes to less than 30% of the total and it was calculated using $N \times t_c \times \Delta b_{\beta-n}$ where N is the number of implanted isotopes and t_c is the correlation time. The value of $\Delta b_{\beta-n}$ was calculated to be 0.02 mHz. The uncertainty in N_β is isotope dependent and it is calculated from the intrinsic uncertainty in the fitting procedure that is used to obtain the number of parent decays in Figs. 3.15, 3.16 and 3.17. Uncertainty in the NERO efficiency was calculated to contribute $\approx$ 5% to the total error.

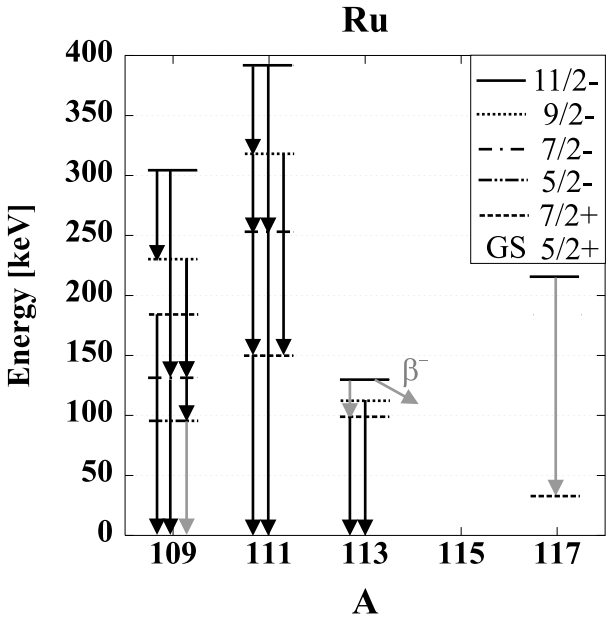

Figure 3.23: Relevant energy levels and decay scheme of neutron-rich Ru isotopes. Known microsecond or longer transitions are shown in gray color. The position and assignment of the energy levels in ^{117}Ru is arbitrary because only the γ energy is known [83].

3.6 Results

Table 3.2 shows the resulting measured half-lives in this work. All the measured half-lives in this work agree with values found in literature within one σ with the exception of ^{121}Ag and ^{115}Ru. ^{121}Ag is within two σ of the known value. For ^{115}Ru one possible explanation of the discrepancy is the possible presence of an isomeric state. Odd $^{109-115}$Pd isotopes are known to have an isomeric $11/2^-$ state with an excitation energy of less than 200 keV as shown in Fig. 3.24 and a half-life longer than 50 s. Such an isomeric state is also known in ^{113}Ru [82] (Fig. 3.23) with a half-life of 0.51(3) s. Tomlin *et al.* [83] also reported the presence of a microsecond isomer in ^{117}Ru. Therefore it seems possible that the discrepancy of our ^{115}Ru half-life to the previous value could be due to an unobserved similar isomer.

The existence of an isomeric state that would lead to a mixture of the measured

Table 3.2: Experimental β-decay half-lives ($T_{1/2}$) and β-delayed neutron emission probabilities (P_n) measured in this work. Previously known data is shown when available.

Isotope	Half-life (ms)		Pn (%)	
	This Work	Previous	This Work	Previous
^{121}Ag	661^{75}_{72}	780(10) [76]		
^{122}Ag	357(24)	550(50)	≤ 1.3	0.186(10) [76]
		200(50) IM [74]		
^{123}Ag	272(24)	293(7) [77]	1.0(5)	0.55(5) [76]
^{124}Ag	187^{15}_{14}	172(5) [77]	1.3(9)	
^{119}Pd	918(111)	920(130) [78]		
^{120}Pd	492(33)	500(100) [58]	≤ 0.7	
^{121}Pd	285(24)		≤ 0.8	
^{122}Pd	175(16)		≤ 2.5	
^{123}Pd	174^{38}_{34}			
^{124}Pd	38^{38}_{19}			
^{116}Rh	688^{52}_{50}	680(60)	≤ 2.1	
		570(50) IM [79]		
^{117}Rh	394^{47}_{43}	440(40) [80]	≤ 7.6	
^{118}Rh	266^{22}_{21}	300(60) [57]	3.1(14)	
^{119}Rh	171(18)		6.4(16)	
^{120}Rh	136^{14}_{13}		≤ 5.4	
^{121}Rh	151^{67}_{58}			
^{114}Ru	510^{69}_{65}	570(50) [81]		
^{115}Ru	405^{96}_{80}	740(80) [56]		
^{116}Ru	204^{32}_{29}			
^{117}Ru	142^{18}_{17}			
^{118}Ru	123^{48}_{35}			
^{114}Tc	91^{62}_{35}	150(30) [55]		
^{115}Tc	73^{32}_{22}			

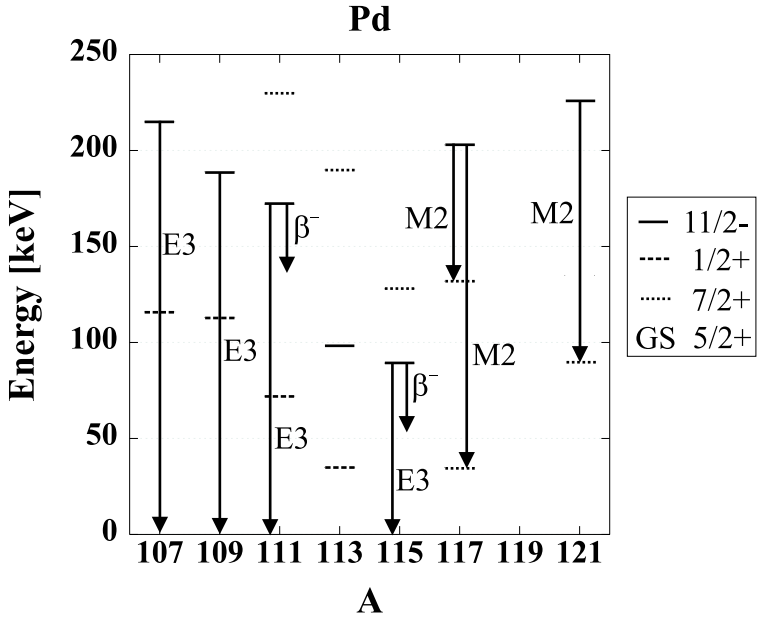

Figure 3.24: Relevant energy levels of neutron-rich Pd isotopes. Known microsecond or longer transitions are shown. The position and assignment of the energy levels in ^{121}Pd is arbitrary because only the γ energy is known [83].

ground state and isomer half-lives in ^{123}Pd is also possible. As mentioned before, odd $^{109-115}$Pd isotopes have a long-lived $11/2^-$ isomer that decays through either a E3 transition to the $5/2^+$ ground state or through beta decay as shown in Fig. 3.24. For ^{117}Pd, the $7/2^+$ energy level drops below the $11/2^-$ energy level and a M2 transition occurs to that intermediate state with $T_{1/2}$=19.1(7) ms [80]. Tomlin *et al.* [83] reported the existence of a microsecond E_γ=135 keV γ-ray from ^{121}Pd that may be due to the $11/2^-$-$7/2^+$ M2 transition. A Weisskopf estimate for a 50 keV M2 transition in ^{123}Pd gives a half-life of the order of milliseconds. Therefore, it seems plausible that an unobserved long-lived isomer exists in ^{123}Pd corresponding to a similar transition. The current reported $T_{1/2}$ value would then be a mixture of the decay of the long-lived isomer and the ground state since it would not be possible to distinguish between them.

The measured ^{122}Ag and ^{116}Rh half-lives in this work correspond to a mixture of

the half-lives of the ground state and a known isomer for each case.

The resulting P_n values are shown in Table 3.2. The current results agree well with previously measured values for ^{122}Ag and ^{123}Ag.

Chapter 4

Analysis and discussion

4.1 Theoretical calculations

To model astrophysical processes such as the r-process requires knowledge of β decay properties of nuclei far from stability. In addition, because such process proceeds through elements from Fe to U, a complete and consistent understanding of nuclear structure through a large mass range is needed. Because the majority of nuclei involved in the r-process have not been studied experimentally, the need for such knowledge has stimulated the development of theoretical models.

There are different types of theoretical models: some start from basic microscopic principles and include nuclear correlations (shell model), some attempt to achieve self-consistency (HFB+QRPA) and other emphasize global applicability (macro/microscopic mass model+QRPA). Modeling an r-process requires a global knowledge of nuclear properties and because it is generally used in self-consistent r-process calculations, the macro/microscopic mass model+QRPA was used in this work.

The macro/microscopic mass model+QRPA model divides the problem into three steps. First of all, ground state masses and deformation parameters of nuclei are calculated in a macroscopic description that includes microscopic effects based on the Strutinski method of adding shell effects plus a pairing correction. We have used the

finite-range droplet model (FRDM) [48] and the extended Thomas-Fermi with Strutinsky integral (ETFSI-Q) model [16] to obtain the ground state masses and deformation parameters. The ETFSI formalism is based on a Skyrme-type force Hartree-Fock approach and BCS pairing. The basic idea behind the FRDM and ETFSI-Q methods involves calculating the total potential energy as a function of proton and neutron numbers. The potential energy is the sum of a macroscopic term plus a microscopic term representing the shell plus pairing corrections. Because some aspects of the FRDM are later used in the calculation of the β-decay rates, only the FRDM method is going to be explained with some detail.

The macroscopic term of the FRDM mass model is based on the droplet model, which accounts for the finite range of the nuclear force and includes higher order terms in $A^{-1/3}$ and $(N-Z)/A$ in order to add nuclear compressibility and variations in the proton and neutron radii, respectively. The microscopic term is divided into the shell and pairing corrections calculated from a set of single-particle levels. Wave functions were obtained using a potential which included a spin-independent nuclear part in the form a folded-Yukawa potential, a spin-orbit part and the coulomb potential felt by the protons.

The shape of the nuclear surface depends on the quadrupole deformation ϵ_2, hexadecapole deformation ϵ_4 and higher terms. To use this parameterization of the shape of a nucleus, a procedure motivated by the Nilsson modified-oscillator model was used. Starting from a deformed harmonic oscillator potential (Nilsson modified-oscillator model), the shape of the nuclear surface is found by equating it to an equipotential surface. Because the single-particle potential is dependent on the shape of the nucleus, ϵ_2 and ϵ_4 become free parameters that are to be calculated. To introduce pairing effects, the Lipkin-Nogami pairing model is used with a constant pairing interaction acting between doubly-degenerate single-particle levels starting below the Fermi surface. In this approach, a set of coupled nonlinear equations are solved and quasi-particle energies and occupation probabilities are found.

Shell effects were included using the Strutinsky method. In this method, the shell correction is calculated by subtracting the energy of a "uniform" distribution of states (gaussian shape for each state) from the sum of the energies of single-particle levels weighted by their occupation probabilities.

Potential energy surfaces are calculated as a function of quadrupole ϵ_2 and hexadecapole ϵ_4 deformation. The ground state of a nucleus corresponds to the minimum of this surface.

The second step in the macro/microscopic mass model+QRPA calculation consists in taking either the FRDM or ETFSI-Q mass models' ground-state shapes to find single-particle levels using the same folded-Yukawa potential with the Lipkin-Nogami pairing model used in the FRDM calculation. In a third and final step, the Gamow-Teller component of the β-decay is calculated using the operator

$$\beta^{1\pm} = G_A \sum_{i}^{A} (\sigma\tau^{\pm})_i, \tag{4.1}$$

where G_A is a coupling constant, the operator t^- changes a neutron into a proton and σ is the spin operator. The β-strength function S_β which contains the nuclear structure information of the decay is proportional to $< \phi_f|\beta^{1+}|\phi_i >^2$. This type of decay is the dominant form of decay on the neutron-rich side due to the discrepancy in the number of neutrons and protons.

In terms of the strength function, the half-life $T_{1/2}$ using Fermi's golden rule is given by,

$$\frac{1}{T_{1/2}} = \sum_{E_i \geq 0}^{E_i \leq Q_\beta} S_\beta(E_i) \times f(Z, Q_\beta - E_i), \tag{4.2}$$

where Q_β is the Q value of the decay and $f(Z, Q_\beta - E_i)$ is the Fermi function. The energy dependent phase space factor $f \approx (Q_\beta - E_i)^5$ strongly weighs the low-energy part of the excitation spectrum and therefore $T_{1/2}$ is dominated by the lowest energy resonances in the strength function.

The β-delayed neutron emission probability is calculated as the ratio of the transition probability to states above the neutron separation energy S_n,

$$P_n = \frac{\sum_{B_n}^{Q_\beta} S_\beta(E_i) \times f(Z, Q_\beta - E_i)}{\sum_{0}^{Q_\beta} S_\beta(E_i) \times f(Z, Q_\beta - E_i)}. \tag{4.3}$$

This method neglects possible γ decays from states above the neutron separation energy. This simplification is justified in most, but not all cases [74].

4.2 Discussion

In Fig. 4.1 our measured experimental half-lives values are compared with theoretical predictions. The Q_β value and S_n were taken from extrapolations from measured values [84], and the deformations ϵ_2 and ϵ_4 from the FRDM or the ETFSI-Q mass models. The predictions and the experimental values agree within a factor of 3, which is well within the expected model uncertainties [47]. The only exceptions are the half-lives of ^{119}Pd and ^{124}Pd. Closer examination reveals a trend for the models to over-predict the half-lives for ruthenium and palladium isotopes. On the other hand, while the rhodium predictions using the FRDM deformations reveal a trend to under-predict the half-lives, the predictions using ETFSI-Q deformations indicate no systematic trend for the more neutron-rich isotopes.

The neutron emission probabilities P_n values provide additional nuclear structure constraints as they probe the β-strength distribution above the neutron separation energy. The experimental neutron emission probabilities are compared in Fig. 4.2 with theoretical predictions. In general, the comparisons agree very well, and the only surprise is the low measured P_n value of ^{120}Rh.

As mentioned before, the QRPA model is a microscopic-macroscopic approach and as such, it lacks a complete description of the inner workings at the microscopic level. Furthermore, it was designed as a unified approach to predict nuclear structure

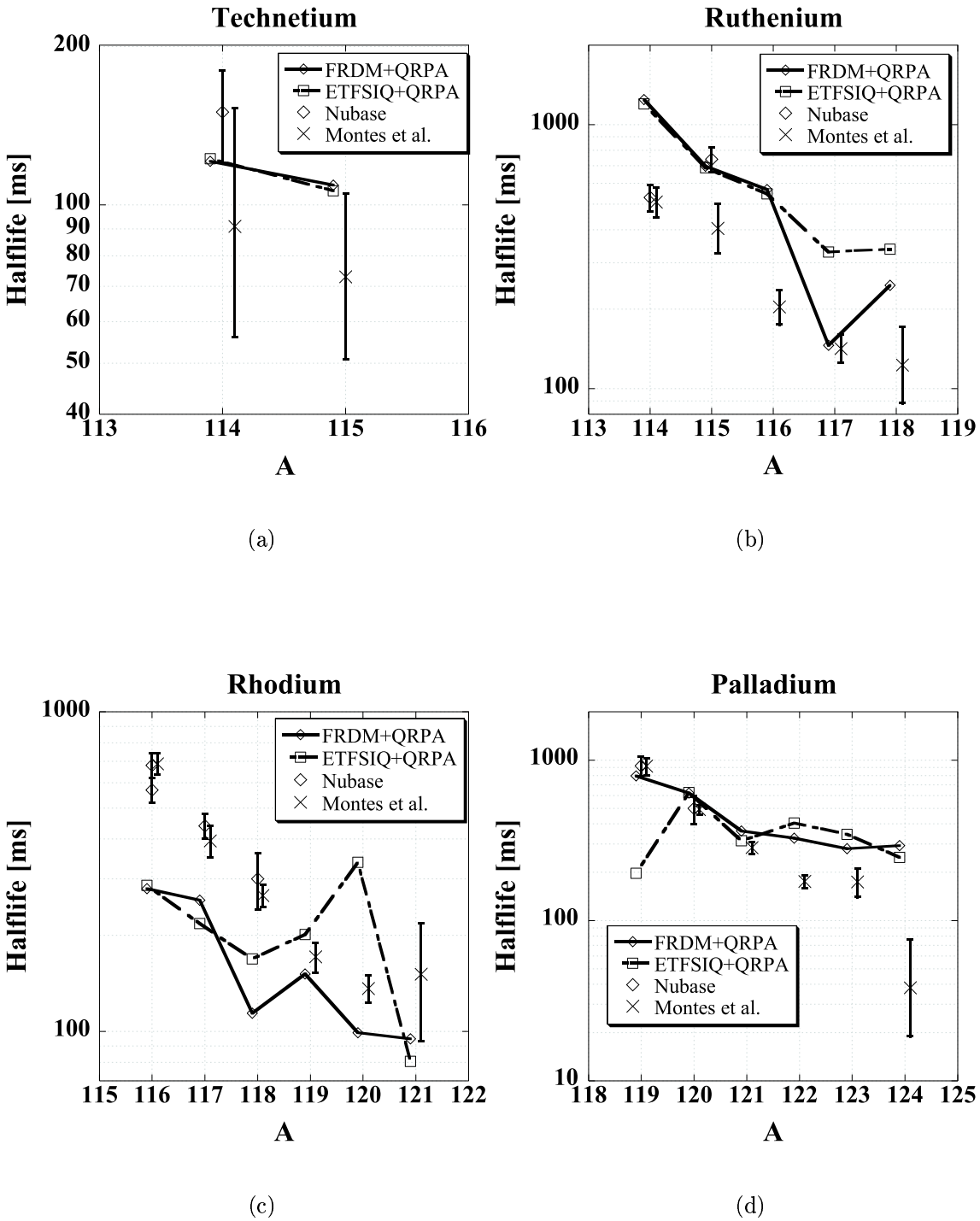

Figure 4.1: Experimental half-lives from this work and from literature compared with QRPA calculations using mass extrapolations and the FRDM and ETFSI-Q ground state deformation predictions.

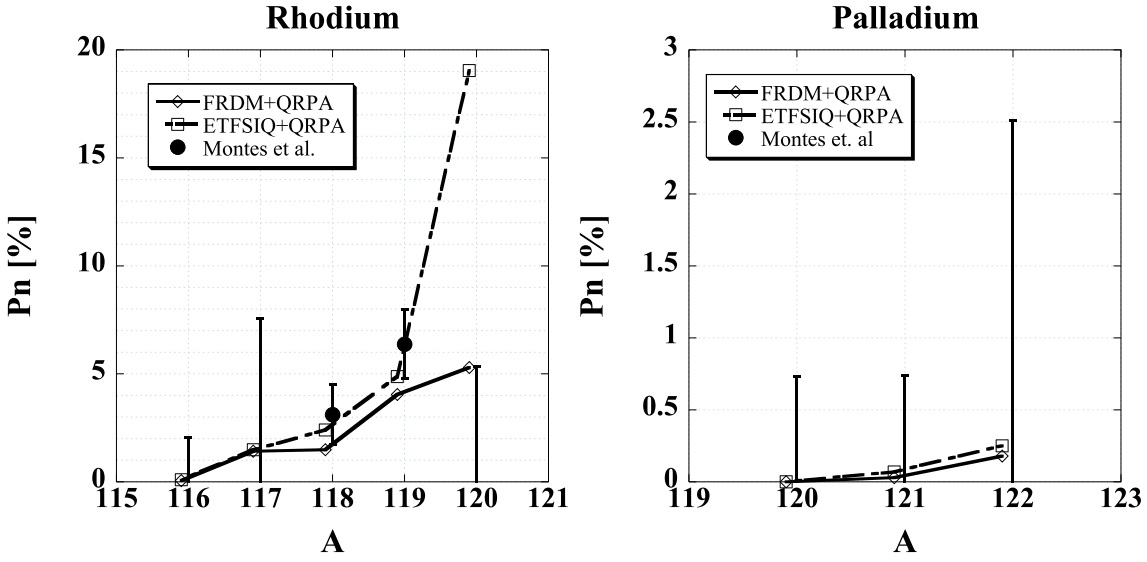

(a)

(b)

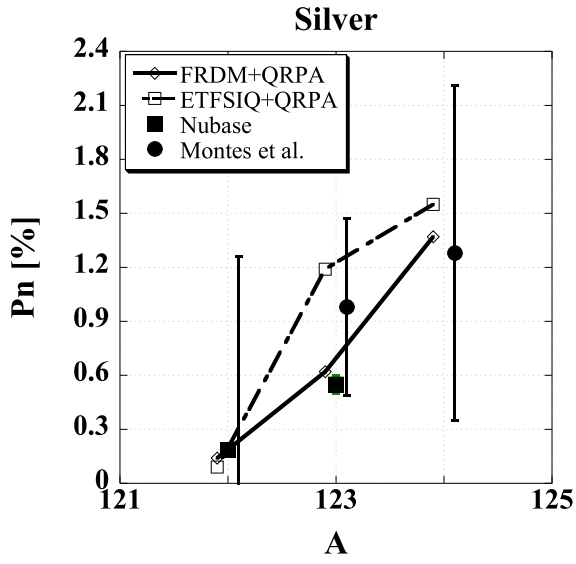

(c)

Figure 4.2: Experimental β-delayed neutron emission probabilities from this work and from literature compared with QRPA calculations using mass extrapolations and the FRDM and ETFSI-Q ground state deformation predictions.

quantities of any given nucleus. Free parameters of the model were chosen based on *known* nuclear properties. In addition to the underlying uncertainties within the model, input parameters as deformation values ϵ_2 or ϵ_4, level order, or Q_β value have a direct bearing in the β-decay rates and P_n values. Uncertainties in those input parameters are therefore entangled in the quoted expected uncertainty of the model.

As the neutron number is increased from mid-shell to a closed shell, the shape of the nucleus is expected to change from deformed to spherical at the shell closure. For the case of Tc, Ru and Rh, both FRDM and ETFSI-Q models predict oblate shapes that become less deformed with increasing neutron number as shown in Fig. 4.3. For some of the Pd and Ag isotopes, both models predict different shapes (prolate and oblate) and even within the same model, jumps between an oblate and prolate shape occur as the number of neutrons is increased. In addition, the FRDM mass model predicts for ^{121,124}Pd and $^{120-124}$Ag isotopes two mass minima within 200 keV. This is less than the typical mass model uncertainty of 680 keV [48]. In those cases, the two mass minima also have quadrupole shape parameters with opposite signs.

Due to the uncertainty in the predicted shape deformation from the theoretical models, it was decided to study systematically the effect of changing the deformation from an oblate shape ($\epsilon_2 = -0.3$) to a prolate shape ($\epsilon_2 = 0.3$) for all the isotopes of interest. In addition, both half-life and P_n can serve as probes of the nuclear shape by finding the "correct" quadrupole deformation that would result in the experimentally measured value. In cases where measured half-lives and P_n are available, the system is further constrained by deformations that would "correctly" predict both. The results are summarized in Fig. 4.3 where theoretical deformations used in the QRPA that predict experimental half-lives and P_n values are shown.

Figure 4.4 shows theoretical Ru half-lives as a function of quadrupole deformation ϵ_2 keeping ϵ_4=0. Shaded regions correspond to the experimental value. The absolute minimum from the FRDM or ETFSI-Q mass models predict some hexadecapole deformation ϵ_4, but its influence on the half-life is smaller by at least an order of magnitude

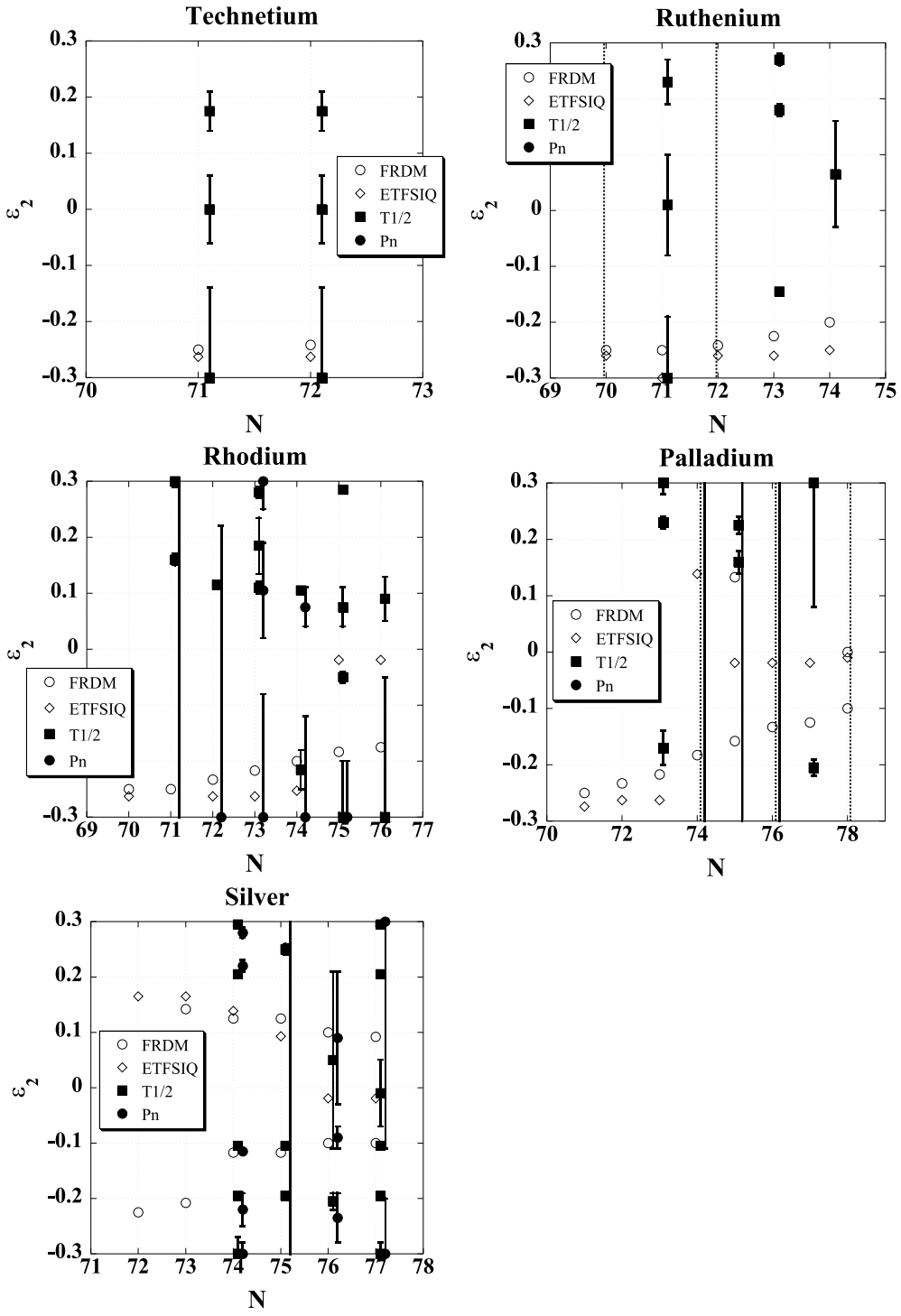

Figure 4.3: Theoretical deformations that predict the measured half-lives (black squares) and the measured P_n values (black circles) in this work (with the exceptions of ^{115}Ru, ^{116}Rh and ^{122}Ag where the known ground state $T_{1/2}$ was used, and of ^{121}Ag where the known P_n value was used). Predicted deformations from the FRDM and ETFSI-Q mass models are also shown. Thick lines going from top to bottom correspond to cases in which any deformation in the range $-0.3 \leq \epsilon_2 \leq 0.3$ predicts the measured P_n. Dotted lines going from top to bottom correspond to cases in which no deformation in the range $-0.3 \leq \epsilon_2 \leq 0.3$ predicts the measured half-life.

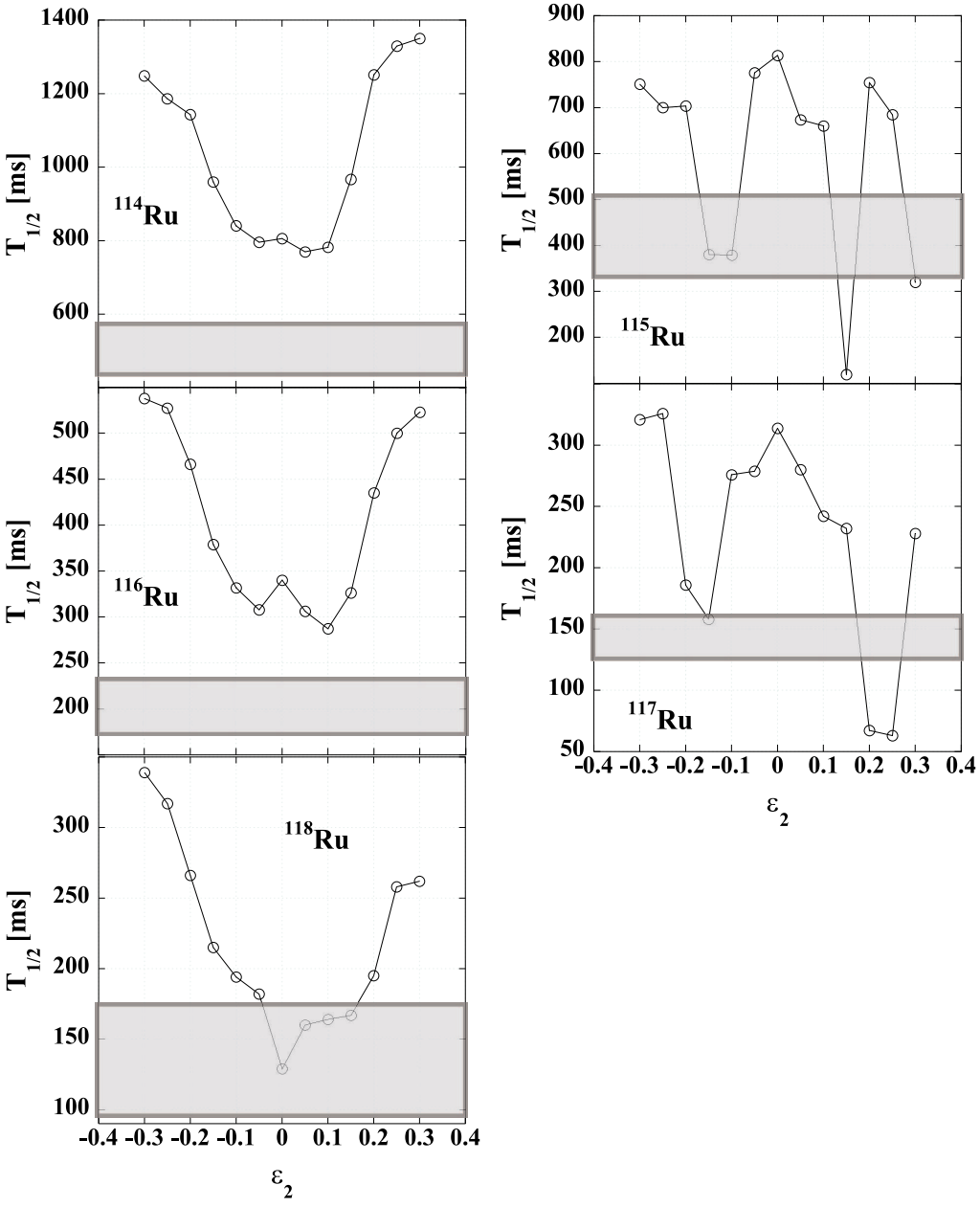

Figure 4.4: Theoretical half-lives of Ru isotopes as a function of quadrupole deformation ϵ_2 with $\epsilon_4 = 0$. Shaded regions correspond to the experimental $T_{1/2}$ in this work.

than the quadrupole deformation ϵ_2. For the even-even ^{114,116}Ru isotopes, there is no deformation that would predict the correct half-life, while for ^{118}Ru a spherical or slightly prolate shape would predict the measured value. For ^{115,117}Ru the situation is not as clear as either an oblate or prolate shape predict the experimental half-lives.

In the case of Rh isotopes both $T_{1/2}$ and P_n are shown in Fig. 4.5 and Fig. 4.6 as a function of quadrupole deformation. Shaded regions correspond to the experimental value. There are deformations that predict the experimental $T_{1/2}$ and P_n values of all Rh isotopes. For $^{116-119}$Rh a deformation value around $\epsilon \approx 0.1 - 0.15$ (prolate shape) is consistent with the half-life and the P_n. The theoretical models on the other hand, predict a value of $\epsilon \approx -0.3 - -0.2$ (oblate shape). For ^{120}Rh, while the FRDM prediction agrees with the measured value, the ETFSI-Q model overpredicts the P_n value of ^{120}Rh by almost a factor of 4. Because of this overprediction, it was decided to study systematically the effect of the uncertainty in the Q_β value and in the quadrupole deformation.

From the mass extrapolation taken from [84], Q_β=10.92±0.61 MeV for the decay of ^{120}Rh into ^{120}Pd. Figure 4.7 shows the dependence of the half-lives and P_n as a function of quadrupole deformation using the upper and lower limit of the extrapolated Q_β value. As before, the shaded region corresponds to the experimental values in this work. Uncertainties in the quadrupole deformation and in the Q_β values explain the discrepancy of the predicted P_n value with the current experimental result as shown in Fig. 4.7. The discrepancy may also be due to the incorrect energy placement of the dominant GT feeding ($\nu g_{7/2} \rightarrow \pi g_{9/2}$) above the neutron separation energy to ^{120}Pd. Such an energy shift would produce a lowering of the predicted $T_{1/2}$ bringing the predicted ETFSI-Q value closer to the measured one but it would increase the disagreement with the FRDM prediction. Spectroscopic information is needed and a definitive conclusion is beyond the scope of the current work.

Theoretical half-lives of Pd isotopes are shown in Fig. 4.8 as a function of quadrupole deformation. Again, shaded regions correspond to the measured value in this

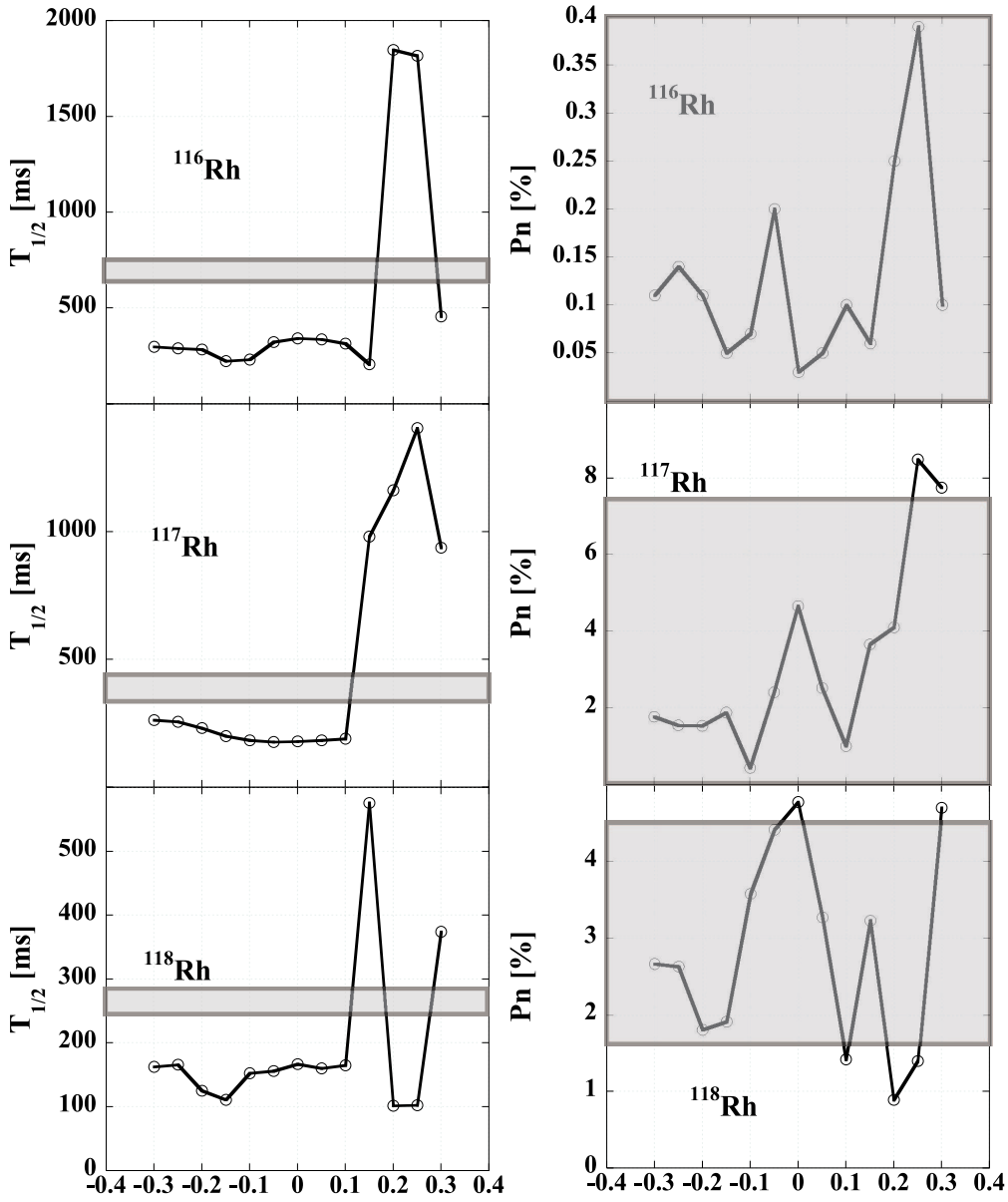

Figure 4.5: Theoretical half-lives of $^{116-118}$Rh isotopes as a function of quadrupole deformation ϵ_2 with $\epsilon_4 = 0$. Shaded regions correspond to the experimental $T_{1/2}$ or P_n in this work.

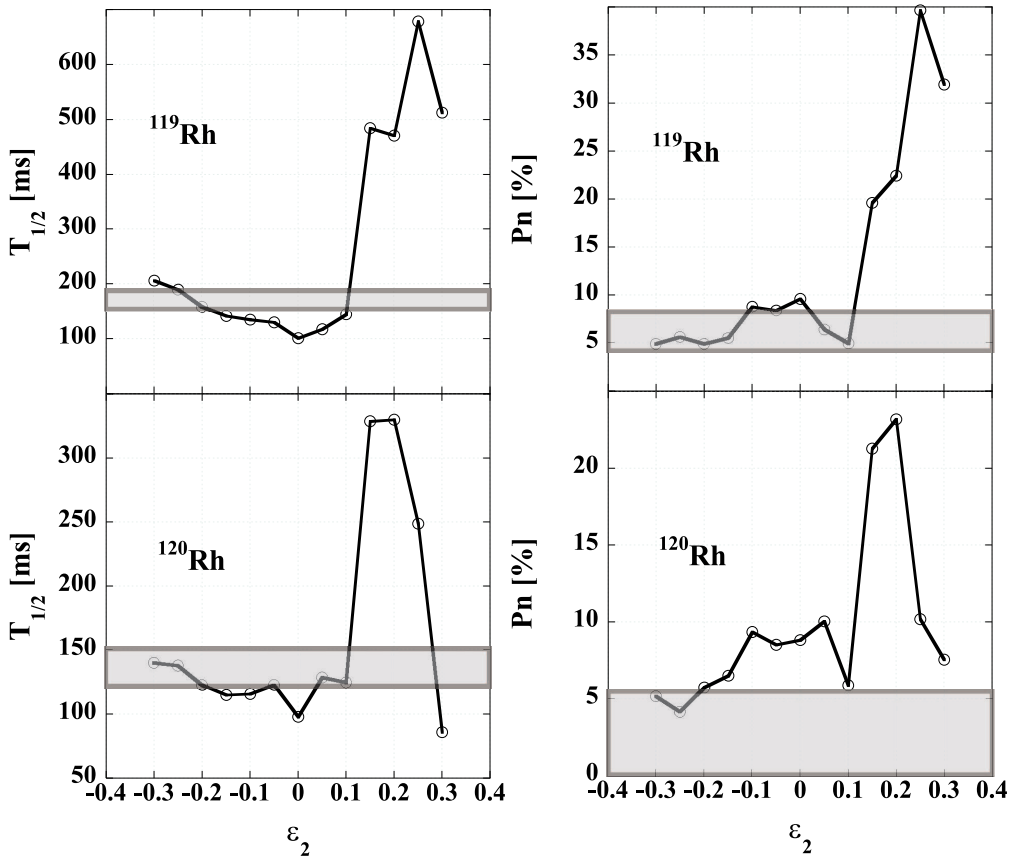

Figure 4.6: Theoretical half-lives of ^{119,120}Rh isotopes as a function of quadrupole deformation ϵ_2 with $\epsilon_4 = 0$. Shaded regions correspond to the experimental $T_{1/2}$ or P_n in this work.

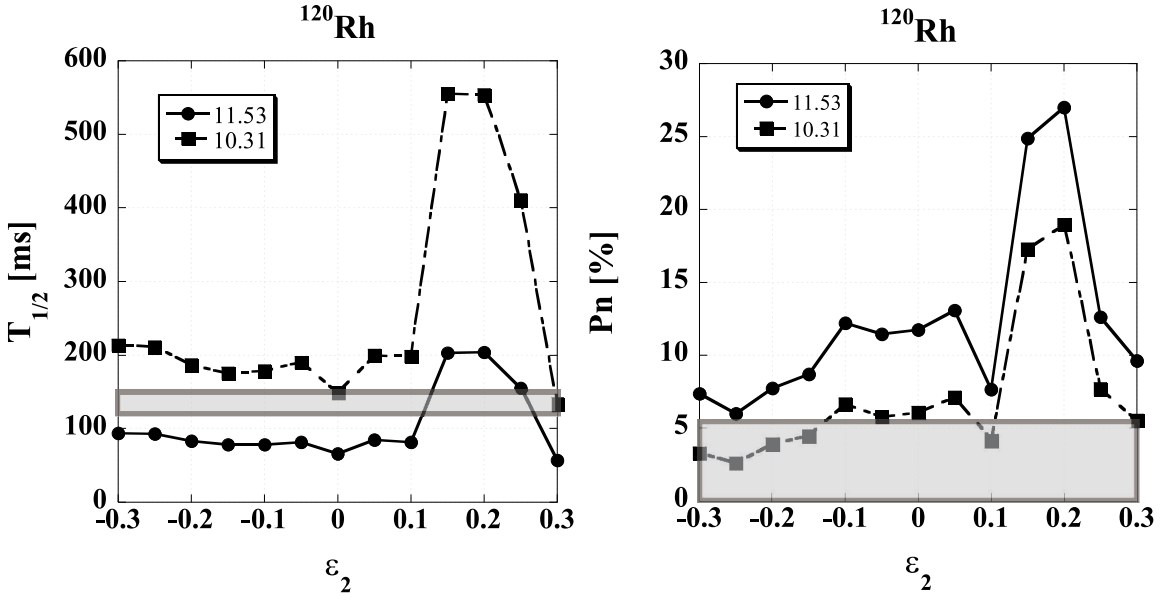

Figure 4.7: Theoretical ^{120}Rh $T_{1/2}$ and P_n values calculated as a function of quadrupole deformation ϵ_2 with $\epsilon_4 = 0$ using a QRPA model. The two lines correspond to the upper and lower limit of the Q_β [MeV] input value in the QRPA calculation. The shaded region correspond to the experimental $T_{1/2}$ or P_n obtained in this work.

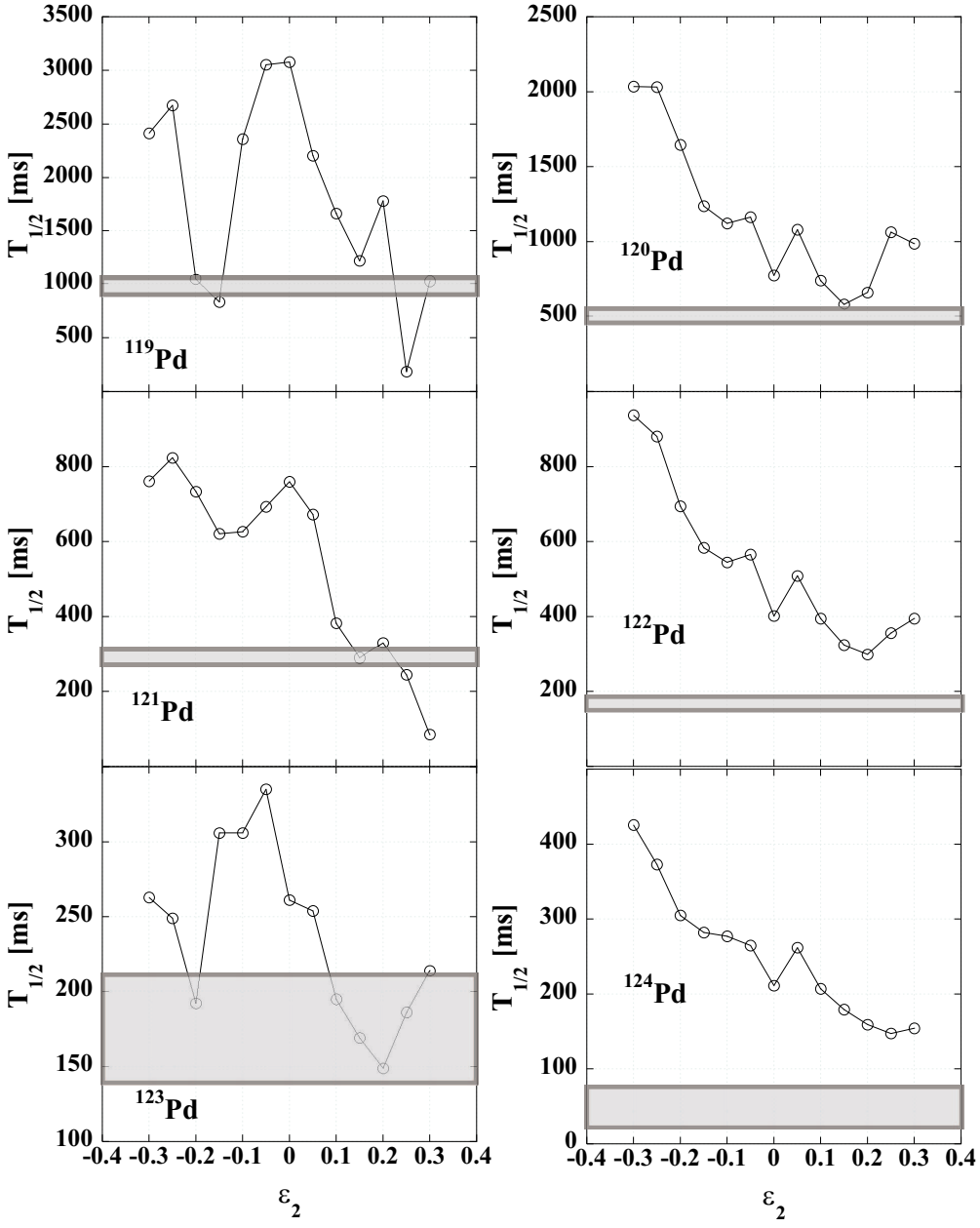

Figure 4.8: Theoretical half-lives of Pd isotopes as a function of quadrupole deformation ϵ_2 with $\epsilon_4 = 0$. Shaded region correspond to the experimental $T_{1/2}$ or P_n in this work.

work. P_n values are not shown for $^{120-122}$Pd because in those cases any deformation in the range $-0.3 \leq \epsilon_2 \leq 0.3$ predicts the measured value within the error bars and no new information is gained. For the even-even ^{120,122,124}Pd isotopes there is neither an oblate nor a prolate deformation that predict the experimental value. For the even-odd ^{119,121,123}Pd isotopes there is, on the other hand, both oblate and prolate shapes that match the experimental value. The absolute values of the deformations for ^{121,123}Pd are higher than the predicted quadrupole deformations either from the FRDM or the ETFSI-Q mass model as shown in Fig. 4.3. We did not, however, found any systematic trend that would explain the theoretical over-prediction of the experimental half-lives. In the case of ^{119}Pd, it is seen that the half-life value is very sensitive to the quadrupole deformation used, which could explain the discrepancy between prediction and experiment.

Because the predicted half-life is the combination of different parameters, another possibility to explain the over-prediction of the Pd isotopes' half-lives is that the Q_β values of the β-decay from the extrapolations are systematically too low for the Pd isotopes. To further explore this possibility, Fig. 4.9 shows theoretical half-lives using the Q_β value, S_n and deformations ϵ_2 and ϵ_4 from the FRDM and ETFSI-Q mass models instead of from mass extrapolations. While the Q_β values are lower for the FRDM than either extrapolations or ETFSI-Q mass models, the ETFSI-Q Q_β are higher than the values from the mass extrapolations. The difference in Q_β between ETFSI-Q and FRDM mass models is in the range 0.5-1.4 MeV. Even though the ETFSI-Q predictions are still higher than the measured $T_{1/2}$ for N$\geq$76, they do a better job than the FRDM results except for ^{119}Pd. An increase in the Q_β value to better reproduce the experimental results would be consistent with a weakening of the neutron shell closure observed by the Pd isotopes. Systematic problems in the predicted β-strength functions in principle could also play a role and therefore, a definite conclusion based solely on the basis of the half-lives cannot be drawn.

Figure 4.10 shows theoretical half-lives and P_n values of Ag isotopes as a func-

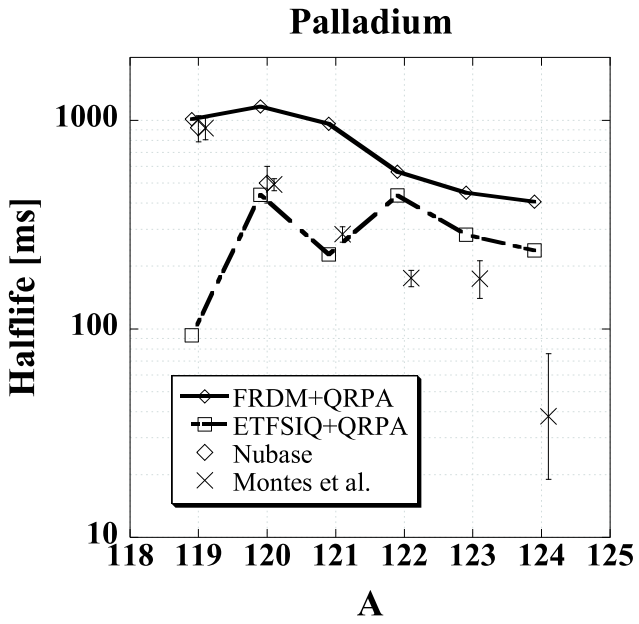

Figure 4.9: Experimental half-lives from this work and from literature compared with QRPA calculations using FRDM and ETFSI-Q ground state deformation, Q-value and S_n predictions.

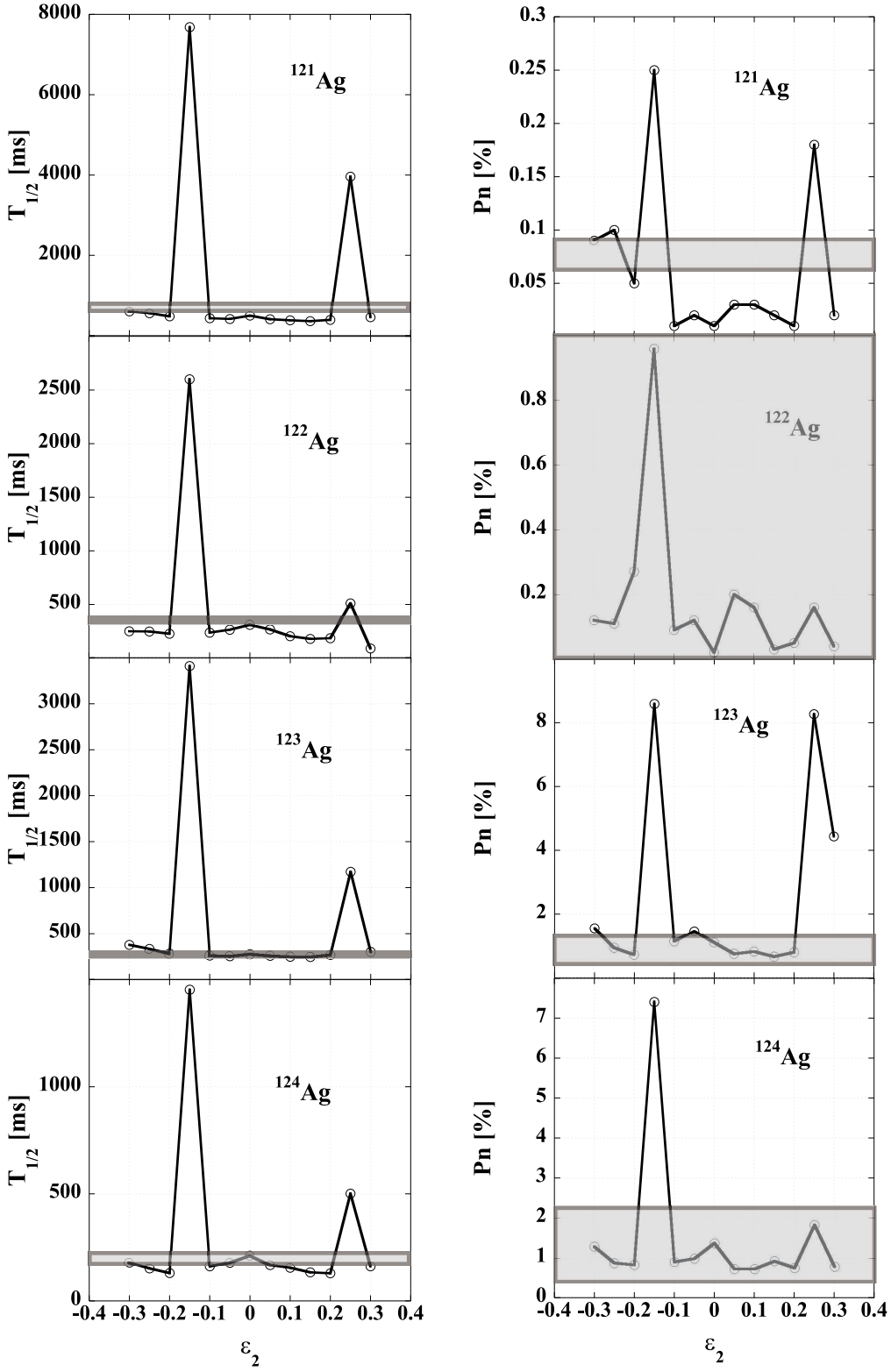

Figure 4.10: Theoretical half-lives and P_n values of Ag isotopes as a function of quadrupole deformation ϵ_2 with $\epsilon_4 = 0$. Shaded region correspond to the experimental $T_{1/2}$ or P_n in this work (with the exception of the P_n of ^{121}Ag where a previously known value was used).

tion of quadrupole deformation. From N=73 to more neutron-rich, the FRDM mass model predicts two minima within 200 keV with about the same absolute value of ϵ_2, one oblate and the other prolate. Even though the predicted deformations that would agree with experimental values are consistent in general for the half-lives and P_n values, those deformations may be oblate and prolate and a conclusion is not straightforward.

4.3 Astrophysical impact

To study the impact of the new experimental P_n values, a classical r-process calculation was used. Isotopic abundances were determined assuming that a (n,γ)$\rightleftharpoons$(γ,n) equilibrium is quickly obtained before any β-decay occurs. At every time step, isotopic abundances were first calculated using Eq. 4.4 neglecting differences in the ratios of the partition functions. Each isotopic chain had a total abundance equal to $Y(Z) = \sum_A Y(Z,A)$. Once the isotopic abundances were calculated assuming equilibrium in an isotopic chain, their sum was normalized to $Y(Z)$. The final isotopic abundances in the time step were obtained taking into account only the β-decay flow. The abundance flow from each isotope to the next by β-decay is determined by the expression,

$$\begin{aligned}\frac{dY(Z,A)}{dt} &= Y(Z-1,A)(1-P_n^{(Z-1,A)})\lambda_\beta^{(Z-1,A)} \\ &\quad +Y(Z-1,A+1)P_n^{(Z-1,A+1)}\lambda_\beta^{(Z-1,A+1)} - Y(Z,A)\lambda_\beta^{Z,A}, \quad (4.4)\end{aligned}$$

where λ_β is the β-decay rate. This process repeats for the time τ to be determined by the fit to solar r-process abundances. After the time τ, freeze-out occurs and only β-decays were considered.

The solar r-process abundance pattern is shown in Fig. 4.11 along with two simulated classical r-process patterns. In both classical calculations, existing experimental

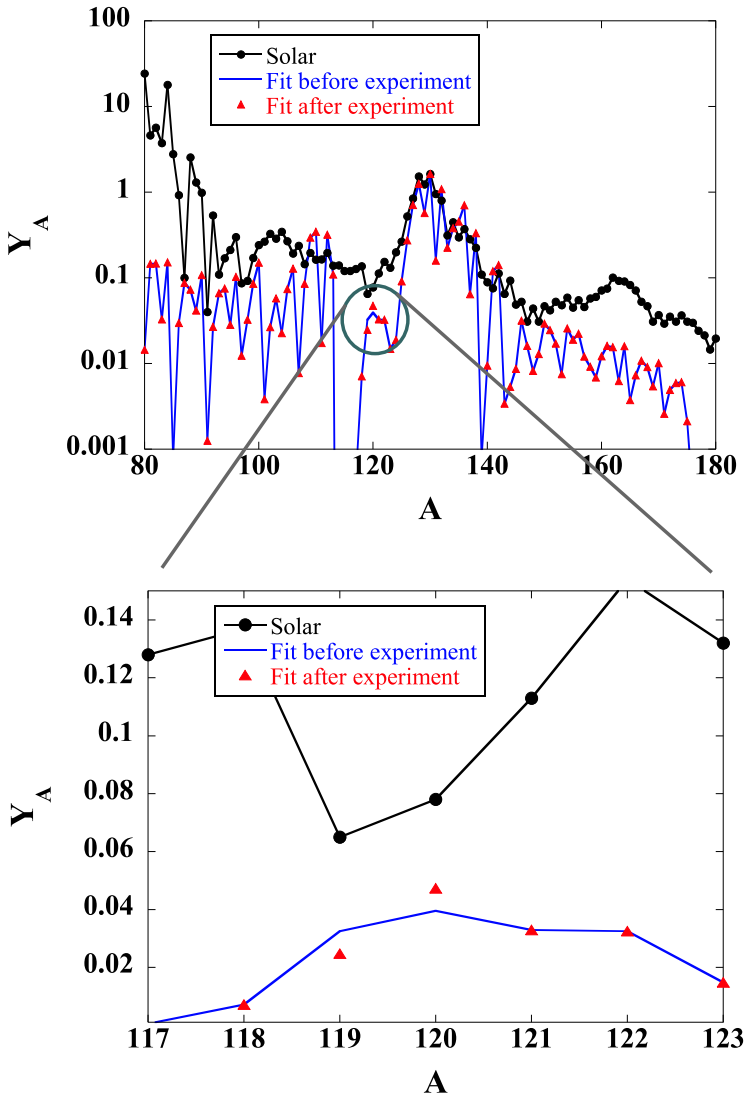

Figure 4.11: Solar and calculated r-process abundances using a one component (n_n=5×10^{23} cm^{-3}, T=1.35 GK, τ=2 s) classical r-process code. Experimental information available before this work was used in the classical r-process calculations (blue line). Red triangles represent a simulation that also included the half-lives and P_n values measured in this work. The ETFSI-Q and QRPA models were used to obtain theoretical values necessary for the simulation.

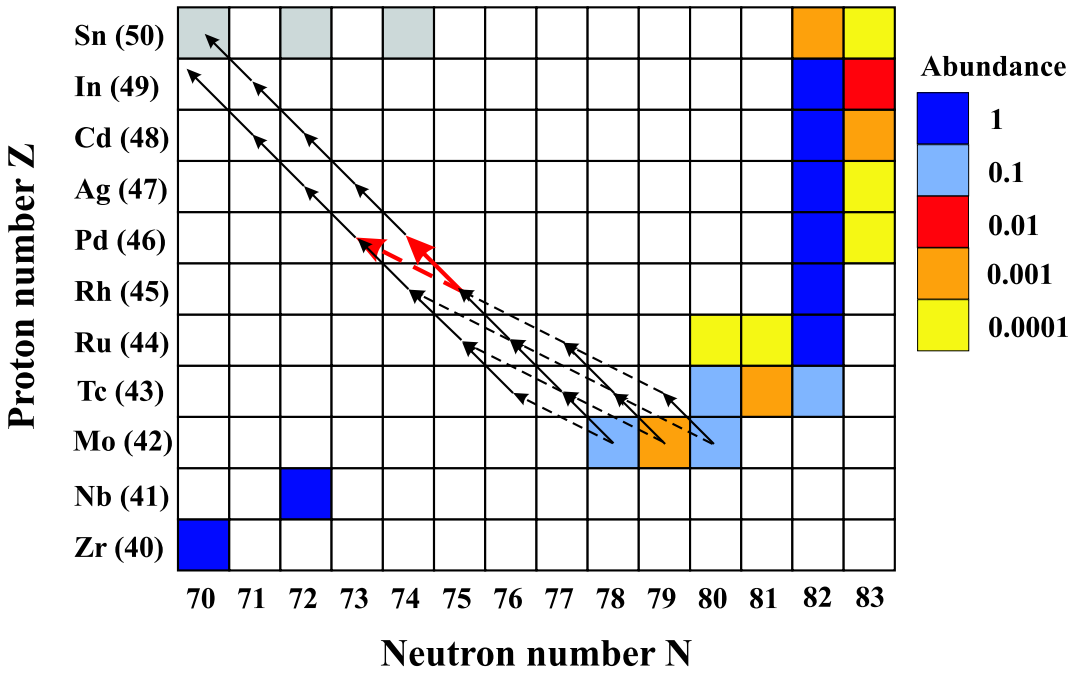

Figure 4.12: Mass region showing the calculated isotopic abundances just before freezeout. Largest abundances were normalized to 1. Stable isotopes are shown in gray. The most important β-decay rates that affect the ^{120}Sn/^{119}Sn abundance ratio are also shown. The β-decay rate in red represents the ^{120}Rh P_n value measured in this work.

data available before this work was used. The simulation represented with red triangles *included* the half-lives and P_n values measured in this work. The ETFSI-Q mass model was used to calculate theoretical masses and the QRPA+ETFSI-Q model was used to calculated unknown $T_{1/2}$ and P_n values. A neutron density 5×10^{23} cm^{-3}, temperature 1.35 GK and a τ time of 2 s were chosen to best reproduce the solar r-process $A \approx 130$ abundance peak.

Fig. 4.12 shows the isotopic abundances just before freezeout. Even though in principle all the half-lives of participating isotopes are used in Eq. 4.4, only the ones belonging to isotopes with high abundance $Y(Z, A)$ are important for the calculation. Because the proposed r-process path before freezeout is further out from stability as shown in Fig. 4.12, the measured Tc, Ru, Rh and Pd half-lives do not directly affect the final abundance pattern. The measured P_n values, on the other hand, are direct inputs in the calculation and they directly affect the final abundance pattern.

Since, with the exception of ^{120}Rh, there is good agreement between theory and experimental values, the only noticeable effect in the final abundance pattern is due to the low experimental P_n of ^{120}Rh. It is found that it strongly affects the abundance ratio of ^{120}Sn/^{119}Sn produced in the r-process. With the low measured P_n value instead of the QRPA prediction using the ETFSI-Q mass model, the ^{120}Sn/^{119}Sn ratio increases by 40% from 1.22 to 1.66, still inside the value of 1.3(5) deduced from solar system abundances and s-process models [10]. The large error in the solar r-process isotopic abundances is due to the 21% and 10% uncertainties in the s-process contribution of ^{119}Sn and ^{120}Sn, respectively. This ratio is dependent on the predictions of P_n values of the more neutron rich isobars as shown in Fig. 4.12, on the predictions for the half-lives of the progenitors in the r-process path, and on the astrophysical assumptions.

4.4 Conclusions and outlook

New or improved half-lives of very neutron-rich $^{114-115}$Tc, $^{114-118}$Ru, $^{116-121}$Rh, $^{119-124}$Pd, and P_n values (or upper limits) for $^{116-120}$Rh, $^{120-122}$Pd and $^{122-124}$Ag isotopes have been measured. In general, there is reasonable agreement between measurements and the QRPA results within the expected model uncertainties. The only surprise is the low measured value of the ^{120}Rh P_n value. Because of this discrepancy, and because the measured neutron branchings are direct inputs in r-process models, current r-process calculations have somewhat modified final abundance pattern.

A correct understanding of the nuclear structure from mid-shell to the N=82 shell closure is desired in this mass region because of its relevance in the r-process. Even though it is not possible to make definite statements about shell structure in the very neutron-rich Tc-Pd region based on the measured $T_{1/2}$ and P_n values, comparison with theoretical QRPA predictions provide insight into this region. Systematic trends in the $T_{1/2}$ and P_n values can be used to disentangle uncertainties from the QRPA

model itself and uncertainties in the input parameters such as Q_β value and quadrupole deformation ϵ_2. It was found that for $^{116-119}$Rh isotopes, the absolute values of ϵ_2 deformations have to be maintained or slightly reduced from predicted FRDM and ETFSI-Q models to agree with measured $T_{1/2}$ and P_n values. For the ^{121,123}Pd isotopes, a systematic increase in Q_β values best reproduces the experimental values. Such an increase in the Q_β values for the exotic Pd isotopes would be consistent with a relative weakening of the neutron shell closure seen for N$\geq$75 Pd isotopes. In section 1.3, it was pointed out that sufficient amounts of nuclei are created in the mass region A=112-123 in r-process calculations if one assumes the ETFSI-Q mass model. Because this mass model assumes a weakening of the N=82 shell closure, one is tempted to assume that the possible large Q_β value of the Pd isotopes is an additional signature of nuclear structure for extremely neutron-rich nuclei. However, because systematic problems in the predicted β-strength functions could in principle also play a role, the ETFSI-Q model might be compensating for other nuclear structure deficiencies. Measurements and spectroscopic data are needed before definite conclusions can be reached.

The measured P_n values are direct inputs in r-process network calculations. The isotopic abundance ratio ^{120}Sn/^{119}Sn increases by 40% when using the experimental values instead of the prediction by the ETFSI-Q mass model. Further β-decay measurements in this mass region would affect final abundances precisely where the theoretical models with a strong shell-closure predict an abundance through at $A \approx 115$.

The current experiment made use of a new technique at the NSCL to measure the kinetic energy of the implanting fragments. Such a measurement is necessary for distinguishing charge states of the fragments in the particle identification. This paves the way for more experiments to study more very neutron-rich nuclei in this mass region. This is necessary to finally disentangle nuclear from astrophysical effects when studying the r-process.

Chapter 5

Is there a *weak r − process*?

5.1 Abundances

In Section 1.3.1, discrepancies between elemental abundances from recently observed r-process rich metal-poor stars and solar system r-process abundances were shown. While for Ba and heavier elements the abundances agree within error bars, there are noticeable differences for lighter elements $38 \leq Z \leq 47$.

To better observe the discrepancies between solar and the r-process rich metal-poor star abundances, the difference $\Delta log\epsilon = log\epsilon^{star} - log\epsilon^{r-solar}$ (for a definition see Appendix A) is shown in Fig. 5.1 and Fig. 5.2, where $r - solar$ refers to the solar r-process abundance. Two different r-process solar abundances are used because of ambiguities in the main component s-process contributions. Two s-process models (Travaglio *et al*. [14] and Arlandini *et al*. [10]), explained in Section 1.2, were used. The resulting two different patterns of solar r-process abundances are shown in Fig. 1.5. The difference $\Delta log\epsilon$ shows that in the Travaglio case, the lighter elemental metal-poor star abundances are lower than the solar r- abundances. Using the Arlandini model, such observation is still valid for $42 \leq Z \leq 47$. The abundance pattern below Ba seems to be consistent from star to star and the discrepancies are within the observational uncertainties. The average of the differences for all the stellar abundances are also

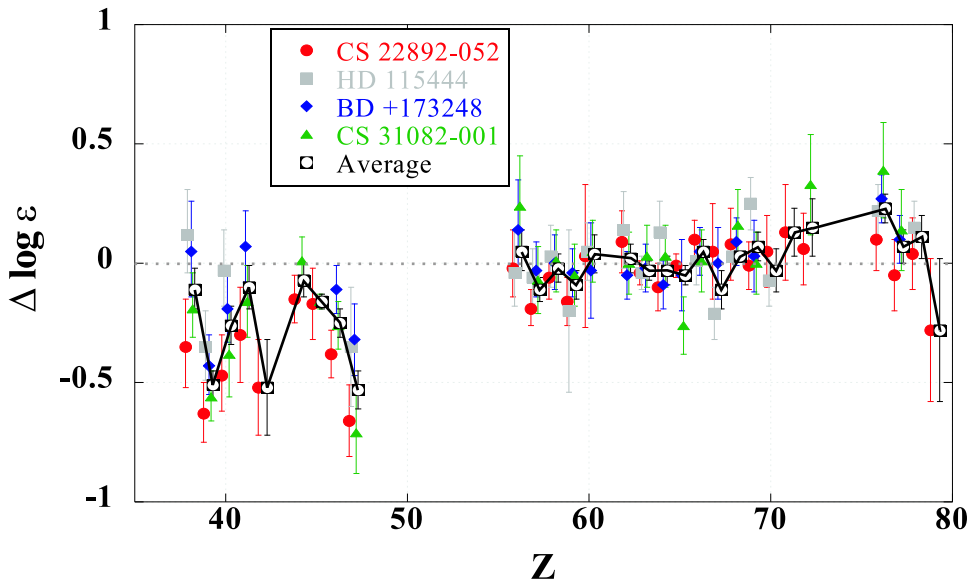

Figure 5.1: Differences between CS 22892-052, HD 155444, BD $+17^o$3248 and CS 31082-001 abundances and scaled solar r-process abundance pattern derived using Travaglio *et al.* [14]. The difference has been normalized such that the mean difference for elements in the range $56 \leq Z \leq 79$ is equal to zero.

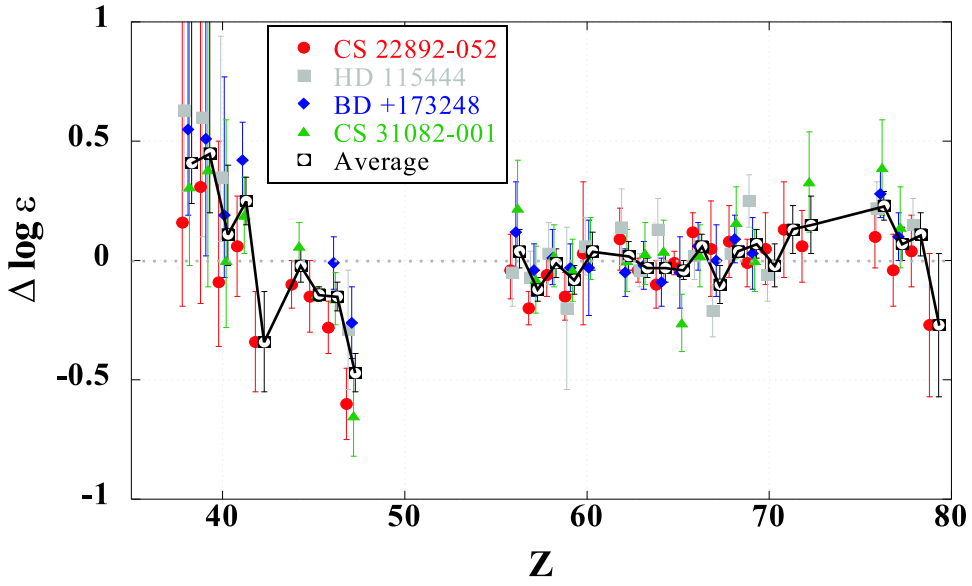

Figure 5.2: Differences between CS 22892-052, HD 155444, BD $+17^o$3248 and CS 31082-001 abundances and scaled solar r-process abundance pattern derived using Arlandini *et al.* [10]. The difference has been normalized such that the mean difference for elements in the range $56 \leq Z \leq 79$ is equal to zero.

shown for both models.

5.2 Different processes

Because isotopic abundances are much harder to obtain from spectroscopic data, only very limited information is available. Two stable isotopes of Eu have been observed [85,86] in metal-poor stars and their proportions agree with the solar system r-process proportion. Since the sun is only 4.6 billion years old, this isotopic agreement together with the good agreement of heavy elemental abundances (Z$\geq$56) between metal-poor and solar r-, suggests that the r-process creating these heavy elements has been pretty robust and uniform through time. It appears that conditions such as temperature, density and neutron flux vary only in a small range and that the r-process has been operating in the same way since it first started. The r-process responsible for the creation of the majority of r-process abundances has been referred in literature as the *strong* r-process [42].

It is generally believed that metal-poor stars are old stars that reflect the matter composition of just one or a few r-process nucleosynthesis events. Spectroscopic observations reflect the unburned material composition of the interstellar material from which those stars were formed. The difference $\Delta log\epsilon$ then would simply reflect the ratio of what had already been produced and was mixed in the interstellar medium where the r-process rich metal-poor stars were formed, over the composition of interstellar material produced by *many* r-process events at the time of the solar system formation,

$$\begin{aligned} \Delta log\epsilon_i &= log\epsilon_i^{star} - log\epsilon_i^{r-solar} \\ &= log\frac{Y_i^{star}}{Y_H} + 12 - log\frac{Y_i^{r-solar}}{Y_H} - 12 \\ &= log\frac{Y_i^{star}}{Y_i^{r-solar}}. \end{aligned} \tag{5.1}$$

Elements for which $\Delta log\epsilon < 1$ are elements that had less abundance when the star formed than when the sun formed. The observed Ag abundance in the metal-poor stars is only ≈30% ($\Delta log\epsilon \approx -0.5$) of the solar r-process abundance regardless of the model. For Ru, Rh and Pd, the observed abundance is between 50 and 90% of the solar r-process abundance. Because of the discrepancies for Z<56, another process responsible of creating the residual differences that the *strong* r-process cannot produce has been called the *weak* r-process [42] even though the astrophysical site and conditions in which a neutron-capture process would create the residual abundances are not yet known. The study of nucleosynthesis conditions that would create the missing abundances is the subject of this chapter.

For Sr, Y and Zr, the picture is not as clear due to the uncertainties in the s-process contribution. Also, the galactic chemical history as observed in their scaling with Fe and Eu indicates a different origin of those elements.

5.3 Residuals

To find the actual amount of material that is missing in these metal-poor stars, the r-process-rich star elemental abundance was subtracted from the r-process solar system abundance,

$$\Delta Y_i = Y_i^{r-solar} - Y_i^{star} = Y_H \left(10^{log\epsilon_i^{r-solar}} - 10^{log\epsilon_i^{star}}\right). \tag{5.2}$$

In a logarithmic scale the abundance residuals become

$$\begin{aligned} log\epsilon_{RES} &= log_{10}\frac{\Delta Y_i}{Y_H} + 12 \\ &= log_{10}\left(10^{log\epsilon_i^{solar}} - 10^{log\epsilon_i^{star}}\right) + 12.0. \end{aligned} \tag{5.3}$$

Figures 5.3 and 5.4 show the average amount of material that still would have to be produced in nucleosynthesis events in addition to the strong r-process to reach the

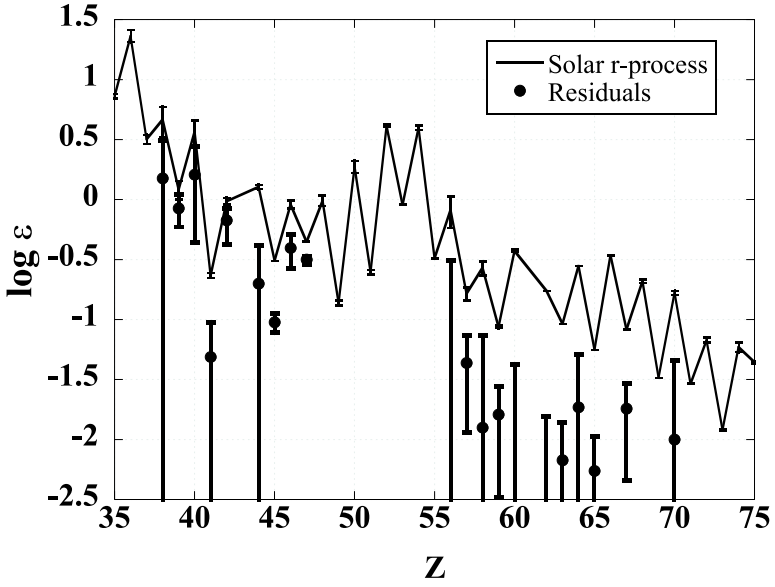

Figure 5.3: Average residual and solar r-process distributions as a function of atomic number derived using the Travaglio *et al.* [14] model.

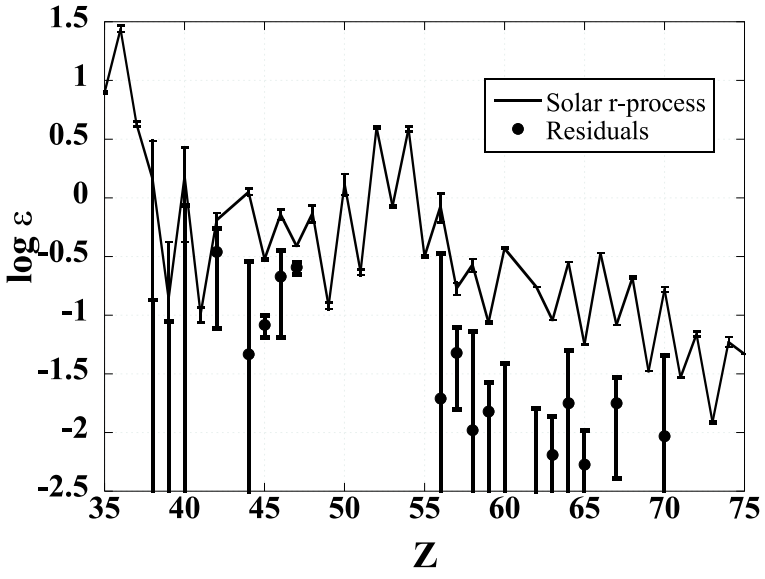

Figure 5.4: Average residual and solar r-process distributions as a function of atomic number derived using the Arlandini *et al.* [10] model.

solar system abundance pattern. The solar r-process abundance pattern is also shown for comparison. The average abundance for each element was obtained using the weighted average from Eq. 5.3 of the metal-poor star abundances. The total number of residual abundances that were considered was 21.

5.4 Reaction Network

To find the astrophysical conditions (n_n, T, τ) in which a neutron-capture process would produce the necessary residual abundance and pattern, a network calculation with classical neutron exposures from s-process to r-process type was used. Instead of a waiting point approximation, an abundance network containing 2026 nuclei from H to Ta was used. Nuclear reactions affected isotopic abundances for every time step. A range of different neutron densities and temperatures were chosen to simulate different astrophysical environments.

Nuclear reaction rates were taken from experiment and statistical model calculations. The Hauser-Feschbach code NON-SMOKER [87] was used to calculate the theoretical rates using the FRDM [48] mass model to calculate the Q values of the reaction. Theoretical β-decay rates were taken from [47] or when available from unpublished calculations by Kratz [88].

The initial abundance composition consisted of just neutrons and ^{56}Fe. While in principle neutron density could change due to neutron captures, the neutron to ^{56}Fe ratio was chosen so that n_n did not change by more than 5% of the initial value. The Ag abundance is generally believed to be the most accurate stellar observation of these r-process-rich stars. The abundances found in the reaction network were normalized to the residual Ag abundance. For this reason, only time steps with a silver abundance different than zero were studied.

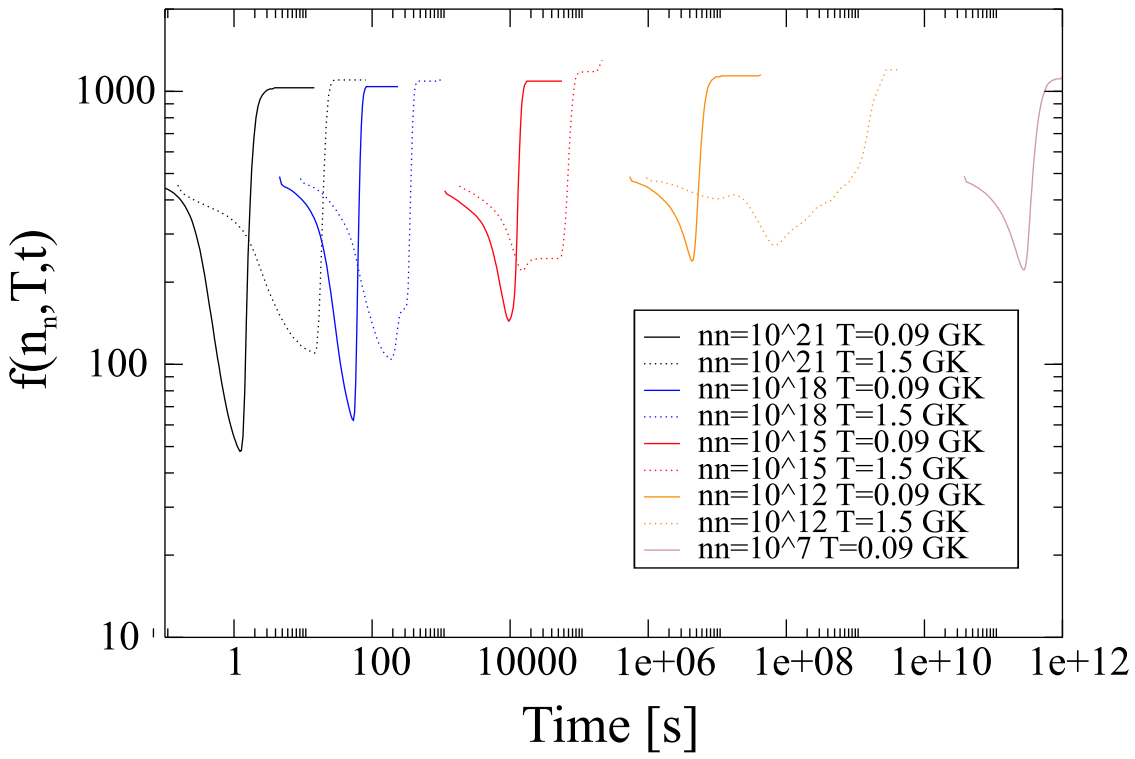

Figure 5.5: $f(n_n, T, t)$ as a function of time for different astrophysical conditions when using the Arlandini *et al.* [10] model.

5.5 Results

In order to find the right conditions that would create the residual abundance pattern, a chi-square function $f(n_n, T, t)$ defined as,

$$f(n_n, T, t) = \sum_{i \in RES} \left(\frac{Y_i^{CAL} - Y_i^{RES}}{\Delta Y_i^{RES}} \right)^2 , \tag{5.4}$$

was used. The residual abundance uncertainties depend on the metal-poor star observation uncertainties and the solar r-process uncertainties. The solar r-process abundances uncertainties depend mainly on the s-process uncertainties. Because in principle all the uncertainties are independent, the use of a chi-square function is justified.

The closer the value of $f(n_n, T, t)$ to the number of residuals is, the better the agreement between the abundance pattern calculation and the desired residual pattern.

Because the observed abundance pattern is the composition after the neutron flux is exhausted and nuclei had time to decay back toward stable nuclei, two consecutive steps were included in the network calculation. In the initial step, n_n was kept approximately constant as explained before. The temperature was kept constant as a function of time. For every time step, a *stable* abundance pattern was approximated by assuming an abrupt neutron exhaustion and a decay back to stability due *only* to β-decays. This "fast" decay back to stability was used because of the impracticality of running a decay network calculation for every time step. The "fast" decay *stable* pattern was compared to the desired residual abundance pattern by the function $f(n_n, T, t)$.

Typical $f(n_n, T, t)$ curves are shown in Fig. 5.5. The average atomic number of heavy nuclei, which starts at Fe, increases as a function of time. As the material becomes heavier, some of it reaches the region $38 \leq Z \leq 47$ resulting in a decrease of the function $f(n_n, T, t)$. The final increase in $f(n_n, T, t)$ is due to more and more material increasing its atomic number while the abundance in the region $38 \leq Z \leq 47$ decreases. For a given set of astrophysical conditions (n_n, T), an increase in the temperature causes an increase in photodisintegration and the moving of the neutron-capture process path closer to stability, where the β-decay half-lives are longer. This increase in $T_{1/2}$ reduces the speed of the process but the overall pattern of decrease and then increase of $f(n_n, T, t)$ is conserved. The half-lives of the progenitor isotopes that produce the $38 \leq Z \leq 47$ abundance also affect the time-width of the dip in the $f(n_n, T, t)$ curve. For high neutron density, the involved half-lives are short and the material spends less time passing through this region than when there is less neutron density. Because the isotopes involved when there is a low neutron density are closer to stability and therefore have longer half-lives, the time-width of the dip in the curve is larger.

Fig. 5.5 also shows that deeper minima exist for high n_n and low T. To better observe this, a new function was defined as $f(n_n, T) = f(n_n, T, \tau)$. The ideal neutron

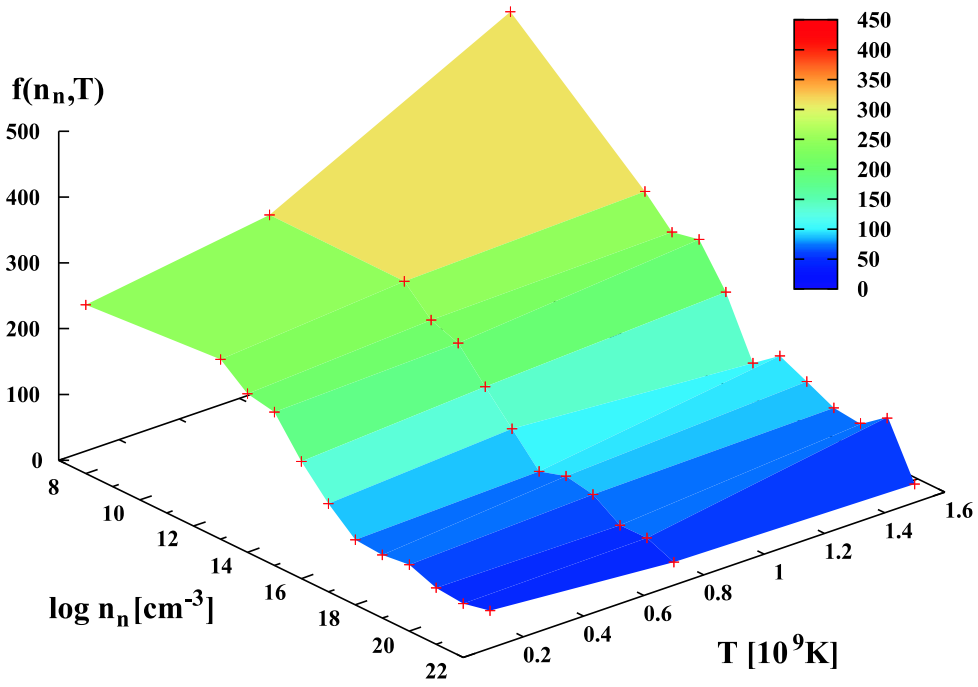

Figure 5.6: $f(n_n, T)$ in the parameter space when using Arlandini *et al.* residuals.

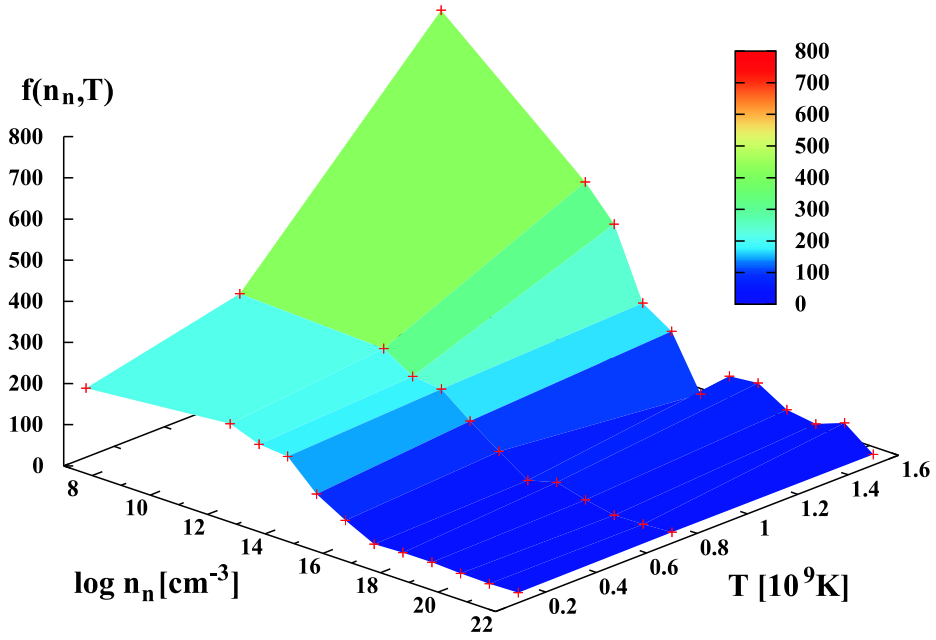

Figure 5.7: $f(n_n, T)$ in the parameter space when using Travaglio *et al.* residuals.

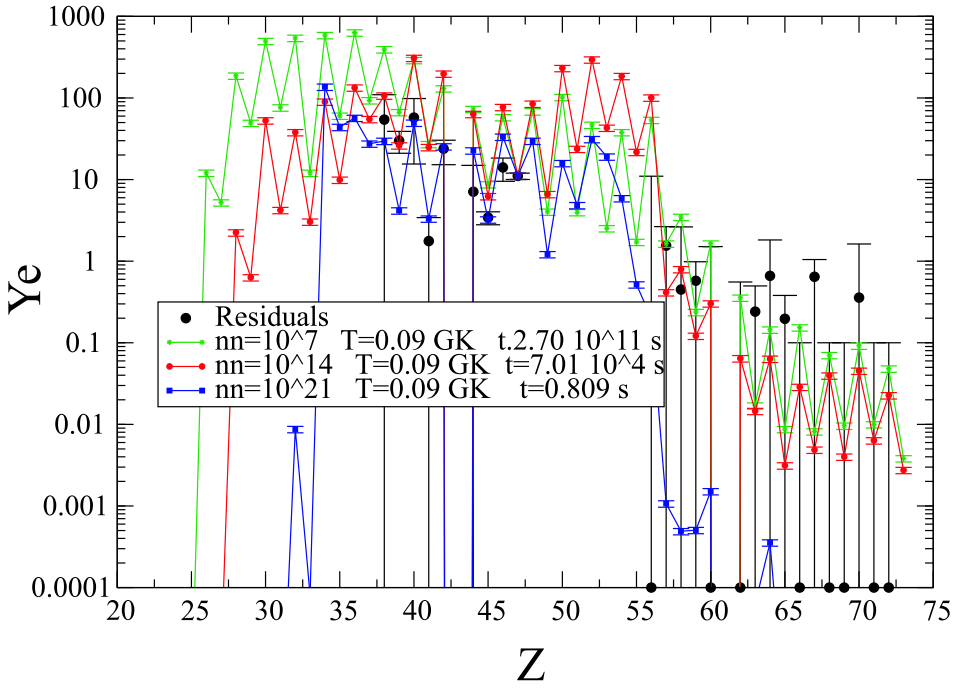

Figure 5.8: Abundances obtained using different astrophysical conditions. The desired residual distribution as a function of atomic number using the Travaglio *et al.* [14] model is also shown.

flux duration τ for each set of astrophysical conditions (n_n, T) was the time that minimized $f(n_n, T, t)$.

Figures 5.6 and 5.7 show $f(n_n, T)$ for different astrophysical conditions. Neutron-capture processes with a high neutron density $n_n \geq 10^{16}$ seem to reproduce the residual abundance pattern better. Regardless of the s-process contribution used, the abundance patterns that best fit the respective residual patterns were obtained with a r-process-like scenario. For high neutron densities, $f(n_n, T)$ stabilizes close to a minimum value. The absolute value of the function $f(n_n, T)$ is dependent upon the model used. In the Travaglio *et al.* model, $f(n_n, T)$ has a value around $20 - 50$ which corresponds to a normalized chi-square value of $1 - 2.5$ (the total number of residuals is 21). In the Arlandini *et al.* model, the normalized chi-square is around $2 - 4$.

Abundance patterns obtained using a sample of different astrophysical conditions are shown in Fig. 5.8 and 5.9. As mentioned before the residual pattern is better reproduced using a high neutron density. Low neutron densities do not reproduce

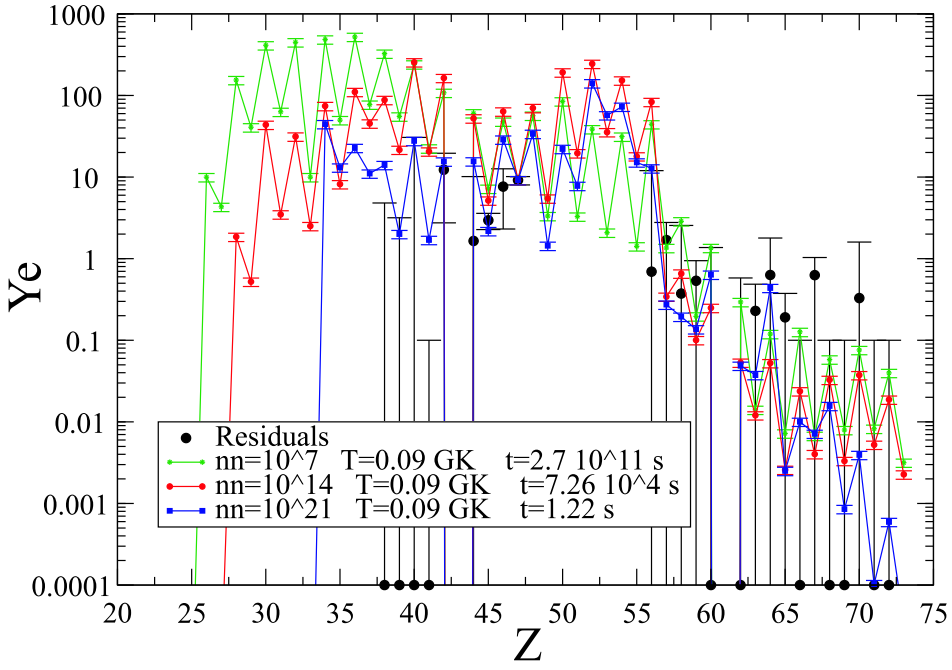

Figure 5.9: Abundances obtained using different astrophysical conditions. The desired residual distribution as a function of atomic number using the Arlandini *et al.* [10] model is also shown.

the residual abundance pattern due to the shell closure at N=82. To satisfactorily reproduce the residual abundance pattern most of the abundance has to go into $38 \leq Z \leq 47$. For $Z \geq 56$, the amount of created material has to be at least an order of magnitude less than the average abundance of the *light* heavy elements. At the shell closure, material tends to accumulate resulting in a peak in the abundance pattern. For processes with a relatively small neutron density, the shell closure produces progenitor bottleneck abundances that decay back to stability in the region $56 \leq Z \leq 60$ resulting in an overabundance of Ba. The high abundance in this region therefore prevents the correct residual pattern of low abundance for $Z \geq 56$. For processes with a large neutron density, the final abundance peak occurs around $52 \leq Z \leq 56$ and therefore the residual pattern may still be reproduced. It is unfortunate that there is no observational data to constrain the $52 \leq Z \leq 56$ abundances.

To better simulate the decay back to stability, another network calculation was run once the set of astrophysical conditions n_n, T and τ that minimizes f(n_n, T, t) had

been obtained. The initial abundance pattern of such calculation was the abundance at time τ (just before freezeout). The initial neutron density is set to zero to simulate a sudden freezeout. Using a full network allows the possibility of not only β-decays but other nuclear reactions such as captures of the emitted β-delayed neutrons while the system decays back to stability. The final abundance patterns shown in Fig. 5.10 and 5.11 are the result of such calculations.

Even though specific sets of astrophysical conditions were used in Fig. 5.10 and 5.11, similar r-process-like scenarios produced similar results.

5.6 Analysis

Generally there is good agreement between the solar r-process abundances and the sum of the observed main r-process abundances in metal-poor stars plus the here calculated weak r-process abundances from Section 5.5 as shown in Figs. 5.12 and 5.13. While the $Z \geq 56$ elements are produced in negligible quantities, the right abundance and pattern is obtained for the majority of the *light* heavy elements. Clearly, the residuals are drastically reduced from 0.5-1 (Figs. 5.1 and 5.2) to less than 0.25 when adding a high neutron density weak r-process component. This demostrates that the discrepancies between observed abundances and solar r-process abundances can be explained by a late weak r-process.

Exceptions are the abundances of Sr (only for the Arlandini case), Y and Pd. The Pd abundance is always overproduced, in the Arlandini *et al.* case by almost a factor of 3 compared to the expected solar r-process abundance. The abundance of ^{110}Pd and ^{105}Pd correspond to 35% of the final abundance in that case. Increasing the β-delayed neutron emission branchings (P_n) of ^{110}Sr, ^{110}Y, ^{110}Zr, ^{105}Kr, ^{105}Rb, ^{105}Sr and ^{105}Y decreases the final abundance of ^{110}Pd and ^{105}Pd as shown in Fig. 5.14. However, the overabundance of Pd still would be a factor of $\approx$2 even if the mentioned P_ns were increased to 100%. Another possible explanation to the high Pd abundance would

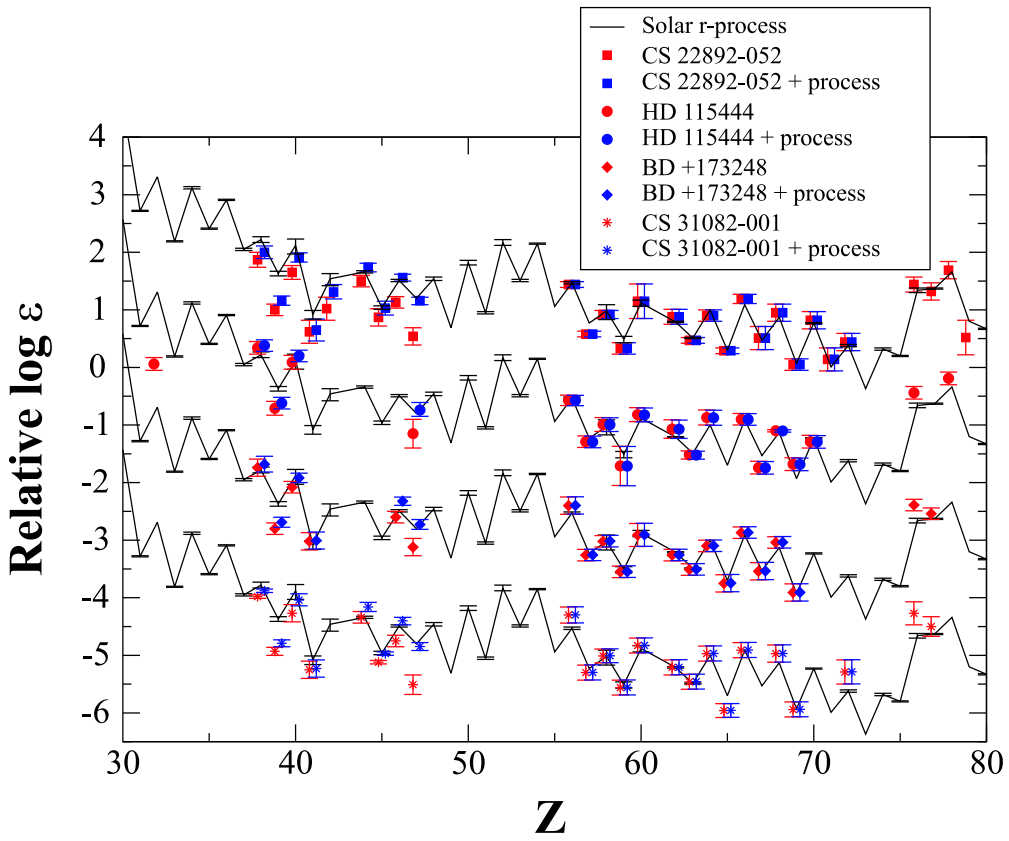

Figure 5.10: Sum of the elemental abundance pattern of r-process rich stars CS 22892-052, HD 155444, BD $+17^o3248$ and CS 31082-001 with the result of a network calculation using $n_n = 10^{21}\ cm^{-3}$, $T = 0.09\ GK$ and $\tau = 0.8\ s$ (red symbols), compared with solar r-process abundance (black lines) derived using the s-process contribution from Travaglio *et al.* [14]. Also shown are the star's abundances (blue symbols). Abundances have been shifted for all stars for display purposes.

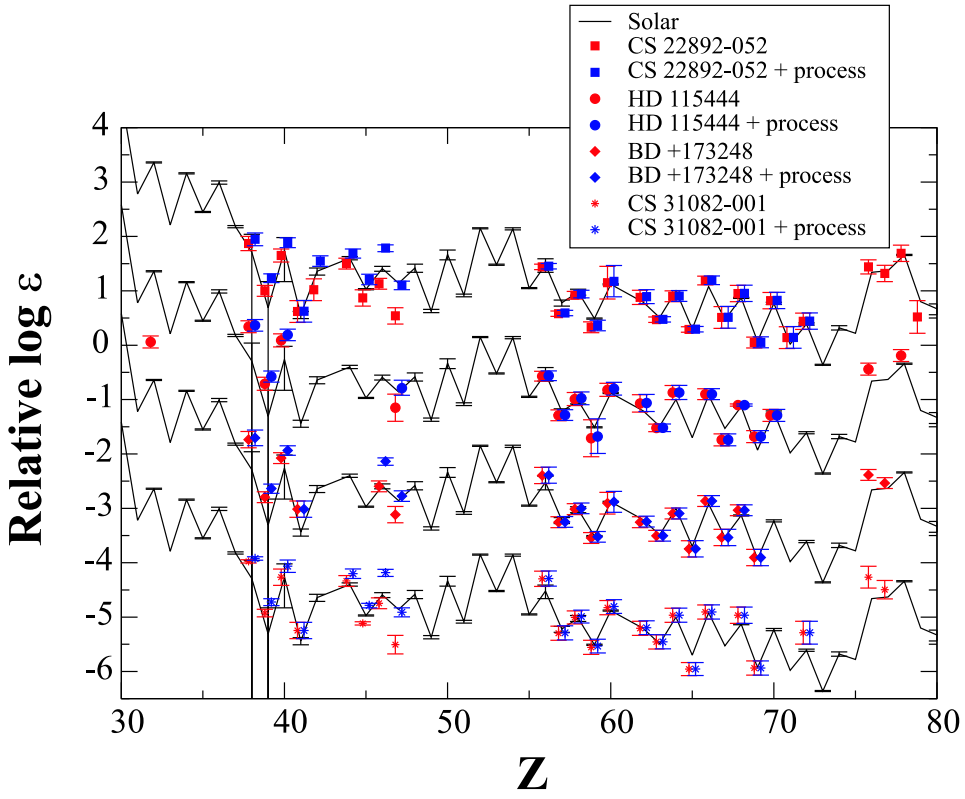

Figure 5.11: Sum of the elemental abundance pattern of r-process rich stars CS 22892-052, HD 155444, BD +17°3248 and CS 31082-001 with the result of a network calculation using $n_n = 10^{21}\ cm^{-3}$, $T = 0.09\ GK$ and $\tau = 1.2\ s$ (red symbols), compared with solar r-process abundance (black lines) derived using the s-process contribution from Arlandini *et al.* [10]. Also shown are the star's abundances (blue symbols). Abundances have been shifted for all stars for display purposes.

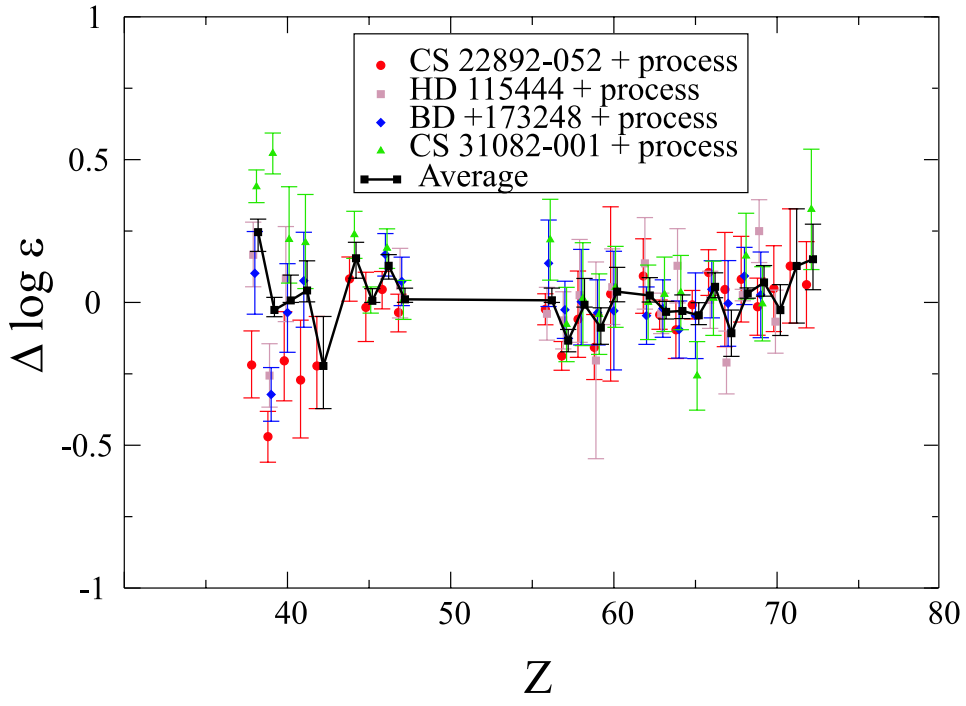

Figure 5.12: Differences between the sum of CS 22892-052, HD 155444, BD +17°3248 and CS 31082-001 abundances with the result of a network calculation using $n_n = 10^{21}\ cm^{-3}$, $T = 0.09\ GK$ and $\tau = 0.8\ s$, and scaled solar system abundance pattern derived using Travaglio *et al*. [14]. The difference has been normalized such that the mean difference for elements in the range $56 \leq Z \leq 79$ is equal to zero.

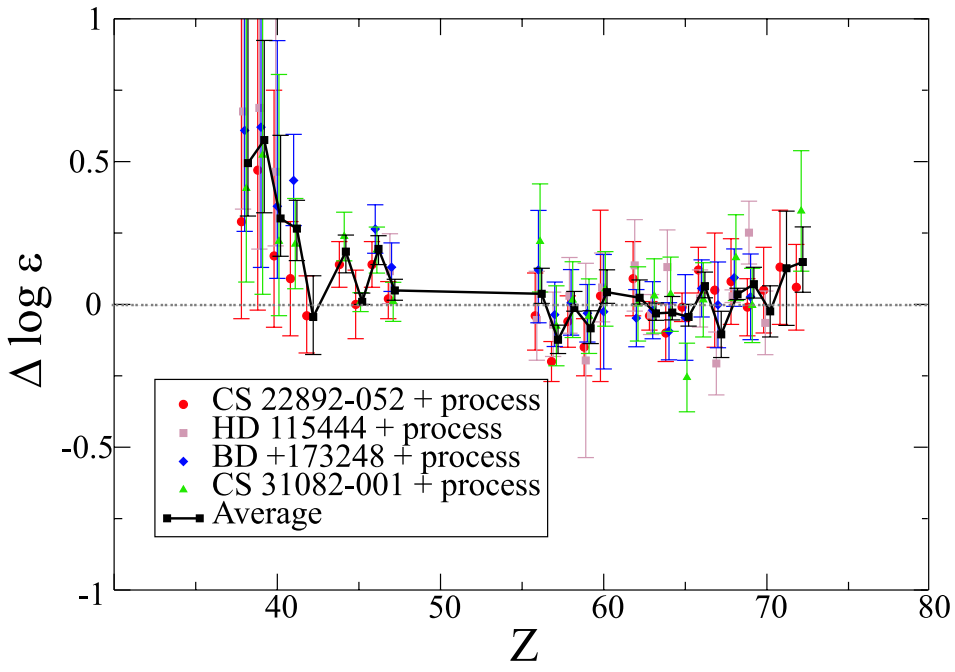

Figure 5.13: Differences between the sum of CS 22892-052, HD 155444, BD +17°3248 and CS 31082-001 abundances with the result of a network calculation using $n_n = 10^{21}\ cm^{-3}$, $T = 0.09\ GK$ and $\tau = 1.2\ s$, and scaled solar system abundance pattern derived using Arlandini *et al.* [10]. The difference has been normalized such that the mean difference for elements in the range $56 \leq Z \leq 79$ is equal to zero.

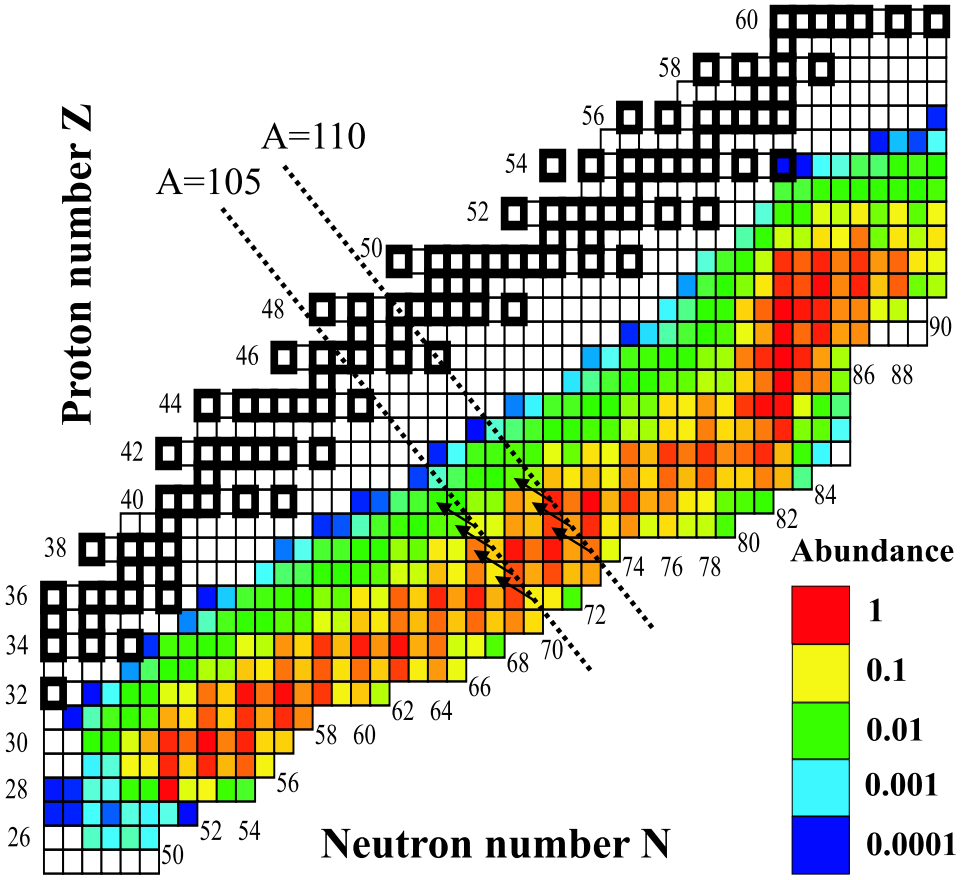

Figure 5.14: Mass region showing the calculated isotopic abundances just before freezeout using a network calculation with $n_n = 10^21\ cm^{-3}$, $T = 0.09\ GK$ and $\tau = 1.2\ s$. Largest abundances were normalized to 1. Squares with black thick lines represent stable isotopes. The most important β-delayed neutron emission branchings that reduce the final Pd abundance are also shown.

be an incorrect nuclear structure around N=70. Changing the neutron separation energy S_n would shift the progenitor abundances before freezeout affecting the final Pd abundance. As mentioned in section 2.3, a new magic number at N=70 may create new "waiting" points in a neutron-capture process. Depending on the strength of the new shell closure, the progenitor abundances could be shifted "upward" increasing the final abundance of Ag and Cd and thus reducing the relative Pd abundance.

The abundances of Y, Sr and Zr observed in the metal-poor stars exceed the solar r-process abundances when using the Arlandini model. The large scatter of the abundance ratios of these elements to heavier r-process elements may indicate an as-

trophysical origin different from the strong r-process. The observed overabundances could be just a reflection of this scatter. To decrease their abundance a process would have to destroy such elements and increase the abundance of the other *light* heavy elements. Such process was not observed, and the most promising scenario still increases the Sr and Y abundance by a small amount. However, because the s-process contribution for Sr and Y differ between the Arlandini and Travaglio models, it is not straightforward to reach any conclusion.

5.7 Conclusions and outlook

Astrophysical observation indicate that an additional mechanism besides the *strong* r- processes is necessary to account for the observed solar r-process abundance in the region $Z \leq 47$. Even though this mechanism had been referred as the *weak* r-process, the astrophysical scenario and conditions necessary for such a process were not known. There is however some ambiguity in the amount of material such a process creates due to the discrepancies in the solar r-process abundances between the Arlandini *et al.* and Travaglio *et al.* models. The calculations and results presented in this chapter are the first step toward determining the conditions that would result in the creation of these residual abundances.

To find a set of astrophysical conditions (neutron density, temperature and neutron flux duration) that would allow a neutron-capture process to produce the correct abundance pattern, a network calculation with different neutron densities and temperatures was used. Neutron densities were spanned from a s-process-like ($n_n \approx 10^7\ cm^{-3}$) to a r-process-like ($n_n \approx 10^{21}\ cm^{-3}$) scenario. Temperature was also spanned from 0.09 to 1.5 GK.

In general, the neutron densities and temperatures that better fit the missing material resemble an r-process like scenario regardless of which solar r-process abundances are used. This result justifies the name, weak $r-process$, as the process

responsible of creating such residuals.

Discrepancies such as the overabundance of Pd may be due to the incorrect nuclear structure used in the calculation. Changing the theoretical nuclear reaction rates by using a different mass model would give some clues as in fact, the problem of the Pd overabundance is due to nuclear structure uncertainties, and it requires further study. In addition, the abundance of Y and Sr seem to differ from the solar abundance but the s-process contribution also differ between models.

Supernovae explosions and neutron star mergers are the preferred possible sites of an r-process. These sites have different astrophysical conditions and the neutron star mergers reach a neutron density of up to $10^{30}\ cm^{-3}$. To further constraint the scenario responsible for creating the residual abundance, the calculations presented here should be extended to more neutron-rich densities to account for the possibility of neutron star mergers producing the residual abundances.

Recent results form the Hamburg/ESO R-process Enhanced Star survey (HERES) [89–91] extended the number of r-I and r-II stars for which elemental abundances have been measured. Elemental abundances exist now for Sr, Y, Zr, Ba, La, Ce, Nd, Sm and Eu for 8 new r-II stars and 35 r-II stars. Among the light r-process elements, Y, Sr and Zr show scatter that is larger than explained by error in the observational analysis. These new observations should be included in the future in the current analysis to better constraint the contribution of a weak r-process to their observed abundances. In the next few years, the Sloan Extension for Galactic Understanding and Exploration (SEGUE) should extend the number of observed r-process enhanced stars to a minimum of 100-150 r-II stars and 300-500 r-I stars [92]. Such amount of spectroscopic data would put the r-process into solid observational ground and put further constraints in the modeling of the astrophysical production of weak r-process elements.

Appendix A

Abundances

Abundance is defined as

$$Y_i = \frac{X_i}{A_i}, \tag{A.1}$$

where X_i is the mass fraction of a given element or isotope. It is a standard definition independent of density when dealing with how much material exist in a given environment. The number density of a given element or isotope can also be expressed in terms of abundance with

$$n_i = \frac{X_i \rho}{m_1} =_{CGS} \frac{X_i \rho N_A}{A_i} = Y_i \rho N_A, \tag{A.2}$$

if CGS units are used. Because differences between elements vary by orders of magnitude, a commonly used definition is

$$A_{el} = log_{10}\left(\frac{Y_{el}}{Y_H}\right) + 12.0 = log\epsilon. \tag{A.3}$$

The elemental abundance can also be expressed as

$$Y_{el} = Y_H 10^{log\epsilon - 12}. \tag{A.4}$$

Bibliography

[1] J. J. Cowan et al. *Phys. Rep.*, **208**:267, 1991.

[2] M. Asplund et al. The solar chemical composition. In *Cosmic Abundances as Records of Stellar Evolution and Nucleosynthesis*. ASP Conference Series, 2005. F. N. Bash and T.G. Barnes (editors).

[3] Donald D. Clayton. *Principles of Stellar Evolution and Nucleosynthesis*. McGraw-Hill, 1968.

[4] E.M. Burbidge et al. *Rev. Mod. Phys.*, **29**:547, 1957.

[5] S. Wanajo et al. *Nucl. Phys. A*, **616**:91, 1997.

[6] J. L. Fisker et al. *Nucl. Phys. A*, **752**:604, 2005.

[7] J. Pruet et al. *Astrophys. J*, **623**:325, 2005.

[8] E. Anders and N. Grevesse. *Geochim. Cosmochim. Acta*, **53**:97, 1989.

[9] C. M. Raiteri et al. *Astrophys. J*, **387**:263, 1992.

[10] C. Arlandini et al. *Astrophys. J*, **525**:886, 1999.

[11] D. D. Clayton et al. *Annu. Phys.*, **12**:331, 1961.

[12] B. S. Meyer. *Annu. Rev. Astron. Astrophys.*, **32**:153, 1994.

[13] F. Käppeler et al. *Rep. Prog. Phys.*, **52**:945, 1989.

[14] C. Travaglio et al. *Astrophys. J*, **601**:864, 2004.

[15] K.-L. Kratz et al. *Astrophys. J*, **402**:216, 1993.

[16] Y. Aboussir et al. *At. Data and Nucl. Data Tables*, **61**:127, 1995.

[17] J. M. Pearson et al. *Phys. Lett. B*, **387**:455, 1996.

[18] J. J. Cowan and C. Sneden. Origin and evolution of the elements. In *Carnegie Observatories Astrophysics Series*. Cambridge University Press, 2004. Ed. A. McWilliam and M. Rauch.

[19] C. Sneden et al. *Astrophys. J*, **591**:936, 2003.

[20] J. Westin et al. *Astrophys. J*, **530**:783, 2000.

[21] J. J. Cowan et al. *Astrophys. J*, **572**:861, 2002.

[22] V. Hill et al. *Astron. Astrophys.*, **387**:560, 2002.

[23] S. E. Woosley and E. Baron. *Astrophys. J*, **391**:228, 1992.

[24] B. S. Meyer et al. *Astrophys. J*, **399**:656, 1992.

[25] K. Takahashi et al. *Astron. Astrophys.*, **286**:857, 1994.

[26] S. E. Woosley et al. *Astrophys. J*, **433**:229, 1994.

[27] Y.-Z. Qian and other. *Phys. Rev. Lett.*, **71**:1965, 1993.

[28] R. C. Duncan et al. *Astrophys. J*, **309**:141, 1986.

[29] S. E. Woosley and R. D. Hoffman. *Astrophys. J*, **395**:202, 1992.

[30] S. Wanajo et al. *Astrophys. J*, **593**:968, 2003.

[31] H.-T. Janka et al. *Nucl. Phys. A*, **758**:19, 2005.

[32] J. M. Lattimer and D. N. Schramm. *Astrophys. J*, **192**:L145, 1974.

[33] J. M. Lattimer and D. N. Schramm. *Astrophys. J*, **210**:549, 1976.

[34] M. Ruffert et al. *Astron. Astrophys.*, **319**:122, 1997.

[35] S. Rosswog et al. *Astron. Astrophys.*, **341**:499, 1999.

[36] B. S. Meyer. *Astron. Astrophys.*, **343**:254, 1989.

[37] C. Freiburghaus et al. *Astrophys. J*, **525**:L121, 1999.

[38] D. Argast et al. *Astron. Astrophys.*, **416**:997, 2004.

[39] J. J. Cowan and F.-K. Thielemann. *Phys. Today*, **10**:47, 2004.

[40] G. C. Mclaughlin and R. Surman, 2004. arXiv:astro-ph/0407555.

[41] M. Terasawa et al. *Astrophys. J*, **608**:470, 2004.

[42] B. Pfeiffer et al. *Nucl. Phys. A*, **693**:282, 2001.

[43] H. Schatz et al. *Astrophys. J*, **579**:626, 2002.

[44] P. Hoff et al. *Phys. Rev. Lett.*, **77**:1020, 1996.

[45] I. Dillmann et al. *Phys. Rev. Lett.*, **91**:162503, 2003.

[46] B. A. Brown and other. *Nucl. Phys. A*, **719**:177c, 2003.

[47] P. Möller and J. Randrup. *Nucl. Phys. A*, **514**:1, 1990.

[48] P. Möller et al. *At. Data and Nucl. Data Tables*, **59**:185, 1995.

[49] M. Hannawald et al. *Phys. Rev. C*, **62**:054301, 2000.

[50] G. Audi and A.H. Wapstra. *Nucl. Phys. A*, **595**:409, 1995.

[51] A. P. Zuker J. Duflo. *Phys. Rev. C*, **52**:R23, 1995.

[52] J. Dobaczewski et al. *Phys. Rev. C*, **53**:2809, 1996.

[53] S. Goriely et al. *At. Data and Nucl. Data Tables*, **77**:311, 2001.

[54] M. Samyn et al. *Phys. Rev. C*, **66**:024326, 2002.

[55] J. C. Wang et al. *Phys. Lett. B*, **454**:1, 1999.

[56] J. Äystö et al. *Phys. Rev. Lett.*, **69**:1167, 1992.

[57] A. Jokinen et al. *Eur. Phys. J. A*, **9**:9, 2000.

[58] Z. Janas et al. *Nucl. Phys. A*, **552**:340, 1993.

[59] W. B. Walters et al. *Phys. Rev. C*, **70**:034314, 2004.

[60] B. Pfeiffer et al. *Acta Phys. Polon.*, **B27**:475, 1996.

[61] R. Bengtsson P. Möller. Subm. to Nature.

[62] N. Schunck et al. *Phys. Rev. C*, **69**:061305, 2004.

[63] D. J. Morrisey et al. *Nucl. Instr. and Meth. B*, **204**:90, 2003.

[64] J. I. Prisciandaro et al. *Nucl. Instr. and Meth. A*, **505**:140, 2003.

[65] P. T. Hosmer et al. to be published.

[66] D. Bazin et al. *Nucl. Instr. and Meth. A*, **482**:307, 2002.

[67] GSI, 1998. http://www-aix.gsi.de/ scheid/ATIMA1.html.

[68] J. F. Ziegler et al. *The Stopping and Range of Ions in Solid.* Pergamon Press, New York, 2003.

[69] W. F. Mueller et al. *Nucl. Instr. and Meth. A*, **466**:492, 2001.

[70] Kenneth S. Krane. *Introductory Nuclear Physics.* John Wiley & Sons, Inc., 1988.

[71] M. Bernas et al. *Z. Phys. A*, **336**:41, 1990.

[72] R. Schneider et al. *Nucl. Phys. A*, **588**:191, 1995.

[73] A. Stolz, 2002. A method of maximum likelihood for analyzing half-lives.

[74] B. Pfeiffer et al. *Prog. Nucl. Energy*, **41**:39, 2002.

[75] W. Brüchle. *Radiochim. Acta*, **91**:71, 2003.

[76] P.L. Reeder et al. *Phys. Rev. C*, **27**:3002, 1983.

[77] V.N. Fedoseyev et al. *Z. Phys. A*, **353**:9, 1995.

[78] H. Penttila et al. *Z. Phys. A*, **338**:291, 1991.

[79] J. C. Wang et al. *Phys. Rev. C*, **63**:024309, 2001.

[80] H. Penttila et al. *Phys. Rev. C*, **44**:R935, 1991.

[81] A. Jokinen et al. *Nucl. Phys. A*, **549**:420, 1992.

[82] J. Kurpeta et al. *Eur. Phys. J. A*, **2**:241, 1998.

[83] B. Tomlin et al. to be published.

[84] G. Audi et al. *Nucl. Phys. A*, **729**:3, 2003.

[85] C. Sneden et al. *Astrophys. J*, **566**:L25, 2002.

[86] W. Aoki et al. *Astrophys. J*, **586**:506, 2003.

[87] T. Rauscher and F.-K. Thielemann. *At. Data and Nucl. Data Tables*, **75**:1, 2000.

[88] K.-L. Kratz, 2005. unpublished private communication.

[89] N. Christlieb et al., 2004. arXiv:astro-ph/0408389.

[90] P. S. Barklem et al., 2004. arXiv:astro-ph/0505050.

[91] T. C. Beers et al. *Annu. Rev. Astron. Astrophys.*, **43**:531, 2005.

[92] T. C. Beers, 2005. The Oldest Stars.